Limb scatter measurements of high altitude cloud distributions

A Thesis Submitted to the
College of Graduate Studies and Research
in Partial Fulfillment of the Requirements
for the degree of Master of Science
in the Department of Physics and Engineering Physics
University of Saskatchewan
Saskatoon

By
Elise N. Normand

Permission to Use

In presenting this thesis in partial fulfillment of the requirements for a Postgraduate degree from the University of Saskatchewan, the author agrees that the Libraries of this University may make it freely available for inspection. The author further agrees that permission for copying of this thesis in any manner, in whole or in part, for scholarly purposes may be granted by the professor who supervised this thesis work or, in his absence, by the Head of the Department or the Dean of the College in which this thesis work was done. It is understood that any copying or publication or use of this thesis or parts thereof for financial gain shall not be allowed without written approval from the author. It is also understood that due recognition shall be given to the author and to the University of Saskatchewan in any scholarly use which may be made of any material in this thesis.

Requests for permission to copy or to make other use of material in this thesis in whole or in part should be addressed to:

Head of the Department of Physics and Engineering Physics
163 Physics Building
116 Science Place
University of Saskatchewan
Saskatoon, Saskatchewan
Canada
S7N 5E2

Abstract

Clouds have pivotal influence on the Earth's hydrological cycle and climate system because they are intricately involved in the dynamical, chemical, and radiative processes within the upper troposphere and lower stratosphere. Cirrus clouds occur at high altitude around the tropopause level and, despite their thin appearance and low optical thickness, they contribute to the radiative balance of the atmosphere. The processes in this region of the atmosphere have become increasingly important for a clear understanding of feedback mechanisms in the climate system.

The Canadian designed and built Optical Spectrograph and Infrared Imaging System (OSIRIS) satellite instrument measures the spectrum of sunlight scattered from the Earth's atmosphere at wavelengths from the ultraviolet (280 nm) to the near infrared (810 nm). The *limb scattering* measurement technique allows OSIRIS to collect information on the vertical profile of atmospheric chemical and particle composition at a resolution of approximately 2 km with nearly global daily coverage.

In this work, a technique characterizing the distribution of cirrus cloud top occurrences from OSIRIS limb scattering radiance profiles is presented. The technique involves computing residual profiles by comparing normalized measured radiance and modelled molecular density profiles where mismatches between the two traces indicate the presence of clouds. Probability density functions of scattering residuals show the distribution is not a continuum measurement; there is a clear distinction between the cloudy and cloud-free conditions. Observations show high cloud top occurrences in the upper troposphere and lower stratosphere region above Indonesia and Central America. Results obtained using the high altitude cloud detection technique and OSIRIS measurements are compared to those by *Sassen et al.* (2008) who used CALIPSO nadir measurements and to those by *Wang et al.* (1996) who used SAGE II solar occultation measurements of cirrus clouds.

The cloud detection technique is applied to three case studies. Cloud top detections are used to support results presented in *Dessler* (2009) who theorized the local relative humidity controls either dehydration or hydration of the lower stratosphere through the efficiency of evaporation of ice lofted by deep convection. The second study makes use of the cloud detection technique to eliminate cloud-containing scans as to identify an Asian Tropopause Aerosol Layer in support of *Vernier et al.* (2011). Finally, the technique is used to track the dispersion and evolution of the volcanic plume following the Sarychev eruption in June 2009 since monitoring volcanic plumes is an effective way to help mitigate aviation hazards.

Acknowledgements

A special and heartfelt thanks is extended to my supervisor, Dr. Adam Bourassa, for his inspiration, enthusiasm, and interest in my work. I am grateful for his encouragement, sound advice, and effort to explain concepts simply and clearly. This master's thesis would not have been possible without his generous help and guidance over the past two years.

I wish to thank Nick Lloyd for his advice and numerous conversations, which often helped me consider and understand problems from a different point of view. Also, I would like to thank my student colleagues and office-mates for providing me with a stimulating and enjoyable learning environment.

Lastly, I thank my parents, siblings, and family for supporting me throughout this journey as their encouragement and love has helped me undoubtedly.

Contents

List of Tables

List of Figures

List of Abbreviations

ACE	Atmospheric Chemistry Experiment
ATAL	Asian Tropopause Aerosol Layer
CALIOP	Cloud-Aerosol Lidar with Orthogonal Polarization
CALIPSO	Cloud-Aerosol Lidar Pathfinder Satellite Observations
CCD	Charge Coupled Device
DU	Dobson Units
ECMWF	European Center for Medium-Range Weather Forecasting
ExUTLS	Extra-Tropical Upper Troposphere and Lower Stratosphere
FTS	Fourier Transform Spectrometer
IASI	Infrared Atmospheric Sounding Interferometer
IRI	Infra-Red Imaging module of OSIRIS
ITCZ	Intertropical Convergence Zone
GEOS	Goddard Earth Observing System Model
LZRH	Level of Zero Radiative Heating
MLS	Microwave Limb Sounder
NASA	National Aeronautics and Space Administration
NCEP	National Centers for Environmental Prediction
OS	Optical Spectrograph module of OSIRIS
OSIRIS	Optical Spectrograph and Infra-Red Imaging System
PDF	Probability Density Function
ppmv	Parts Per Million by Volume
PSC	Polar Stratospheric Cloud
PV	Potential Vorticity
PVU	Potential Vorticity Units
R	Scattering Residual
ROI	Region Of Interest
SAA	South Atlantic Anomaly
SAGE	Stratospheric Aerosol and Gas Experiment
SASKTRAN	University of Saskatchewan Radiative Transfer Model
SR	Scattering Ratio
STE	Stratosphere-Troposphere Exchange
TTL	Tropical Tropopause Layer
UTLS	Upper Troposphere and Lower Stratosphere
VAAC	Volcanic Ash Advisory Center
VEI	Volcanic Explosivity Index
WMO	World Meteorological Organization

List of Nomenclatures

Symbol	Name	Units
a	Particle Radius	nm
α	Specific Volume	m^3/kg
c	Speed of Light	m/s
c_p	Specific Heat at Constant Pressure	J kg^{-1} K^{-1}
γ	Angle between the Scattered Electric Dipole Moment and the Observation Direction	
Γ	Lapse Rate	K/km
Γ_d	Dry Adiabatic Lapse Rate	K/km
Δs_T	Tangent Point Path Length	km
$\vec{\mathbf{E}}$	Total Electric Field	V/m
$\vec{\mathbf{E}}_0$	Applied Electric Field	V/m
$\vec{\mathbf{E}}_{scat}$	Scattered Electric Field	V/m
f	Coriolis Parameter	rad/s
F	Monochromatic Irradiance	$\frac{\text{photons}}{\text{cm}^2\ \text{s}\ \mu\text{m}}$
g	Acceleration due to Gravity	m/s^2
ζ	Relative Isentropic Vorticity	rad/s
h	Plank's Constant	m^2 kg s^{-1}
H	Pressure Scale Height	km
ϑ	Potential Temperature	K
θ	Solar Zenith Angle	
Θ	Solar Scattering Angle	
I	Monochromatic Radiance	$\frac{\text{photons}}{\text{cm}^2\ \text{s steradian nm}}$
$\mathcal{I}$	Intensity	V^2/m^2
J	Radiance Source Term	$\frac{\text{photons}}{\text{cm}^2\ \text{s steradian nm}}$
κ	Extinction	1/km
κ_{abs}	Absorption Extinction	1/km
κ_{scat}	Scattering Extinction	1/km
k	Wavenumber	1/nm
λ	Wavelength	nm
m	Relative Refractive Index	
n	Number Density	$1/cm^3$
n_{abs}	Absorption Number Density	$1/cm^3$
n_{scat}	Scattering Number Density	$1/cm^3$
N_1, N_2	Complex Indices of Refraction	
N^2	Brunt-Vaisala Frequency	$1/s^2$
ν	Polarizability	m^3
ξ_n	Hankel Functions	
p	Pressure	Pa
$\vec{\mathbf{p}}$	Scattered Electric Dipole Moment	C m
$\vec{\mathbf{p}}_0$	Induced Electric Dipole Moment	C m
$P(\cos\Theta)$	Scattering Phase Function	

Q	Extinction Efficiency	
Q_{abs}	Absorption Efficiency	
Q_{scat}	Scattering Efficiency	
r	Distance to Observation Point	m
$\vec{r_0}$	Satellite Position	km
R_s	Specific Gas Constant	J kg^{-1} K^{-1}
ρ	Mass Density	kg/m^3
σ	Cross Section	cm^2
σ_{abs}	Absorption Cross Section	cm^2
σ_{scat}	Scattering Cross Section	cm^2
t	Time	s
T	Temperature	K
$\vec{\mathbf{T}}$	Transformation Matrix	
τ	Optical Depth	
ϕ	Solar Azimuth Angle	
ψ_n	Bessel Functions	
ω	Frequency	rad/s
$\hat{\mathbf{\Omega}}$	Propagation Direction	
$\hat{\Omega}_0$	Solar Direction	
$\hat{\mathbf{\Omega}}'$	Scattered Direction	
x	Size Parameter	
z	Altitude	km

Chapter 1

Introduction

The upper troposphere and lower stratosphere (UTLS) is roughly defined as the region of the atmosphere within 5 km of the tropopause (*Holton et al.*, 1995; *Gettelman et al.*, 2011) thus encapsulating the uppermost region of the troposphere and the lowermost region of the stratosphere. Here, important dynamic, chemical, and radiative aspects are coupled to each other and strongly affect surface temperatures. Clouds have pivotal influence on the Earth's hydrological cycle and climate system (*Chahine*, 1992; *Liou*, 1992; *Hobbs*, 1993) because they are intricately involved in the dynamic, chemical, and radiative processes within the UTLS.

Strong tropical convective systems can loft tropospheric air into the stratosphere (*Alcala and Dessler*, 2002; *Gettelman et al.*, 2002), which consequently affect stratospheric chemistry and the abundance of trace species therein (*Dessler*, 2002). Stratosphere-Troposphere Exchange (STE) is an important dynamical exchange process occurring through the tropopause and has considerable influence on the chemistry in the UTLS. *Corti et al.* (2006) suggest air may be lofted through the interaction between cirrus clouds and radiation.

The radiative balance of the atmosphere is regulated in part by clouds and aerosols. They reflect shortwave solar radiation back into space and consequently increase planetary albedo, the ratio between scattered and incoming radiation, which cools the Earth and scatter terrestrial thermally emitted infrared radiation, which warms the planet through the greenhouse effect (*Hartmann et al.*, 1992; *Liou*, 2002). Generally, the greater longwave effect leads to a net warming of the atmosphere (*Wang et al.*, 1996; *Sassen et al.*, 2009). However, *Liou* (1986) explains the local regulation of the radiative forcing depends on the Earth-atmosphere conditions where the clouds are formed and on the geometric and physical arrangements of the clouds.

Detecting the presence of clouds is not a simple task. Cloud visibility depends on several factors like the viewing geometry of the measuring instrument, the relative brightness between the targeted cloud and its background, and the scattering phase function, which characterizes scattering directionality. The optical thickness, τ, which is a function of wavelength, is a critical component

affecting visibility because it describes the fraction of radiation attenuated by a layer of atmosphere and is a function of the number density and cross section of atmospheric particles as well as the thickness of the optical layer. *Sassen and Cho* (1992) categorize clouds into three groups according to their optical thickness: Subvisual clouds with $\tau < 0.03$, threshold visible with $\tau \approx 0.03$, and thin cirrus with $\tau > 0.03$.

Cirrus clouds occur at high altitude around the tropopause level and, despite their thin appearance and low optical thickness, they contribute to the radiative balance of the atmosphere (*Liou*, 1986, 2002). Cirrus clouds are involved in STE (*Corti et al.*, 2006) and in the process controlling the distribution of water vapour in the UTLS (*Dessler and Minschwaner*, 2007; *Dessler*, 2009). However, the manner and extent of their involvement are uncertain. It is believed cirrus clouds connect atmospheric circulation and climate (*Sassen and Cho*, 1992). A complete understanding of cirrus clouds may be obtained through a thorough description of their physical extent and distribution, occurrence frequency, duration, refractive index, and particle size distribution, shape, and composition (*Wang et al.*, 1996).

This work studies the occurrence frequency and distribution of high altitude clouds. When viewed from the Earth's surface with a ground-based zenith lidar system or remotely using nadir sounding, subvisual clouds appear invisible because of their extremely low optical thickness and relative contrast to their background (*Sassen et al.*, 1989). Alternatively, subvisual clouds are readily measurable using the limb scattering remote sensing technique. The limb scattering technique is based on the concept of measuring sunlight, which, while scattered through the limb of the atmosphere, is imprinted with the signatures of atmospheric composition. Here, the instrument's line of sight is directed at a tangent altitude within the atmospheric limb. Vertical profiles are obtained by scanning multiple tangent altitudes sequentially (*Bourassa*, 2007). Two outstanding benefits to the limb scattering technique are its ability to provide high vertical resolution, much like the occultation technique, as well as good global coverage, similar to nadir sounding.

In this work, measurements from the Optical Spectrograph and Infra-Red Imaging System (OSIRIS), a Canadian satellite instrument that measures atmospheric limb profiles of scattered solar radiation, are used to develop a high altitude cloud detection technique. OSIRIS is onboard the Swedish satellite Odin and was launched November 2001 into a sun-synchronous polar orbit with a 98° inclination providing coverage between 82°S to 82°N. OSIRIS consists of an optical spectrograph, which measures scattered atmospheric limb radiance between 280 and 810 nm. The instrument was primarily designed to deduce information of the vertical profiles of ozone, nitrogen

dioxide, and stratospheric aerosol (*Murtagh et al.*, 2002; *Llewellyn et al.*, 2004), and is used here in the development of the cloud detection technique.

Atmospheric particles scatter radiation and the scattering efficiency depends on various properties of the scattering particle; namely on size, shape, and refractive index. Generally, increasing the particle size and altering the particle shape leads to more complex scattering features and directionality. Clouds are optically thicker than the molecular background, so the physics describing the scattering field are more involved. Simple radiative transfer models are designed to accommodate single scattering events for small, spherically symmetric particles. However, when clouds are involved, models capable of handling multiple scattering events, which are often computationally expensive, become necessary. Clouds are optically thicker than the molecular background, so measuring features or the abundance of species through a cloud is difficult. Determining boundary limits so as to make measurements down to the cloud height would be ideal. This is, in part, the reasoning for developing a cloud detection technique using OSIRIS measurements.

Chapter 2 presents relevant background on the Earth's atmosphere with particular concentration on the UTLS. Details on the OSIRIS instrument, limb scattering technique, various scattering regimes, and a brief overview of atmospheric radiative transfer are also explained.

The high altitude cloud detection technique is outlined in Chapter 3. The technique is based on computing the residual between the OSIRIS measured and modelled molecular radiance profiles, which characterizes scattering enhancements. Scattering probability density functions are then created from the residual profiles and unveil a distinction between the cloudy and cloud-free conditions; the distribution is not a continuum measurement, which is key to the technique. The technique is used to map the distribution of cloud top occurrences within the UTLS. Maxima cloud top occurrences are observed over Indonesia and Central America. These results are compared to those by *Sassen et al.* (2008) who used Cloud- Aerosol Lidar Pathfinder Satellite Observations (CALIPSO) nadir measurements and to those by *Wang et al.* (1996) who used Stratospheric Aerosol and Gas Experiment (SAGE) II solar occultation measurements of cirrus clouds.

Chapter 4 is comprised of three parts, each of which features a case study that uses the high altitude cloud detection technique. With reference to *Dessler* (2009), the first study relates cloud occurrence frequencies to the distribution of water vapour within the lower stratosphere. The stratosphere is either hydrated or dehydrated through the formation of clouds depending on local circulation patterns and relative humidity. OSIRIS cloud detections and water vapour measurements from the Atmospheric Chemistry Experiment (ACE) instrument affirm the results in *Dessler* (2009).

The cloud detection technique is used in the second study to investigate the presence of an Asian Tropopause Aerosol Layer (ATAL), recently reported by *Vernier et al.* (2011). The ATAL draws connections between the transport of aerosols to the upper atmosphere through deep convection and, as this work suggests, may exhibit a diurnal cycle. *Laaksonen et al.* (2000) propose a diurnal cycle that is linked to the formation of cloud condensation nuclei from sulfuric dioxide. Lastly, the third case study follows the dispersion and evolution of the volcanic plume following the Sarychev eruption on 12 June 2009. The limb scattered signal measured by OSIRIS is enhanced at the location of the ash and dust. Aviation hazards can potentially be reduced by tracking and monitoring the progression of the plume using satellite-derived data.

Chapter 5 summarizes conclusions drawn throughout this work and briefly outlines possible future work and applications involving the cloud detection technique.

Chapter 2

Background

2.1 The Earth's Atmosphere

The region between the first two layers of the atmosphere, namely the tropopause, which lies between the troposphere and the stratosphere, is of primary interest for studies on high altitude cirrus clouds since this is where cirrus clouds occur. The first section in this work is dedicated to explain the essential components of atmospheric science within the troposphere and the stratosphere as well as some atmospheric quantities such as the pressure scale height, potential temperature, and static stability. Since the tropopause is not necessarily a continuous surface globally, various definitions of the tropopause are presented and a description of atmospheric composition, such as molecules, aerosols, and cloud particles, follows.

2.1.1 The Troposphere and the Stratosphere

The layers of the Earth's atmosphere are commonly defined according to the vertical temperature profile of the atmosphere. Figure 2.1 shows a typical mid-latitude vertical temperature profile.

The lowermost layer of the atmosphere is called the *troposphere*, which from Greek means "to turn over" (*Gettelman et al.*, 2011) or "changing" (*Wallace and Hobbs*, 2006). The average temperature at the Earth's surface is around 288 K (*Liou*, 2002). Within the troposphere, temperature, T, decreases with altitude, z, with a lapse rate, Γ, of approximately 6.5°C km^{-1}. That is,

$$\Gamma \equiv -\frac{\partial T}{\partial z} \sim 6.5^{\circ}\mathrm{C\,km^{-1}}. \tag{2.1}$$

Temperature reaches a minimum at the tropopause around 220 K between 10 and 16 km in altitude. As *Liou* (2002) explains, both the convective movement of energy from the Earth to the atmosphere and the radiative balance shape the temperature structure in the troposphere.

The troposphere is generally well mixed because warm air near the surface of the Earth stimulates convection and vertical motion. Air and chemical species can be vertically transported through the

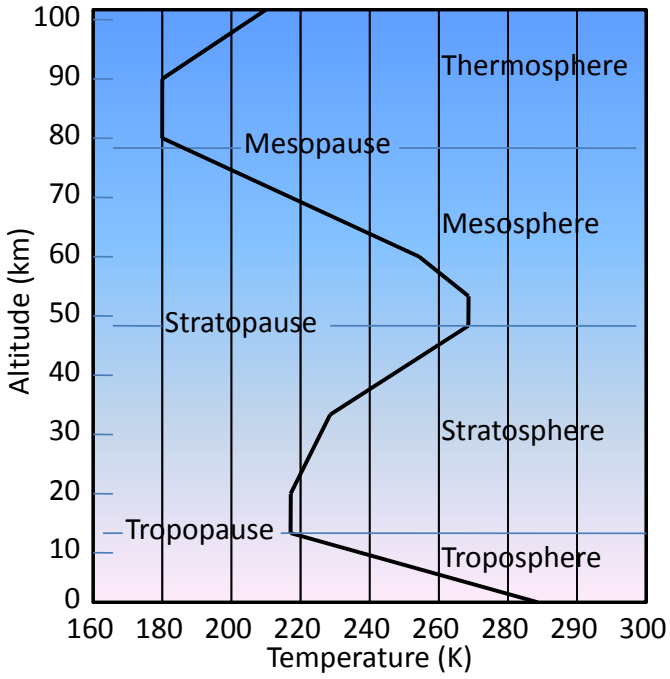

Figure 2.1: Typical mid-latitude vertical temperature profile; adapted from *Wallace and Hobbs* (2006).

depth of the troposphere within a few hours by means of moist convection to a few days via baroclinic eddy motions where large-scale perturbations in the mean flow are generated by changes in temperature or density along isobaric lines (*Holton et al.*, 1995).

Convection occurs in a couple ways. First, when a parcel of air is quickly moved to a higher altitude, for example when wind pushes a parcel of air up the side of a mountain or when the surface of the Earth heats a localized parcel of air causing it to rise suddenly, it is then hotter and less dense than the surrounding air. Since air does not dissipate heat quickly, the parcel of air will continue to rise in altitude. Second, consider layers of air of uniform temperature where the lower layer contains more moisture than the layer above it. When a parcel of air from the lower layer condenses, latent heat is released causing localized heating within the parcel and causes it to rise to higher altitudes. This parcel of air will continue to rise because of its lower density relative to the surrounding air.

Nearly 80% of the mass of the atmosphere and most clouds, precipitation, and water vapour are contained within the troposphere (*Wallace and Hobbs*, 2006). Aerosols are constantly absorbed by cloud droplets and ice crystals and eventually fall to the surface as rain or snow, which cleanses tropospheric air.

The *stratosphere* is the second layer of the atmosphere and is translated from Greek as "to spread out" (*Gettelman et al.*, 2011). The stratosphere is isothermal from the tropopause to approximately 20 km in altitude where the temperature begins to increase with altitude with a negative lapse rate, reaching a maximum around 270 K at the stratopause near 50 km (*Liou*, 2002). The stratosphere is very stable due to its temperature profile and therefore has little turbulence or convection and strong horizontal winds.

Ozone is abundant and water vapour is sparse in stratospheric air. The ozone layer is within the stratosphere between 15 and 30 km altitude with a maximum concentration near 20 to 25 km depending on latitude and season (*Liou*, 2002). Ozone absorbs solar radiation in the ultraviolet region, meaning the stratospheric ozone layer is an input of solar heating into the atmosphere and is responsible for the rise in temperature in the stratosphere (*Wallace and Hobbs*, 2006). Both the absorption of solar fluxes by ozone and the emission of infrared radiation by carbon dioxide, which is linked to the greenhouse effect, are key factors in determining the state of the stratosphere (*Liou*, 2002).

Aerosols are also present in the stratosphere and linger there for long periods of time due to slow vertical mixing. Stratospheric air is not cleansed through cloud formation as in the troposphere, so resident times are much longer. Compared to the troposphere, vertical transport in the stratosphere can take months or a year depending on altitude (*Holton et al.*, 1995). The upward propagation and dissipation of tropospheric waves, which are largely influenced by UTLS static stability and wind profiles, drive stratospheric circulation (*Chen and Robinson*, 1992).

2.1.2 Pressure Scale Height

The Ideal Gas Law can be written in terms of the specific gas constant, R_s, and relates pressure, p, to the mass density, ρ, and to absolute temperature, T, of the gas,

$$p = \rho R_s T. \tag{2.2}$$

Atmospheric pressure is determined by its weight and is described by the hydrostatic equation,

$$\frac{dp}{dz} = -g\rho. \tag{2.3}$$

Here, g is the acceleration due to gravity and ρ is the density of the air at altitude z. Solving Equation 2.2 for density, Equation 2.3 becomes,

$$\frac{dp}{p} = -\frac{g}{R_s T} dz, \tag{2.4}$$

after some rearrangement. Integrating the right hand side from a reference altitude, such as at sea level, to some altitude z and the left hand side from the reference pressure, $p(0)$, to the pressure at altitude z and rearranging, Equation 2.4 becomes,

$$p(z) = p(0)e^{-\frac{z}{H}}, \tag{2.5}$$

which describes the pressure profile as a function of altitude; pressure falls exponentially with altitude. H is defined as the pressure scale height,

$$H = \frac{R_s T}{g} \approx 7\,\text{km}. \tag{2.6}$$

The pressure scale height defines the distance over which the pressure drops by $\frac{1}{e} \approx 0.37$.

2.1.3 Potential Temperature and Static Stability

Potential temperature, ϑ, is the temperature a parcel of air would have if it was adiabatically compressed or expanded to a standard reference pressure, $p(0)$, usually 1 bar. It can be derived from the first law of thermodynamics for an adiabatic process where the thermal energy added to the system, $\mathrm{d}Q$, is zero,

$$0 = c_p \mathrm{d}T - \alpha \mathrm{d}p. \tag{2.7}$$

Here, c_p is the specific heat at constant pressure defined as,

$$c_p = \left.\frac{\mathrm{d}Q}{\mathrm{d}T}\right|_{p=\text{constant}}, \tag{2.8}$$

where T and p are the temperature and pressure, respectively, and $\alpha = \frac{1}{\rho}$ is the specific volume. Using the Ideal Gas Law in terms of the specific volume, $p\alpha = R_s T$, where R_s is the specific gas constant for dry air, Equation 2.7 becomes,

$$\frac{c_p}{R_s}\frac{\mathrm{d}T}{T} = \frac{\mathrm{d}p}{p}, \tag{2.9}$$

after some rearrangement. Integrating from the reference pressure, $p(0)$, where the temperature is $T = \vartheta$ by definition to the atmospheric pressure at altitude z, $p(z)$, where the temperature is T, and rearranging, the potential temperature is,

$$\vartheta = T\left(\frac{p(0)}{p(z)}\right)^{\frac{R_s}{c_p}}. \tag{2.10}$$

The relationship between potential temperature and lapse rate, Γ, can be derived by taking the logarithm of Equation 2.10 and differentiating with respect to height, z,

$$\frac{1}{\vartheta}\frac{\partial \vartheta}{\partial z} = \frac{1}{T}\frac{\partial T}{\partial z} - \frac{R_s}{c_p}\frac{1}{p}\frac{\partial p}{\partial z}. \tag{2.11}$$

Using the hydrostatic equation and the Ideal Gas Law and multiplying by T, Equation 2.11 becomes,

$$\frac{T}{\vartheta}\frac{\partial \vartheta}{\partial z} = \frac{\partial T}{\partial z} + \frac{g}{c_p}. \tag{2.12}$$

A dry adiabatic, hydrostatic atmosphere $\frac{\partial \vartheta}{\partial z} = 0$ implies the dry adiabatic lapse rate, Γ_d, is,

$$\Gamma_d = -\frac{\partial T}{\partial z} = \frac{g}{c_p} \sim 9.8^{\circ}\mathrm{C\,km^{-1}}. \tag{2.13}$$

Using Equations 2.1 and 2.13 in Equation 2.12, the relationship between potential temperature and lapse rate is,

$$\frac{T}{\vartheta}\frac{\partial \vartheta}{\partial z} = \Gamma_d - \Gamma. \tag{2.14}$$

Static stability is roughly defined as the resistive force to vertical motion by the density structure of the atmosphere (*Gates*, 1961). In the troposphere, the lapse rate given in Equation 2.1 is positive. As described above, if a parcel of air is adiabatically moved to a higher altitude, which is accomplished by quickly moving the parcel to a greater height, it will continue to rise because it is hotter and less dense than the surrounding environmental air. This scenario is unstable and static stability can be negative within the troposphere. Now consider a parcel of air near but just below the tropopause. There is a relative increase in static stability. Static stability in this region is almost zero, but it is increasing with altitude. In the stratosphere, the lapse rate is negative implying temperature increases with altitude. If a parcel of air in the stratosphere is quickly moved to a higher altitude, it will quickly sink then oscillate about the equilibrium point with a dampened amplitude and eventually regain its initial position. The adiabatic oscillations the parcel experiences in the statically stable atmosphere are called *buoyancy oscillations* and the frequency of oscillation is called the *buoyancy frequency* or the *Brunt-Vaisala frequency*, N^2, which quantifies the static stability,

$$N^2 = \frac{g}{\vartheta}\frac{\partial \vartheta}{\partial z}. \tag{2.15}$$

If $N > 0$ the parcel will oscillate about its initial position with a period $2\pi/N$. For typical tropospheric conditions, $N \simeq 1.2 \times 10^{-2}\,\mathrm{s^{-1}}$ and the period of buoyancy oscillation is $\tau \simeq 8$ minutes (*Holton*, 1979). When $N = 0$, there is no accelerating force and the parcel will be in equilibrium at its new altitude. In the case of $N^2 < 0$, temperature decreases with height and the atmosphere is unstable because the displacement will increase exponentially with time (*Holton*, 1979). The

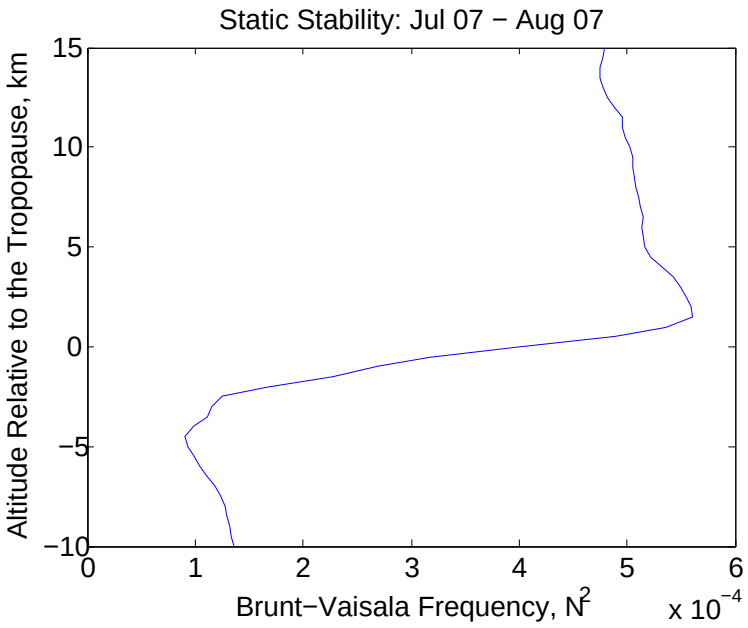

Figure 2.2: Averaged static stability profile over the months of July and August 2007. The potential temperature was computed from interpolated temperature and pressure profiles from the ECMWF reanalysis data.

important results for dry air are summarized in the following:

$$N^2 = \begin{cases} > 0 & \text{Stable} \\ = 0 & \text{Neutral} \\ < 0 & \text{Unstable} \end{cases}$$

Figure 2.2 shows an average vertical profile of the static stability over the months of July and August 2007. The Brunt-Vaisala frequency, N^2, was calculated according to Equation 2.15 where the potential temperature was computed from interpolated temperature and pressure profiles from the European Center for Medium-Range Weather Forecasts (ECMWF) reanalysis data. Synoptically, the atmosphere is always statically stable as any unstable regions are quickly stabilized through convective motion (*Holton*, 1979). The figure clearly shows the sharp increase in static stability across the tropopause.

2.1.4 The Tropopause and the UTLS

The *tropopause* is loosely defined as the boundary between the troposphere and the stratosphere. The tropopause altitude is not constant over all latitudes, reaching around 16 km near the equator and falling to 8 km at the poles. Formally, *Gettelman et al.* (2011) present three tropopause definitions. First, the *thermal tropopause*, sometimes referred to as the *cold point tropopause*, is defined

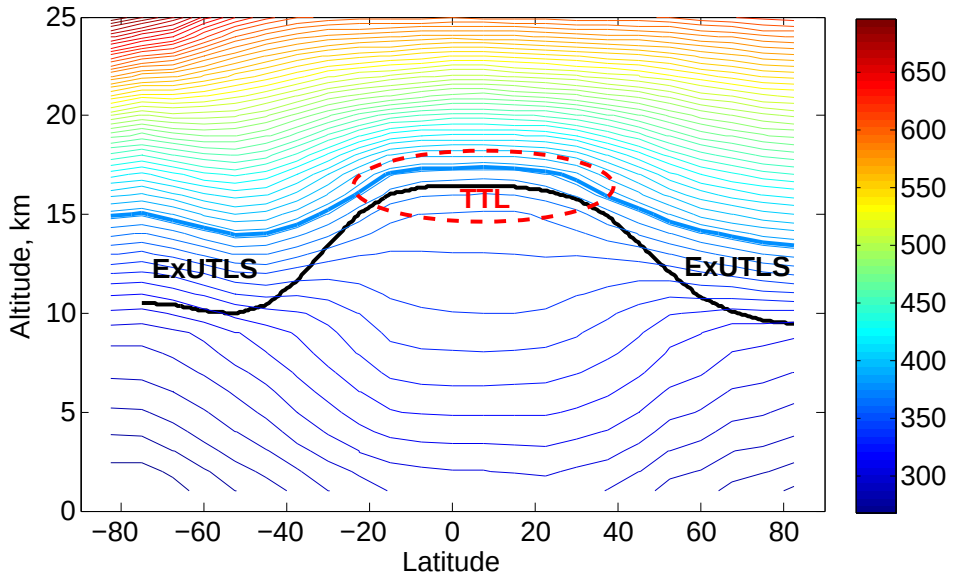

Figure 2.3: Thermal tropopause (thick black line) and lines of constant potential temperature, ϑ, (thin coloured lines) as a function of latitude, averaged from May till October 2007. The thick blue line shows the 380°K potential temperature line. The thermal tropopause was obtained in accordance to the WMO definition and based on calculated lapse rates from reanalysis data from the NCEP. The lines of constant potential temperature were calculated from interpolated temperature and pressure profiles from the ECMWF reanalysis data and are in Kelvin units. The TTL and ExUTLS, or lowermost stratosphere, regions are marked.

by the *World Meteorological Organization* (1957) using the lapse rate, $\Gamma \equiv -\frac{\partial T}{\partial z}$, which states that the tropopause is the lowest altitude where $\Gamma < 2\,\mathrm{K\,km^{-1}}$, provided the average lapse rate from this level to all higher levels within 2 km does not exceed $2\,\mathrm{K\,km^{-1}}$. By this definition, the tropopause is indicative of the vertical discontinuity in the atmospheric static stability (*Gettelman et al.*, 2011) and permits the possibility of multiple tropopauses. Multiple tropopauses are commonly observed near the jet stream, correlated with fronts, storms and stratospheric mixing with the troposphere (*Shapiro*, 1980). Consequently, the thermal tropopause does not necessarily form a continuous surface globally. Figure 2.3 shows the thermal tropopause and lines of constant potential temperature, ϑ, as a function of latitude. The thermal tropopause was obtained in accordance to the WMO definition and based on calculated lapse rates from reanalysis data from the National Centers for Environmental Prediction (NCEP). The lines of constant potential temperature were calculated from interpolated temperature and pressure profiles from the ECMWF reanalysis data.

Second, the *dynamical tropopause* is based on changes in potential vorticity (PV), which itself relies on components of static stability and relative vorticity, as in horizontal and vertical wind shears (*Gettelman et al.*, 2011). Relative vorticity is the vertical component of the curl of the wind

velocity vector. The dynamical tropopause relies on three-dimensional temperature and wind data making it ideal for synoptic-scale global models. PV consists of both a thermodynamical element and of a dynamical element. According to the definition by *Rossby* (1940) and *Ertel* (1942), PV relates the vorticity on an isentropic surface and static stability,

$$PV = -g(\zeta + f)\frac{\partial \vartheta}{\partial p}. \tag{2.16}$$

Here, g is the acceleration due to gravity, ζ is the relative isentropic vorticity, f is the Coriolis parameter, ϑ is the potential temperature, and p is the pressure. Note that $\frac{\partial \vartheta}{\partial p}$ is the static stability in terms of the potential temperature as per Equation 2.15 and the following hydrostatic relation conversion is used,

$$\frac{\partial \vartheta}{\partial z} = -g\rho\frac{\partial \vartheta}{\partial p}. \tag{2.17}$$

An isentropic surface is one with constant potential temperature. Unless heated diabatically through a release of latent heat, radiation, or a turbulent transfer of heat, as in friction, air remains at an isentropic level. The atmosphere is stratified in layers of constant potential temperature where the layers are more tightly bunched in the stratosphere due to the significant increase in static stability; refer to Figure 2.3. Since PV is proportional to static stability, as in Equation 2.16, PV also increases in the stratosphere. Equation 2.16 remains constant for each isentropic layer because a parcel of air will remain at a constant level of potential temperature and maintain the same PV value as long as it moves adiabatically throughout the atmosphere. Thus, static stability and relative vorticity are tied in such a way that PV is conserved on isentropic surfaces. As static stability increases, as in the stratosphere, relative vorticity must correspondingly decrease, and vice versa. Regions with high stratification have low vorticity, so PV contours run along the static stability gradient. Adversely, regions with weak stratification have dominant vortices and PV contours follow the wind gradient (*Gettelman et al.*, 2011). PV is commonly described in PV units (PVU) where $1\,\mathrm{PVU} = 1 \times 10^6\,\mathrm{K\,m^2\,kg^{-1}\,s^{-1}}$ and the dynamical tropopause is defined where the PV gradient is strongest.

Third, sharp gradients in chemical concentrations are the basis defining the *chemical tropopause*. Chemical tracers can be used to define regions of the atmosphere. As mentioned, the troposphere is rich in water vapour and there is an abundance of ozone in the stratosphere. Vertical mixing, which is copious throughout the troposphere, is inhibited at tropopause altitudes because of the temperature inversion. This natural barrier is primarily due to the drastic increase in the gradient of static stability. Dynamically, this implies a parcel of air may only cross PV isosurfaces following a diabatic

process (*Gettelman et al.*, 2011). By means of following the vertical profile of the concentration of trace gases, the chemical tropopause is defined where the gradient is greatest.

The UTLS is often said to include two regions: the Tropical Tropopause Layer (TTL) and the extra-tropical UTLS (ExUTLS), commonly referred to as the *lowermost stratosphere*. Tropical and the extra-tropical regions are distinguished according to the dominant physical processes in each region; radiative-convective balance in the tropics and baroclinic wave motions in the extra-tropics (*Held*, 1982). Further, the global stratospheric overturning circulation is upward in the tropics and downward in the extra-tropics (*Gettelman et al.*, 2011) in relation with the Brewer-Dobson circulation. The UTLS is sensitive to chemical, dynamical, and radiative changes thereby creating climate feedbacks (*Eyring et al.*, 2010; *Gettelman et al.*, 2011).

The TTL has characteristics of both the troposphere and the stratosphere. *Highwood and Hoskins* (1998) describe the TTL as the layer between the level of main convective outflow where the lapse rate is minimal and the cold point tropopause. This definition differs from the more rigid definition described by *Fueglistaler et al.* (2009) in terms of pressure, potential temperature, and altitude. The bottom of the TTL is at 150 hPa, 355 K, and 14 km where the level of zero radiative heating (LZRH), that is the level where the amount of outgoing thermal radiation equals the amount of incoming shortwave radiation, occurs. The top of the TTL is at 70 hPa, 425 K, and 18.5 km where there is a maximum in static stability and at the highest level where clouds are observed. The TTL is bounded laterally by the subtropical jets. According to *Eyring et al.* (2010), the TTL is "maintained by the interaction of convective transport, convectively generated waves, radiation, cloud microphysics and the large-scale stratospheric circulation." Clouds, notably thin cirrus and convective anvils, have significant effects on the radiative balance in the TTL (*Hartmann and Short*, 1980; *Ramaswamy and Ramanathan*, 1989).

The ExUTLS, or lowermost stratosphere, includes the region bounded by the tropopause and the 380 K isentropic potential temperature surface (*Holton et al.*, 1995); refer to Figure 2.3. Due to transport, mixing, and interactions with radiation, the ExUTLS is, chemically speaking, a transition region where the ozone and water vapour concentration gradients are sharpest and opposite; ozone concentrations are high in the stratosphere and low in the troposphere while water vapour concentrations are low in the stratosphere and high in the troposphere (*Gettelman et al.*, 2011).

Some regard the *380 K isentropic surface* as a fourth definition of the tropopause. The 380 K isentropic surface is selected as the upper bounds of the lowermost stratosphere because it corresponds to the level of potential temperature at the tropopause over tropical latitudes. The tropopause

is relatively constant in altitude between 30°S to 30°N and is closely aligned with the 380 K potential temperature surface. Thus, it is sometimes convenient to define the division between the troposphere and the stratosphere at the 380 K potential temperature surface.

In the region below the 380 K potential temperature surface, isentropic surfaces intersect the tropopause in the ExUTLS region as the tropopause height falls with increasing latitude and hence provides a gateway connecting the troposphere and the stratosphere through isentropic displacement of air masses. This exchange across the tropopause along surfaces of constant potential temperature is part of STE, which is a bidirectional process directly affecting the chemistry of the UTLS (*Holton et al.*, 1995).

2.1.5 Molecules, Aerosols, and Cloud Particles

The atmosphere is composed of a number of particles and molecules. Their fractional concentration by volume with respect to dry air are listed in Table 2.1. Together, molecular nitrogen and oxygen account for 99% of the Earth's atmosphere and are the main constituents contributing to the exponential density profile of the atmosphere. At 0.93% per volume, the concentration of argon gas is highest among all noble gases. Water vapour varies in concentration by as much as three orders of magnitude between the coldest and the warmest regions of the Earth's atmosphere. Thus, due to this high variability in water vapour concentration, the percentages of the constituents of air are listed in relation to dry air. (*Wallace and Hobbs*, 2006).

Greenhouse gases, such as water vapour, carbon dioxide, and ozone, are also present in the atmosphere. Due to their molecular structure, greenhouse gases absorb and re-emit thermal radiation and consequently heat up the Earth's atmosphere. The atmosphere is relatively transparent to the incoming shortwave radiation it receives from the Sun. Thus, the Earth's surface is warmed and re-radiates this energy as far infrared longwave thermal radiation. Most of this outgoing radiation is absorbed by the Earth's atmosphere, which is then re-radiated in the upward and downward directions. The downward radiated energy causes heating and hence creates the greenhouse effect. Trace constituents, such as methane, nitrous oxide, carbon monoxide, and chlorofluorocarbons also contribute to the greenhouse effect despite their significant lower concentrations. The absorption bands of these trace gases occupy regions of the spectrum that would otherwise be transparent to outgoing terrestrial radiation. A small increase in the concentration of such trace gases will have a substantially more noticeable impact on the greenhouse effect than an equivalent increase in the concentration of carbon dioxide (*Wallace and Hobbs*, 2006).

Table 2.1: Fractional concentrations by volume of gaseous constituents within the Earth's atmosphere up to an altitude of 100 km with respect to dry air; recreated from *Wallace and Hobbs* (2006).

Constituent [1]	Molecular Weight	Fractional Concentration by Volume
Nitrogen (N_2)	28.013	78.08%
Oxygen (O_2)	32.000	20.95%
Argon (Ag)	39.95	0.93%
Water Vapour (H_2O)	18.02	0 to 5%
Carbon Dioxide (CO_2)	44.01	380 ppm
Neon (Ne)	20.18	18 ppm
Helium (He)	4.00	5 ppm
Methane (CH_4)	16.04	1.75 ppm
Krypton (Kr)	83.80	1 ppm
Hydrogen (H_2)	2.02	0.5 ppm
Nitrous Oxide (N_2O)	56.03	0.3 pmm
Ozone (0_3)	48.00	0 to 0.1 ppm

[1] Greenhouse gases are indicated by bold-faced type.

The presence of aerosols, which are loosely defined as any solid or liquid particle suspended in the atmosphere, within the UTLS region has significant impact on radiative processes. Examples of aerosol particles include soot, minerals, oceanic particles, volcanic dust, smoke from forest fires, and desert sand (*Liou*, 2002). Aerosols affect the UTLS both in a direct and an indirect manner. Directly, the effects on the radiative balance of the atmosphere are twofold. Aerosols scatter visible radiation and thereby increase the planetary albedo, a ratio of scattered sunlight to incoming sunlight, and cool the Earth. In addition, aerosols effectively scatter thermally emitted infrared radiation from the Earth's surface which, through the greenhouse effect, contribute to the planet's warming. This effect, however, is dependent on the size distribution of the aerosol itself. Indirectly, aerosols affect the chemistry of the atmosphere by seeding cloud formation which, in the case of polar stratospheric clouds (PSCs), enables chemical reactions producing chlorine, a catalyst in ozone destruction (*Le Treut et al.*, 1998).

The composition and shapes of cloud particles depend greatly on altitude, temperature, relative humidity, and whether they have undergone collision or coalescence processes (*Liou*, 2002). At low altitudes where cloud base heights are around 2 km in altitude, stratus and cumulous clouds are typically composed of spherical water droplets ranging between 1 and 20 μm is size. At middle altitudes, altostratus and altocumulous clouds have varied composition and particle shapes with altitude. Particles are sometimes liquid and spherical at the base of the cloud and gradually transform into supercooled water droplets as altitude increases and temperature decreases, which eventually leads to ice particles at the cloud top. Irregularly shaped ice crystals are the most common type of aerosol in the UTLS, and at this altitude, they collectively form cirrus clouds. Cirrus clouds typically occur near the tropopause altitude, but are sometimes observed as low as 4 km (*Liou*, 1986). In general, particles at the top of high altitude clouds are small and take the form of refined columns or plates. Near the bottom of these clouds, particle shapes become more complex and irregular taking the form of bullet rosettes and aggregates resulting from particle collisions and coalescence processes due to vertical mixing and gravitational pulling (*Liou*, 2002).

At lower altitudes, clouds formed from water droplets, like typical cumulus clouds, are generally optically thick and behave like blackbodies in the thermal infrared region. These clouds contribute to the albedo effect and cool the atmosphere. On a global basis, the solar albedo effect decreases the radiation balance by 56 Wm^{-2} and the infrared greenhouse effect increases it by 40 Wm^{-2} for a net cooling of 16 Wm^{-2} (*Herman et al.*, 1980). In support of *Herman et al.* (1980), *Hartmann and Short* (1980) and *Ohring and Clapp* (1980) show the albedo effect dominates at the top of the

atmosphere where an increase in the fractional cloud coverage will cool the Earth.

Cirrus clouds, which are optically thin, are formed from large non-spherical ice crystals in low concentration and are non-black in the thermal infrared region (*Liou*, 1986). These high altitude clouds contribute to the greenhouse effect because of the location of their occurrence, low reflectivity to incoming solar radiation, and low optical thickness (*Manabe and Strickler*, 1964).

The current understanding of clouds within the climate and weather systems still has uncertainty. It is generally understood the greenhouse effect leading to a net warming of the atmosphere dominates (*Wang et al.*, 1996; *Sassen et al.*, 2009), but the local radiative budget is subject to the Earth-atmosphere conditions in regions where clouds exist and on the geometric and physical compositions of the clouds (*Liou*, 1986).

2.2 Measurements of Tropopause Level Clouds

2.2.1 Motivation: Cirrus Clouds

Clouds have a profound influence on climate (*Chahine*, 1992; *Liou*, 1992; *Hobbs*, 1993). A comprehensive description of clouds requires information on their physical location and distribution, size, lifetime, occurrence frequency, and optical properties like particle size distribution, composition, shape, and refractive index (*Wang et al.*, 1996).

As *Sassen et al.* (1989) explain, cloud visibility, which is based on physiological perception of colour and contrast, depends on various factors like the viewing geometry of the instrument, the relative levels of target and background illumination, and the dependence of the scattering phase function on scattering angle for cloud particles. Using a ground-based zenith-pointing lidar system, *Sassen and Cho* (1992) group clouds into three categories based on the cloud's optical thickness, τ, which is described in Section 2.6.2. Daytime measurements consist of subvisual clouds ($\tau < 0.03$), threshold visible ($\tau \approx 0.03$), and thin cirrus ($\tau > 0.03$). *Wang et al.* (1996) use occultation measurements of clouds and broaden these classifications into two categories: subvisual ($\tau \leq 0.03$) and opaque ($\tau > 0.03$) clouds.

Compared to convective clouds, cirrus clouds are more commonly found in the TTL (*Dessler and Yang*, 2003) as they sometimes result from extensive convective anvil remnants once the cumulus cloud has dispersed (*Liou*, 1986; *Dessler and Yang*, 2003; *Sassen et al.*, 2008). The anvils are associated with the Intertropical Convergence Zone (ITCZ) (*Mace et al.*, 2006; *Sassen et al.*, 2008) and convective monsoonal cycles. As *Ludlam* (1948) and *Heymsfield* (1993) describe, subvisual

cirrus clouds can be formed in situ from rising moist air masses. A parcel of air containing water vapour may be lifted by convective motions to a higher altitude. The lower temperature at this elevated altitude cools the air mass and causes the water vapour to solidify into ice crystals, which forms cirrus clouds. Latent heat resulting from the ice crystal growth warms the localized parcel of air, which then carries the cloud further to a higher altitude. In situ formation of cirrus clouds causes the shapes and structures to vary (*Pfister et al.*, 2001).

Cirrus clouds residing at high altitudes near the tropopause and their effects on the atmosphere are poorly understood. At any given time, cirrus clouds cover a minimum of 40% (*Liou*, 1986; *Wang et al.*, 1996) to 60% (*Wylie et al.*, 2005) of the globe. Cirrus clouds act as regulators of the Earth's radiative balance despite their thin characteristics (*Liou*, 1986; *Liou et al.*, 2002). They assume a role in STE (*Corti et al.*, 2006) and in the regulation of water vapour in the UTLS (*Dessler and Minschwaner*, 2007; *Dessler*, 2009) but the intricate manner and extent in which they are involved remain unsolved.

In this work, obtaining measurements of the occurrence frequency and distribution of high-altitude clouds is explored. Subvisual cirrus clouds are invisible to the naked eye when viewed from the ground and have low optical thickness relative to some threshold value suitable for visible clouds (*Sassen et al.*, 1989). Standard observation techniques, like remote nadir sounding and ground-based zenith lidar systems, have difficulty viewing subvisual cirrus clouds particularly because they are thin in nature and often show little contrast relative to their background. Subvisual clouds are more easily detected with alternative viewing geometries from satellites, such as that employed for the limb scattering technique.

2.2.2 Limb Scattering Technique

Although it is difficult to physically access parts of the atmosphere and space, scientists and engineers use a number of instruments to measure and observe phenomena. Prior to the 1960's, balloons, probes, and ground stations were often used to sample the atmosphere. The technique of atmospheric spectroscopy, which entails the study of the interaction between solar radiation and the atmosphere for a range of wavelengths, is used to identify the makeup of the atmosphere. Since then, aeronomy has grown considerably, especially in the 1960's with the launch of artificial satellites and the development of new techniques for space observations. Today, while older techniques are still being used, the combination of spectroscopy with a satellite remote sensing technique is an efficient way to obtain atmospheric signatures providing quantitative information on a global basis.

The solar or stellar occultation remote sensing technique uses the concept of measuring the attenuation of light emitted from a sun or a star from space as it passes through the atmosphere of a planet under investigation. Sunlight, which is composed of a range of wavelengths and energies, penetrates the atmosphere which behaves like a filter. Certain wavelengths of the solar radiation are absorbed and scattered and the resulting signature provides information about the composition of the planet's atmosphere.

Alternatively, some satellites use the limb scattering remote sensing technique where, instead of observing a sun or a star directly, the sunlit limb is observed. The limb scattering viewing geometry is similar to that of the occultation technique, however rather than looking toward the sun, the line of sight is directed through the atmosphere in order to measure scattered sunlight. That is, the line of sight is pointed at a tangent altitude within the atmospheric limb. The concept is that the solar spectrum is imprinted with the signatures of atmospheric composition as it is scattered by molecules and particles along its path through the atmosphere. Vertical profiles are typically obtained in one of two ways: a singular line of sight is scanned through successive tangent altitudes, or multiple lines of sight are imaged concurrently (*Bourassa*, 2007).

There are two major assets to the limb scattering technique. Limb scattering provides high vertical resolution, similar to the occultation technique, and good global coverage, much like nadir sounding. Conversely, limb scattering is also subject to limitations. Along any infinitesimal layer of the atmosphere, inversion techniques assume the atmosphere is uniform in homogeneous layers along the line of sight. Fast sampling both vertically and along the satellite track and a tomographic retrieval are required to resolve high resolution features (*Degenstein et al.*, 2003, 2004). Also, because multiple scattering complicates the interpretation of the measurements, detailed spherical radiative transfer is required (*Bourassa*, 2007).

The geometry of the limb scattering technique is shown in Figure 2.4 (*Bourassa*, 2007). The smallest altitude distance between the Earth's surface and the line of sight is defined as the tangent altitude. Latitude and longitude coordinates directly below the tangent point are used to locate the measurement. The solar geometry is also defined at the tangent point. The tangent point *solar zenith angle*, θ, is defined as the angle between the zenith direction and the direction pointing toward the Sun. The tangent point *solar azimuth angle*, ϕ, is defined as the angle between the line of sight and the horizontal projection of the solar direction. Finally, the tangent point *solar scattering angle*, Θ, which can be derived from the other two solar angles, is defined as the angle between the line of sight and the solar direction. It is understood that the vector defining the line

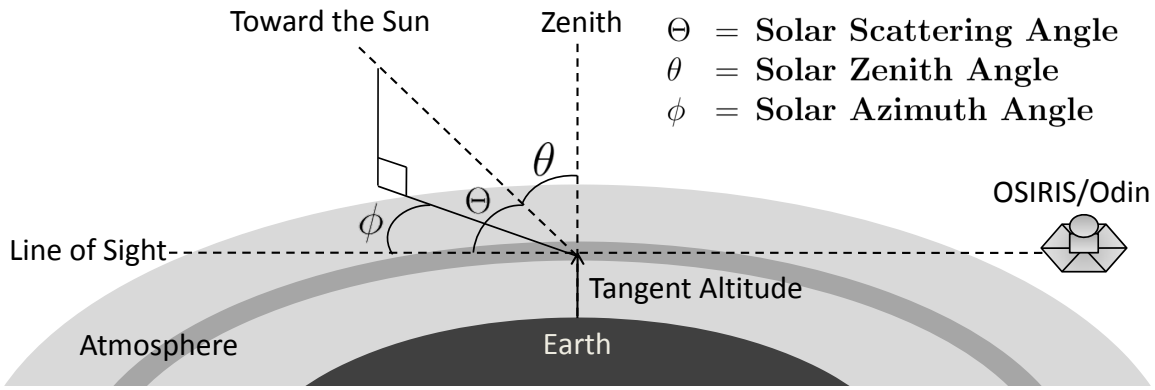

Figure 2.4: Limb scattering geometry; adapted from *Bourassa* (2007).

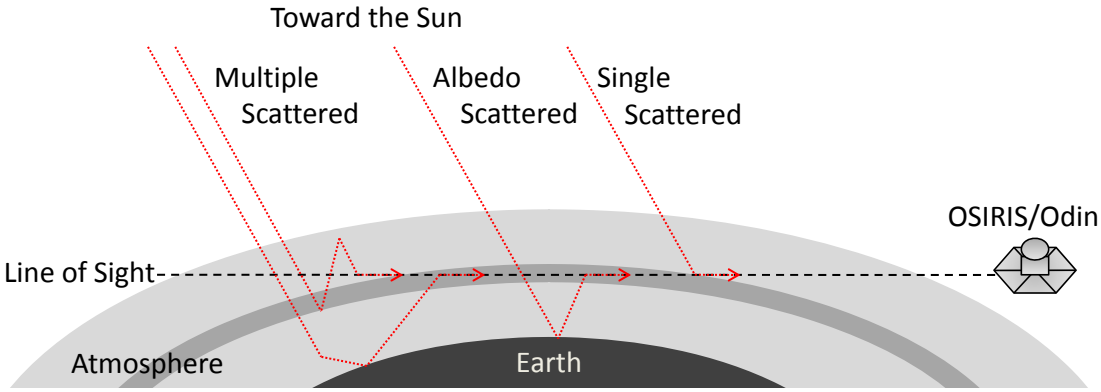

Figure 2.5: The limb scattering technique is based on observing light which has been scattered multiple times and/or from the ground; adapted from *Bourassa* (2007).

of sight is directed away from the satellite.

Figure 2.5 shows how sunlight is scattered into the line of sight of a limb-viewing satellite. Sunlight may be scattered once or multiple times before being scattered into the line of sight, and light can be scattered from any type of atmospheric particle as well as from the surface of the Earth.

2.3 OSIRIS on Odin

The Optical Spectrograph and Infra-Red Imaging System (OSIRIS) (*Llewellyn et al.*, 2004), a Canadian instrument onboard the Swedish Odin satellite (*Murtagh et al.*, 2002), was designed to measure vertical profiles of atmospheric limb radiance of scattered sunlight from the upper troposphere to the lower mesosphere.

2.3.1 Odin

Odin was launched 20 February 2001 into a circular polar orbit about the Earth at an altitude of approximately 600 km with a period of 96 minutes. The satellite follows a sun-synchronous orbit; the plane of orbit is always perpendicular to the Sun, meaning the plane rotates approximately 1° every day. The orbital inclination of 98° from the equator provides near-global coverage as the corresponding sampled latitude range for nominal on-track instrument pointing is from 82°S to 82°N.

The satellite track is always close to the solar terminator implying a dawn/dusk orbit. Odin's track closely follows the local dusk terminator on the ascending track. The local time during the ascending node, namely the northward equatorial crossing, is near 1800 h. The satellite's track follows the local dawn terminator on the descending track and the local time during the descending node, that is during the southward equatorial crossing, is near 0600 h. The satellite's track quickly passes through midday at high northern latitudes and through midnight at high southern latitudes.

The entire atmosphere at the tangent point is illuminated when the solar zenith angle is less than 90°. During the months of May till mid-August, the northern hemisphere is illuminated by the Sun and during the months of November till January the southern hemisphere is illuminated. During the months of February and October, the satellite track is closely aligned with the solar terminator; the solar zenith angle is near 90° at all latitudes, so the Sun is nearly perpendicular to the orbit plane and both hemispheres are largely illuminated (*Murtagh et al.*, 2002).

2.3.2 OSIRIS

OSIRIS, which has been in standard operation since November 2001, is composed of two optical modules: the optical spectrograph (OS) and the infrared imager (IRI). The OS consists of an optical grating and a CCD detector and measures atmospheric limb radiance between 280 and 810 nm with spectral resolution of approximately 1 nm to infer information of the vertical profiles of ozone, nitrogen dioxide, and stratospheric aerosol. There is a gap in the spectrum between 475 and 532 nm due to the order sorter, a transition in optical material to filter high order light diffracted from the grating (*Llewellyn et al.*, 2004). The OS has a single line of sight and vertical profiles from roughly 7 to 110 km in altitude are obtained by nodding the entire spacecraft; this facilitates obtaining observations over a range of tangent altitudes (*Murtagh et al.*, 2002). The OS has a 1 km vertical and approximately 40 km horizontal field of view at the tangent point. Successive measurements are

separated by roughly 2 km tangent altitude. It takes nearly 1.5 minutes to complete a full vertical scan; thus there are about 60 scans per orbit.

The IRI is comprised of three infrared co-aligned single lens interference filter imagers, which observe the limb radiance in one dimension. The imagers operate at 1.263, 1.273, and 1.530 μm where the first two imagers measure molecular oxygen infrared atmospheric band emission while the third imager observes both Rayleigh- and aerosol-scattered sunlight and the OH Meinel vibration-rotation band airglow (*Llewellyn et al.*, 2004). The IRI data is not used in this work.

2.4 Scattered Sunlight

The majority of the light we see does not come directly from its source. Rather, our eyes view light that has undergone a process called *scattering*. Objects are visible because of the light they scatter. The Earth's surface, the atmosphere, and clouds also scatter light. Many phenomena occurring in the sky, such as rainbows, haloes, coronas, white clouds, and the blue nature of the sky, result from the scattering of sunlight (*Wallace and Hobbs*, 2006; *Liou*, 2002). As *Liou* (2002) explains, "scattering is a fundamental physical process where light interacts with matter." The physical process of scattering occurs when the light's energy is absorbed and is re-directed or radiated in another direction. Thus, the scattering object is like a localized point source of scattered energy (*Liou*, 2002).

Consider the schematic shown in Figure 2.6. Light incident on a particle at position A is scattered in all directions where the light scattered in the **d** direction has undergone first order scattering. Some of the remaining scattered light is directed toward the particle at position B, which also scatters light in all directions. The light scattered in the **d** direction from the particle at position B has undergone second order scattering. Third order scattering occurs when light scattered from the particle at position B toward the particle at position C is further scattered into the **d** direction from the particle at position C. Light scattered more than once is called *multiple scattering*, a process deeply involved with the transfer of radiant energy in the atmosphere particularly at ultraviolet to visible wavelengths (*Liou*, 2002).

There are many particles with a wide variety of shapes and sizes in the atmosphere. For example, there are gas molecules as small as 10^{-4} μm, aerosols between 0.1 and 1 μm in size, cloud particles 1 to 50 μm in diameter, ice crystals between 10 and 100 μm in size, water droplets 0.1 to 3 mm in diameter, and hailstones on the order of 1 cm (*Petty*, 2004). The size of the scattering object,

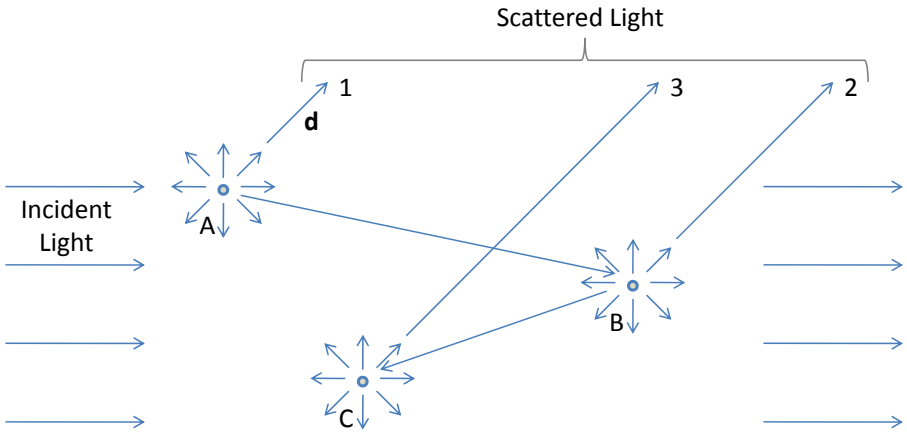

Figure 2.6: Schematic showing multiple scattering events with first (A), second (B), and third (C) order scattering in the **d** direction; adapted from *Liou* (2002).

in particular, is important. When the particle size is very small compared to the wavelength, the particle is a poor scatterer (*Wallace and Hobbs*, 2006; *Petty*, 2004). When the particle is much larger than the wavelength, the laws of refraction, reflection, and absorption can be used and the techniques of ray-tracing and geometric optics apply (*Petty*, 2004).

Most atmospheric particles fall between these two extremes. Rayleigh scattering, the scattering of particles much smaller than the wavelength, characterizes molecular scattering; Mie scattering, the scattering from spherical particles of size comparable to the wavelength, characterizes aerosol scattering; and cloud particle scattering, the scattering of light from irregularly shaped particles such as cloud particles, cover most atmospheric particles and will be described in some detail below.

2.4.1 Key Properties

The appropriate scattering regime and the directionality of the scattering depend greatly on the properties of the scattering object: size, shape, and refractive index (*Petty*, 2004). Small particles relative to the incoming wavelength are likely to scatter equally in the forward and backward directions. As the particle size increases in comparison to the wavelength, forward scattering becomes predominant. Further, as the particle shape deviates from that of a perfect sphere, the scattering features and directionality become increasingly complex.

The scattering regime is selected in accordance to the size parameter, x, which is a ratio between the radius of the particle, a, and the wavelength, λ,

$$x \equiv \frac{2\pi a}{\lambda}. \tag{2.18}$$

The size parameter is used to characterize the significance of scattering. When $x \ll 1$, the Rayleigh scattering regime applies; when $0.1 \leq x \leq 50$, the Mie scattering regime applies; and when $x > 50$, scattering by cloud particles and geometric optics occur (*Wallace and Hobbs*, 2006; *Liou*, 2002).

The shapes of particles can vary greatly. Smaller particles are typically approximated as spheres, but as the size of the particles increases, their shapes typically become more complex. Aerosols, such as ice crystals, snowflakes, soot, and dust have highly irregular shapes (*Petty*, 2004). About 75% of particles within cirrus clouds are columns and bullet rosettes while the remaining 25% are plates and range in size between 100 to 1000 μm (*Liou*, 1986). The shapes of ice crystals are highly dependent on temperature, relative humidity, and whether they evolve through collision or coagulation processes (*Liou*, 2002).

The relative refractive index, m, is a ratio between the complex indices of refraction of the particle and of the surrounding medium, N_1 and N_2 respectively,

$$m = \frac{N_2}{N_1}. \tag{2.19}$$

To generalize, the real part describes the phase speed of the propagating wave within the material and the imaginary part describes absorption. Typically, N_1 is set to one for particles suspended in air so that $m \approx N_2$. The refractive index of the particle is a function of wavelength and depends on the composition of the particle itself (*Petty*, 2004).

2.4.2 Scattering Regimes

Rayleigh Scattering

In 1871, Lord Rayleigh explored the scattering of solar radiation from air in terms of molecular oscillators. Consider a small homogenous, isotropic, spherical particle with radius a. The dimensionless size parameter, $x = \frac{2\pi a}{\lambda}$, characterizes the ratio between the molecular radius and the incident wavelength, λ. The Rayleigh scattering regime is when $x \ll 1$ (*Wallace and Hobbs*, 2006; *Liou*, 2002) where the radius is so small that the particle can be approximated as a sphere. When an electromagnetic wave is incident on the particle, the homogeneous electric field, $\vec{\mathbf{E}}_0$, called the applied field, creates a small electric dipole within the particle. Positive charges are slightly displaced in the direction of the electric field vector while negative charges are displaced in the direction opposite to the electric field vector. The electric field of the particle, which is caused by the electric dipole, interacts with the applied electric field inside and near the particle. The total field, $\vec{\mathbf{E}}$, is then a combination of the applied and the particle's fields and has units charge per area. This electric

dipole induces a dipole moment, $\vec{\mathbf{p}}_0$, with units charge times length. The dipole moment of a small spherical particle is proportional to the strength of the applied electric field,

$$\vec{\mathbf{p}}_0 = \nu \vec{\mathbf{E}}_0, \tag{2.20}$$

where ν is the polarizability and has dimensions of volume. The polarizability depends on the composition and size of the particle and on the frequency of the incident wave. Typically, ν is a 3x3 tensor when $\vec{\mathbf{p}}_0$ and $\vec{\mathbf{E}}_0$ are not aligned. However, for spherical particles composed of electrically isotropic constituents, such as water, the vectors $\vec{\mathbf{p}}_0$ and $\vec{\mathbf{E}}_0$ coincide, which reduces ν to a scalar (*Liou*, 2002; *Petty*, 2004).

The strength and orientation of the induced oscillating electric dipole vary with the incident electric field. In response, the orienting dipole generates its own plane-polarized electromagnetic wave, called the scattered wave, which propagates at the speed of light. The scattering process is elastic where the incident and scattered wavelengths are identical. *Petty* (2004) outlines five key points regarding the incident and scattered electromagnetic waves:

1. The electric field vector is perpendicular to the propagation direction, $\hat{\mathbf{\Omega}}$.

2. The induced dipole moment, $\vec{\mathbf{p}}_0$, is also perpendicular to the propagation direction, $\hat{\mathbf{\Omega}}$, provided the vectors $\vec{\mathbf{p}}_0$ and $\vec{\mathbf{E}}_0$ coincide and ν is a scalar.

3. The electric field vector of the scattered wave, $\vec{\mathbf{E}}_{scat}$, is in the plane containing the scattered electric dipole moment, $\vec{\mathbf{p}}$, and the scattered direction, $\hat{\mathbf{\Omega}}'$.

4. The strength of the electric field at the observation point is proportional to $\sin\gamma$, where γ is the angle between the scattered dipole moment, $\vec{\mathbf{p}}$, and the direction of observation. When referring to the perpendicular and parallel components, $\gamma_\perp$ and $\gamma_\parallel$ are used, respectively.

5. An oscillating dipole induces a vibrating electric field where its amplitude is proportional to the square of the frequency of vibration. That is, the power radiated by the dipole is proportional to the acceleration of the electric charge in the dipole.

Using these five points and referring to the classical electromagnetic solution given by *Hertz* (1889), the scattered electric field, $\vec{\mathbf{E}}_{scat}$, is proportional to the acceleration of the scattered dipole moment, $\vec{\mathbf{p}}$, and to $\sin\gamma$ and is inversely proportional to the distance between the dipole and the observation point, r,

$$\vec{\mathbf{E}}_{scat} = \frac{1}{c^2}\frac{1}{r}\frac{\delta^2\vec{\mathbf{p}}}{\delta t^2}\sin\gamma, \tag{2.21}$$

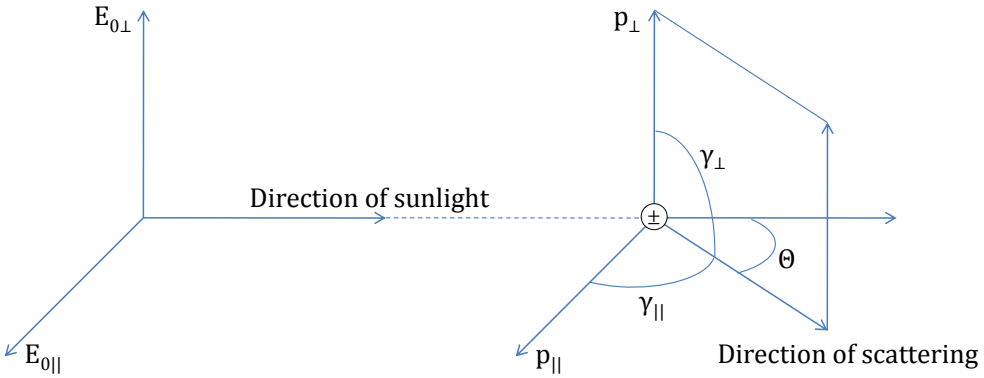

Figure 2.7: Scattering by a dipole. The scattering plane is defined by the directions of the incident and scattering waves and the electric field vectors can be separated into two orthogonal components such as the perpendicular, $\perp$, and parallel, $\parallel$, components to the scattering plane. $\gamma_\perp = \frac{\pi}{2}$ and Θ is the scattering angle; adapted from *Liou* (2002).

where c is the speed of light (*Liou*, 2002). In an oscillating periodic field, the scattered dipole moment, $\vec{\mathbf{p}}$, is expressed in terms of the induced dipole moment, $\vec{\mathbf{p}}_0$,

$$\vec{\mathbf{p}} = \vec{\mathbf{p}}_0 e^{-ik(r-ct)}, \tag{2.22}$$

where $k = \frac{\omega}{c}$ is the wavenumber in terms of the angular frequency, ω, and the exponential component takes the oscillating effect from the electric field into account. Using Equations 2.20 and 2.22, Equation 2.21 becomes,

$$\vec{\mathbf{E}}_{scat} = -\vec{\mathbf{E}}_0 \frac{e^{-ik(r-ct)}}{r} k^2 \nu \sin\gamma, \tag{2.23}$$

(*Liou*, 2002).

Referring to Figure 2.7, the scattering plane is defined by the directions of the incident and scattered waves and the electric vectors can be separated into two orthogonal components such that the perpendicular, $E_\perp$, and parallel, $E_\parallel$, components to the scattering plane are,

$$E_\perp = -E_{0\perp} \frac{e^{-ik(r-ct)}}{r} k^2 \nu \sin\gamma_\perp, \tag{2.24}$$

$$E_\parallel = -E_{0\parallel} \frac{e^{-ik(r-ct)}}{r} k^2 \nu \sin\gamma_\parallel, \tag{2.25}$$

which hold for scattering by spherical, isotropic, homogeneous particles. Here, Θ is the angle between the incident and scattered waves, called the *scattering angle*, and $\gamma_\perp = \frac{\pi}{2}$ and $\gamma_\parallel = \frac{\pi}{2} - \Theta$. Since the scattered dipole moment is always perpendicular to the r direction in the scattering plane, $\gamma_\perp$ will always equal $\frac{\pi}{2}$. Therefore, in matrix notation,

$$\begin{bmatrix} E_\perp \\ E_\parallel \end{bmatrix} = -\frac{e^{-ik(r-ct)}}{r} k^2 \nu \begin{bmatrix} 1 & 0 \\ 0 & \cos\Theta \end{bmatrix} \begin{bmatrix} E_{0\perp} \\ E_{0\parallel} \end{bmatrix}, \tag{2.26}$$

(*Liou*, 2002).

The power per unit area, otherwise known as the intensity, $\mathcal{I}$, is proportional to the square of the electric field amplitude,

$$\mathcal{I} \propto |E|^2. \tag{2.27}$$

Therefore, from Equations 2.24 and 2.25, the polarized intensities of the perpendicular, $\mathcal{I}_\perp$, and parallel, $\mathcal{I}_\parallel$, components are,

$$\mathcal{I}_\perp = \mathcal{I}_{0\perp} \frac{k^4 \nu^2}{r^2}, \tag{2.28}$$

$$\mathcal{I}_\parallel = \mathcal{I}_{0\parallel} \frac{k^4 \nu^2 \cos^2 \Theta}{r^2}. \tag{2.29}$$

The total scattered intensity, $\mathcal{I}$, is the summation of the orthogonal components,

$$\mathcal{I} = \mathcal{I}_\perp + \mathcal{I}_\parallel = (\mathcal{I}_{0\perp} + \mathcal{I}_{0\parallel} \cos^2 \Theta) \frac{k^4 \nu^2}{r^2}. \tag{2.30}$$

For sunlight, which is unpolarized, $\mathcal{I}_{0\perp} = \mathcal{I}_{0\parallel} = \frac{\mathcal{I}_0}{2}$, so the total scattered intensity of unpolarized sunlight scattered by molecules yields,

$$\mathcal{I} = \frac{\mathcal{I}_0}{r^2} \nu^2 \left(\frac{2\pi}{\lambda} \right)^4 \frac{1 + \cos^2 \Theta}{2}, \tag{2.31}$$

recalling that $k = \frac{2\pi}{\lambda}$. Equation 2.31 is the formula describing Rayleigh scattering of sunlight by molecules and was first derived by Rayleigh himself. Notice how the intensity of the unpolarized light is proportional to the intensity of the incident light, $\mathcal{I}_0$, and is inversely proportional to the distance between the scattering point and the observation point, r. Also, since $k = \frac{2\pi}{\lambda} = \frac{\omega}{c}$, the intensity of the scattered light is proportional to the fourth power of the frequency of the incident radiation and the expression for the scattering efficiency is proportional to λ^{-4}, indicating a strong wavelength dependence. As a ray of sunlight penetrates the atmosphere, violet and blue light, which have relatively short wavelengths, are strongly scattered laterally out of the beam compared to orange and red light, which explains the blue nature of the sky (*Liou*, 2002).

Scattering Phase Function

Referring to Equation 2.28, the scattering intensity is isotropic and independent of the scattering angle, Θ, in the scattering plane for vertically ($\perp$) polarized incident light. However, Equation 2.29 shows that the scattering intensity for horizontally ($\parallel$) polarized incident light is a function of $\cos^2 \Theta$. For unpolarized light, the scattering intensity depends on $(1 + \cos^2 \Theta)$. For Rayleigh scattering, the scattering intensity is maximized in the forward and backward directions, that is for

$\Theta = 0$ and $\Theta = \pi$ respectively, and is minimized in the side directions when $\Theta = \frac{\pi}{2}$ and $\Theta = \frac{3\pi}{2}$. The scattering pattern is symmetrical in three-dimensional space due to the spherical symmetry of the particle (*Liou*, 2002).

To properly characterize the scattering pattern as a function of scattering angle, Θ, it is common to define a *phase function*, $P(\cos\Theta)$, which is non-dimensional and its integral over all angles is normalized to unity,

$$\int_0^{2\pi}\int_0^{\pi} \frac{P(\cos\Theta)}{4\pi} \sin\Theta \, \mathrm{d}\Theta \, \mathrm{d}\phi = 1. \tag{2.32}$$

In broad terms, the phase function describes the amount of scattering along a direction and is dependent on the characteristics of the scattering object. For Rayleigh scattering of unpolarized light, the phase function is,

$$P(\cos\Theta) = \frac{3}{4}(1 + \cos^2\Theta). \tag{2.33}$$

The intensity of the scattered light in Equation 2.31 can be expressed in terms of the phase function from Equation 2.33,

$$\mathcal{I}(\cos\Theta) = \frac{\mathcal{I}_0}{r^2}\nu^2\frac{128\pi^5}{3\lambda^4}\frac{P(\cos\Theta)}{4\pi}. \tag{2.34}$$

By this equation, the scattering intensity is directly proportional to the scattering phase function (*Liou*, 2002).

Mie Scattering

When the wavelength, λ, of the incident plane electromagnetic wave approaches the radius of the spherical particle, a, the Rayleigh solution no longer applies. In 1908, Gustav Mie published the solution describing scattering from a dielectric sphere with comparable size to the incoming wavelength, that is for $0.1 \leq x \leq 50$ where $x = \frac{2\pi a}{\lambda}$. The refractive index, m, of the scattering particle may not necessarily be purely real as it it for Rayleigh scattering, which is key to the Mie scattering regime. A non-zero imaginary component of the refractive index implies absorption of radiation by the particle, so the Mie regime accounts for both scattering and absorption of the incident ray.

Using Maxwell's equations, the vector wave equation is derived in spherical coordinates (r, θ, ϕ),

$$\vec{\nabla}^2\vec{\mathbf{A}} + k^2m^2\vec{\mathbf{A}} = 0, \tag{2.35}$$

where $\vec{\mathbf{A}}$ is either the electric, $\vec{\mathbf{E}}$, or magnetic, $\vec{\mathbf{H}}$, field vector, and $k = \frac{2\pi}{\lambda}$ is the wavenumber.

Solutions are obtained using φ, which satisfies the scalar wave equation,

$$\nabla^2\varphi + k^2m^2\varphi = 0, \tag{2.36}$$

and consist of orthogonal combinations of the electric and magnetic field vectors. The scalar wave equation is written in spherical coordinates such that φ is a separable differential equation,

$$\varphi(r,\theta,\phi) = R(r)\Theta(\theta)\Phi(\phi). \tag{2.37}$$

The incident plane wave is expanded in terms of spherical harmonics and the boundary conditions are applied to assure the total transverse component of the electromagnetic field is continuous at the surface of the dielectric sphere. The result is an analytical solution which comprises an infinite series of orthogonal basis functions such as trigonometric functions to account for the ϕ dependence, spherical Bessel functions for the r dependence, and associated Legendre polynomials for the $\cos\Theta$ dependence (*Petty*, 2004). The far-field solution, that is when observing at a distance much greater than the radius of the particle, gives the extinction and scattering efficiencies, $Q(a)$ and $Q_{scat}(a)$ respectively, as well as the scattering phase function, $P(\cos\Theta)$, all of which are functions of the particle radius, a, The efficiencies are,

$$Q(a) = \frac{2}{(ka)^2}\sum_{n=1}^{\infty}(2n+1)\Re(A_n + B_n), \tag{2.38}$$

$$Q_{scat}(a) = \frac{2}{(ka)^2}\sum_{n=1}^{\infty}(2n+1)(|A_n|^2 + |B_n|^2), \tag{2.39}$$

where A_n and B_n are the coefficients of the scattering wave in terms of the normalized half-integral-order Bessel functions, $\psi_n(ka)$, and Hankel functions, $\xi_n(ka)$,

$$A_n = \frac{\psi_n'(mka)\psi_n(ka) - m\psi_n(mka)\psi_n'(ka)}{\psi_n'(mka)\xi_n(ka) - m\psi_n(mka)\xi_n'(ka)}, \tag{2.40}$$

$$B_n = \frac{m\psi_n'(mka)\psi_n(ka) - \psi_n(mka)\psi_n'(ka)}{m\psi_n'(mka)\xi_n(ka) - \psi_n(mka)\xi_n'(ka)}, \tag{2.41}$$

and m is the index of refraction. The expression for the scattering efficiency is an infinite series that converges slowly and exhibits a damped oscillatory behaviour. The scattering phase function is derived analytically in a similar manner.

The cross sectional area, $\sigma(a)$, of the particle is obtained from the efficiencies,

$$\sigma(a) = \pi a^2 Q(a), \tag{2.42}$$

$$\sigma_{scat}(a) = \pi a^2 Q_{scat}(a) \tag{2.43}$$

where $\sigma_{scat}(a)$ is the scattering cross section. Due to the conservation of energy, the absorption cross section, $\sigma_{abs}(a)$, and efficiency, $Q_{abs}(a)$, are determined,

$$\sigma_{abs}(a) = \sigma(a) - \sigma_{scat}(a), \tag{2.44}$$

$$Q_{abs}(a) = Q(a) - Q_{scat}(a). \tag{2.45}$$

In the Mie scattering regime, scattering depends weakly on wavelength and light is strongly forward scattered compared to Rayleigh scattering.

Scattering by Cloud Particles

Particles with a large size parameter, namely for $x > 50$, are subjected to cloud particle scattering. In this work, cloud particle scattering applies to very large irregularly shaped ice crystals, which, due to their large size, cannot be approximated as spheres. Because Mie scattering applies to spherical particles alone, a more accurate regime needs to be implemented to properly characterize the scattering process. A numerical method for computing non-spherical scattering must be based on solving Maxwell's equations with boundary conditions describing the optical properties of the scattering particle. Out of necessity, several methods have been developed over the last couple of decades to further the advancement of various fields such as remote sensing, astrophysics, engineering, medicine, and biophysics.

The T-matrix approach developed by *Waterman* (1971) is a contemporary method that uses a transformation matrix to linearly relate the scattered and incident field coefficients. Beginning with a plane electromagnetic wave incident on a non-spherical particle, the incident and scattered fields are described in terms of vector spherical functions, which involve spherical Hankel and Bessel functions, and expansion coefficients of the vector spherical basis functions of the incident, $\vec{\mathbf{a}}$ and $\vec{\mathbf{b}}$, and scattered, $\vec{\mathbf{p}}$ and $\vec{\mathbf{q}}$, waves. Due to the linearity of Maxwell's equations and the boundary conditions, the expansion coefficients of the incoming and scattered waves are linearly related and form the T-matrix known as the transformation matrix, $\vec{\mathbf{T}}$. In matrix notation,

$$\begin{bmatrix} \vec{\mathbf{p}} \\ \vec{\mathbf{q}} \end{bmatrix} = \vec{\mathbf{T}} \begin{bmatrix} \vec{\mathbf{a}} \\ \vec{\mathbf{b}} \end{bmatrix} = \begin{bmatrix} \vec{\mathbf{T}}^{11} & \vec{\mathbf{T}}^{12} \\ \vec{\mathbf{T}}^{21} & \vec{\mathbf{T}}^{22} \end{bmatrix} \begin{bmatrix} \vec{\mathbf{a}} \\ \vec{\mathbf{b}} \end{bmatrix}, \tag{2.46}$$

The elements in the T-matrix depends solely on the physical and geometric properties of the scattering particle; they are described by the shape, size parameter, and refractive index of the irregularly shaped particle as well as its orientation with respect to the defined coordinate system. As the

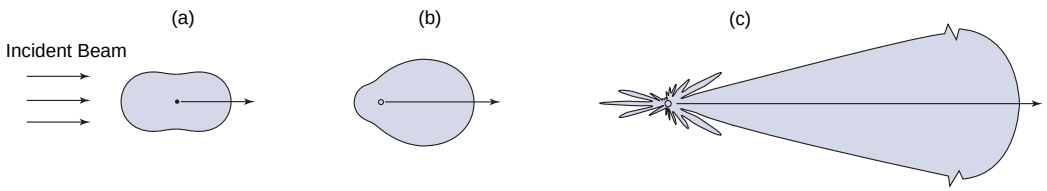

Figure 2.8: Schematic showing the angular distribution of scattered intensity from spherical aerosols by visible light of wavelength 0.5 μm for (a) Rayleigh (10^{-4} μm), (b) Mie (0.1 μm), and (c) cloud particle (10 μm) scattering regimes; adapted from *Liou* (2002).

elements of the T-matrix are independent of the incident and scattered wave, the matrix need be computed once and can then be reused in further calculations for light incident and scattered in different directions (*Mishchenko et al.*, 1996).

Scattering Regime Comparison

Figure 2.8 illustrates three aerosol scattering regimes: Rayleigh scattering with $a = 10^{-4}$ μm, Mie scattering with $a = 0.1$ μm, and cloud particle scattering with $a = 10$ μm, where a is the particle radius. The forward scattering pattern for the 10 μm aerosol is extremely large and is scaled for presentation (*Liou*, 2002). Figure 2.9 shows how the phase function varies with scattering angle for Rayleigh, Mie, and cloud particle scattering for two wavelengths, namely 532 and 800 nm. Rayleigh scattering is nearly isotropic for all scattering angles while Mie and cloud particle scattering are predominantly forward scattering, as described above.

The range of OSIRIS solar scattering angle, Θ, is somewhat limited by the polar inclination of the orbit. For our analysis which focuses on tropical latitudes, the OSIRIS scattering angle is typically near 60° for measurements made on the ascending track and near 120° for measurements made on the descending track. These angles are noted in Figure 2.9 (*Bourassa et al.*, 2007).

2.5 Absorption

Light does not solely experience scattering but also undergoes *absorption*, a process where the radiative energy is transferred to the particle. Physical objects are visible due to the light they scatter but also in part to the light they absorb. For example, a rose is red because it absorbs light at green and blue wavelengths and scatters light near red wavelengths. Atmospheric particles absorb varying amounts of radiation at different wavelengths and the particle's absorption ability is largely dependent on its absorption cross section, σ_{abs}.

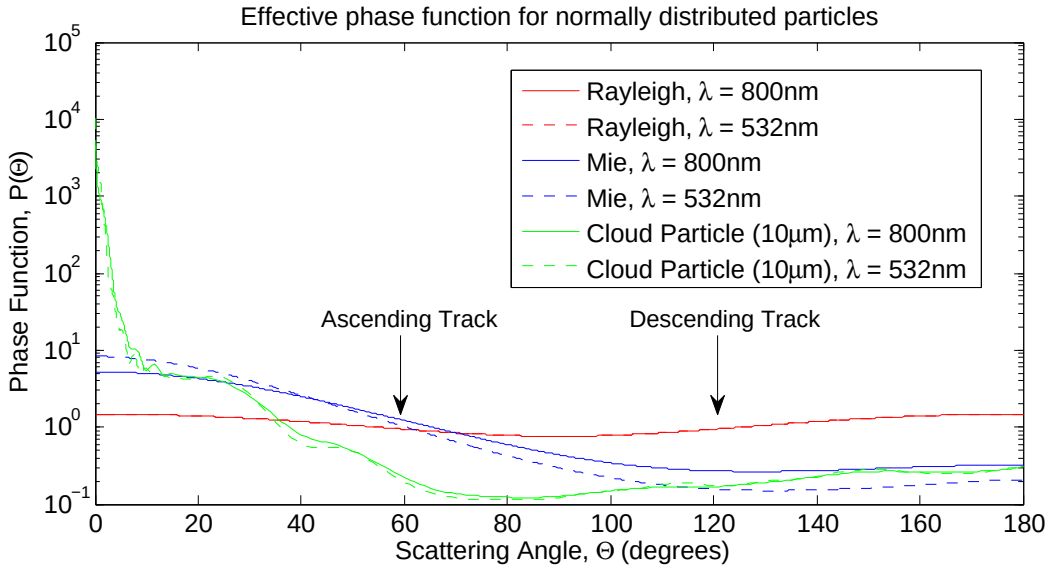

Figure 2.9: Phase function versus scattering angle for Rayleigh, Mie, and cloud particle scattering.

The absorption cross section is often considered as the absorption probability. The absorption of radiation in ice particles, such as those in cirrus clouds, can be neglected because the absorption cross section is very small compared to the scattering cross section at the wavelengths of interest.

2.6 Radiative Transfer and the Atmosphere

2.6.1 Irradiance and Radiance

Monochromatic irradiance, F, otherwise termed the radiant flux density, is defined as the energy, $\mathrm{d}E$, emitted from a surface perpendicular to the direction $\hat{n}$ per unit area, $\mathrm{d}A$, per unit time, $\mathrm{d}t$, per wavelength, $\mathrm{d}\lambda$. Thus, the monochromatic irradiance at position $\vec{r}$ having energy $E = Nhc/\lambda$, where N is the number of photons, h is Plank's constant, and c is the speed of light, is,

$$F(\vec{r}, \hat{n}) = \frac{\mathrm{d}E(\vec{r})}{\mathrm{d}A\,\mathrm{d}t\,\mathrm{d}\lambda}. \tag{2.47}$$

Monochromatic radiance, I, or spectral intensity, is a portion of the irradiance observed when looking at an emitting surface area in the direction $\hat{\Omega}$ over a small solid angle $\mathrm{d}\Omega$. The differential area on the emitting surface decreases by a factor of $\cos\Theta$ when viewed at an angle Θ to the surface normal, $\hat{n}$. Thus, radiance is defined as the energy, $\mathrm{d}E$, incident on a surface normal to the direction

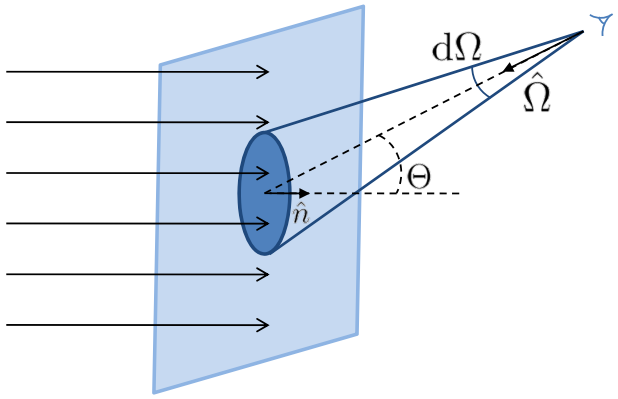

Figure 2.10: Schematic illustrating the difference between irradiance and radiance.

considered, per unit area, $\mathrm{d}A$, per unit time, $\mathrm{d}t$, per wavelength, $\mathrm{d}\lambda$, per unit solid angle, $\mathrm{d}\Omega$,

$$I(\vec{r},\hat{\Omega}) = \frac{\mathrm{d}E}{\mathrm{d}A\cos\Theta\,\mathrm{d}t\,\mathrm{d}\lambda\,\mathrm{d}\Omega}. \tag{2.48}$$

Visualize a surface area that is perpendicular to the direction $\hat{n}$, as shown in Figure 2.10. All the radiation passing through the surface is the irradiance, F. Consider observing the surface in a direction $\hat{\Omega}$ at some position. The radiance, I, consists of all the radiation passing through the surface as seen through the cone $\mathrm{d}\Omega$. The scattering angle, Θ, is the angle between the direction of the surface normal, $\hat{n}$, and the negative of the viewing direction, $\hat{\Omega}$.

2.6.2 Beer-Lambert Law and the Radiative Transfer Equation

Consider an infinitesimal cubic volume of length $\mathrm{d}s$ containing scattering and absorbing particles. As monochromatic radiation passes through the volume the probability of interaction, described by the particle's cross section, $\sigma(s)$, dictates how the light is scattered and absorbed by the particles and can be described by the Beer-Lambert Law. It states that the radiance loss, $\mathrm{d}I$, as the light travels through the volume along the propagation path, s, is also a function of the particle's cross section and the number density, $n(s)$, of the particles,

$$\mathrm{d}I(s) = -I(s)n(s)\sigma(s)\mathrm{d}s. \tag{2.49}$$

If there is more than one species in the volume, each contributing to the absorption and scattering of the incident radiation, the change in radiation is written as a summation over all species, i, as,

$$\frac{\mathrm{d}I(s)}{\mathrm{d}s} = -I(s)\sum_i n_i(s)\sigma_i(s), \tag{2.50}$$

where the summation over all species is known as the extinction,

$$\kappa(s) = \sum_i n_i(s)\sigma_i(s). \tag{2.51}$$

The extinction, which is per unit length, can be decomposed into components contributing to absorption and to scattering,

$$\begin{aligned} \kappa(s) &= \kappa_{abs}(s) + \kappa_{scat}(s), \\ &= \sum_i \left(n_{abs_i}(s)\sigma_{abs_i}(s)\right) + \sum_i \left(n_{scat_i}(s)\sigma_{scat_i}(s)\right). \end{aligned} \tag{2.52}$$

Equation 2.50 can be rearranged and integrated from s to the reference point to give,

$$\int_{I(s)}^{I(0)} \frac{\mathrm{d}I(s)}{I(s)} = -\int_s^0 \kappa(s')\mathrm{d}s'. \tag{2.53}$$

The unit-less expression in the right-hand integral is defined as the differential optical depth, $\mathrm{d}\tau$, which, for a homogenous layer of thickness l, describes the fraction of the radiation attenuated by the layer. Thus, for an incremental path length $\mathrm{d}s$, the radiation is attenuated by,

$$\mathrm{d}\tau(s) = -\kappa(s)\mathrm{d}s = -n(s)\sigma(s)\mathrm{d}s. \tag{2.54}$$

Typically, the optical depth is measured positive in the direction from the reference point, which is define here as $s = 0$, to the position s, therefore removing the negative sign. When Equation 2.54 is substituted into Equation 2.53, the solution is,

$$\begin{aligned} \int_{I(s)}^{I(0)} \frac{\mathrm{d}I(s)}{I(s)} &= \int_{\tau(s)}^{\tau(0)} \mathrm{d}\tau(s'), \\ \ln \frac{I(0)}{I(s)} &= \tau(0) - \tau(s), \end{aligned} \tag{2.55}$$

$$\therefore I(0) = I(s)e^{-\tau(s)}. \tag{2.56}$$

Equation 2.56 describes the absorption and scattering of radiation out of the propagation direction by extinction of the incident beam. However, radiation incident from other directions can also be scattered into the propagation direction, $\hat{\Omega}$, and so increase the radiance. The radiative transfer equation accounts for all positive and negative changes in radiation along the propagation path. A source term, $J(s)$, is added into Equation 2.50 to account for the radiation scattered into the propagation direction,

$$\frac{\mathrm{d}I(s)}{\mathrm{d}s} = \kappa(s)(-I(s) + J(s)). \tag{2.57}$$

The solution yields the integral form of the radiative transfer equation,

$$I(0) = I(s)e^{-\tau(s)} + \int_s^0 \kappa(s')J(s')e^{-\tau(s')}\mathrm{d}s'. \tag{2.58}$$

2.6.3 Scattering in an Optically Thin Atmosphere

In the case of a single scattering event of a solar photon in the atmosphere, such as the first order scattering shown in Figure 2.6, the source term, $J_1(s, \hat{\Omega})$, is,

$$J_1(s, \hat{\Omega}) = \frac{\kappa_{scat}(s)}{\kappa(s)} F_0(\hat{\Omega}_0) e^{-\tau(sun,s)} \bar{P}(s, \hat{\Omega}, \hat{\Omega}_0), \tag{2.59}$$

where $\kappa_{scat}(s)$ is the scattering extinction, $F_0(\hat{\Omega}_0)$ is the solar irradiance, $\tau(sun, s)$ is the optical depth from the Sun to the scattering point, and $\bar{P}(s, \hat{\Omega}, \hat{\Omega}_0)$ is the effective phase function for scattering from the solar direction, $\hat{\Omega}_0$, into the $\hat{\Omega}$ direction and has units per steradian. The radiative transfer equation considering only a single scatter in the atmosphere is,

$$I_1(\vec{r_0}, \hat{\Omega}) = I_1(s_1, \hat{\Omega})e^{-\tau(s_1,0)} + \int_{s_1}^0 \kappa(s)J_1(s, \hat{\Omega})e^{-\tau(s,0)}\mathrm{d}s, \tag{2.60}$$

where $\vec{r_0}$ is the satellite position and s_1 is the position of the single scattering event along s. The exponential $e^{-\tau(s_1,0)}$ in the first term describes the attenuation of light from the scattering position to the observation point where $s = 0$ and the exponential $e^{-\tau(s,0)}$ in the integral describes the attenuation of light along s to the reference point at $s = 0$. The consideration of the single scattering case implies the solar direction, $\hat{\Omega}_0$, is not aligned with the $\hat{\Omega}$ direction; that is the solar radiation must be scattered into the propagation direction and must not initially be aligned with the line of sight. Therefore, the first term in Equation 2.60, which describes radiation emanating from the end of the line of sight, is zero. Similarly, the satellite does not view the Earth's surface, meaning the line of sight does not intersect the Earth's surface, so the $\hat{\Omega}_0$ direction is not aligned with the propagation direction, $\hat{\Omega}$.

If the atmosphere is optically thin, that is if $\tau \ll 1$, then $e^{-\tau} \approx 1$, and,

$$I_1(\vec{r_0}, \hat{\Omega}) \approx \int_{s_1}^0 \kappa(s)J_1(s, \hat{\Omega})\mathrm{d}s. \tag{2.61}$$

The ground scatter component, which is dependent on the albedo, is also an important contribution because the albedo signal can be as bright as the measured signal. However, in an optically thin

atmosphere, the upwelling albedo contribution is approximately equal at all tangent altitudes and the ground scatter component can be accounted for through an altitude normalization.

The integral in Equation 2.61 is largely dominated by the tangent point contribution. Equation 2.61 with the single-scatter source term, Equation 2.59, becomes,

$$\begin{aligned} I_1(\vec{r_0}, \hat{\Omega}) &\approx \kappa(s_T) J_1(s_T, \hat{\Omega}) \Delta s_T, \\ &\approx \kappa_{scat}(s_T) F_0(\hat{\Omega}_0) \bar{P}(s, \hat{\Omega}, \hat{\Omega}_0) \Delta s_T, \end{aligned} \tag{2.62}$$

where Δs_T is the tangent point path length and $\bar{P}(s, \hat{\Omega}, \hat{\Omega}_0)$ is the scattering phase function which describes the probability of scattering in a direction. The radiance for an optically thin atmosphere is proportional to the number density of the scattering particles,

$$I_1(\vec{r_0}, \hat{\Omega}) \approx n_{scat}(s_T) \sigma_{scat}(s_T) F_0(\hat{\Omega}_0) \bar{P}(s, \hat{\Omega}, \hat{\Omega}_0) \Delta s_T. \tag{2.63}$$

When a number of particles and molecules contribute to the scattering of light, the radiance in Equation 2.63 is a sum over each scattering contributor,

$$I_1(\vec{r_0}, \hat{\Omega}) \approx \left[\sum_i n_{scat_i}(s_T) \sigma_{scat_i}(s_T) P_i(s, \hat{\Omega}, \hat{\Omega}_0) \right] F_0(\hat{\Omega}_0) \Delta s_T. \tag{2.64}$$

In the case of an atmosphere containing background molecular nitrogen and oxygen as well as aerosols,

$$I_1(\vec{r_0}, \hat{\Omega}) \approx \left[n_{scat_{\mathrm{m}}}(s_T) \sigma_{scat_{\mathrm{m}}}(s_T) P_{\mathrm{m}}(s, \hat{\Omega}, \hat{\Omega}_0) + n_{scat_{\mathrm{a}}}(s_T) \sigma_{scat_{\mathrm{a}}}(s_T) P_{\mathrm{a}}(s, \hat{\Omega}, \hat{\Omega}_0) \right] F_0(\hat{\Omega}_0) \Delta s_T, \tag{2.65}$$

where the subscripts m and a denote molecular background and aerosol scattering, respectively.

2.7 SASKTRAN

SASKTRAN (*Bourassa et al.*, 2008) is a spherical geometry radiative transfer model designed to simulate limb-scattered solar radiation. It essentially solves the equation of radiative transfer through the method of successive orders for rays travelling within the spherical geometry in order to accurately and efficiently account for the multiple scattering contribution to the limb radiance. The method of successive orders is used to obtain a solution describing light that has undergone multiple scattering by computing scattering solutions recursively. In the previous section, a simplified derivation of the single scatter signal is presented; SASKTRAN is used for where more detailed modelling is required, namely where the single scatter solution does not apply (*Bourassa et al.*,

2008). When modelling the scattering of light by aerosols, SASKTRAN accounts for an altitude dependent cross section and phase function. Absorption by numerous temperature dependent species is also considered in the model. SASKTRAN is used for operational retrievals of ozone, nitrogen dioxide, and aerosols from the OSIRIS measurements. In this work, SASKTRAN is used to model the molecular background within a limb geometry as it accurately takes into account ground and multiple scattering.

Chapter 3

OSIRIS Cloud Detection Technique

The effect cirrus clouds have on the radiative balance of the atmosphere is pivotal; their interaction with incoming solar and outgoing thermal radiation results in a net warming of the atmosphere. Cloud formation affects the distribution of water vapour in the upper atmosphere, which has subsequent effects on the regulation of the climate system below. Therefore, obtaining measurements of the occurrence frequency and distribution of clouds enables an understanding of the radiative processes involved in the regulation of the climate system.

As part of this thesis work, a cloud detection technique was developed using OSIRIS limb scattering measurements. The technique involves obtaining scattering residuals, namely the difference between the measurements using modelled molecular radiance profiles. These residual profiles characterize scattering enhancements. Normalizing histograms of scattering residuals produces probability density functions (PDFs), which reveal the distribution is not a continuum measurement. The separation in the distribution is key to the technique since it provides a clear distinction between the cloudy and cloud-free conditions. Probability maps of cloud occurrence frequency are produced by integrating from the minimum in the distribution over the cloudy condition.

A detailed description of the cloud detection technique is presented in this chapter and results obtained using the technique are compared to those by *Sassen et al.* (2008) who used CALIPSO nadir measurements and to those by *Wang et al.* (1996) who used SAGE II solar occultation measurements of cirrus clouds.

3.1 Scattering Residual and Probability Density Functions

In the limb geometry, the Earth's atmosphere is optically thin down to upper tropospheric tangent altitudes for wavelengths longer than around 700 nm. For this analysis, OSIRIS measurements at 800 nm were used; this is essentially the longest wavelength measured by OSIRIS that is not contaminated by polarization anomalies caused by the grating. The measured radiance, I_{measured},

can be split into two components: that due to the molecular background, $I_{\text{molecular}}$, and due to clouds and aerosols, I_{aerosol}. Recall Equation 2.65 from the previous chapter, which describes the single scatter radiance of an optically thin atmosphere,

$$I_1(\vec{r_0}, \hat{\Omega}) \approx \left[n_{scat_{\text{m}}}(s_T)\sigma_{scat_{\text{m}}}(s_T)P_{\text{m}}(s, \hat{\Omega}, \hat{\Omega}_0) + n_{scat_{\text{a}}}(s_T)\sigma_{scat_{\text{a}}}(s_T)P_{\text{a}}(s, \hat{\Omega}, \hat{\Omega}_0) \right] F_0(\hat{\Omega}_0)\Delta s_T, \tag{2.65}$$

where the subscripts m and a denote the molecular and aerosol components, respectively. Therefore, within the limits of these assumptions,

$$I_{\text{measured}} = I_{\text{molecular}} + I_{\text{aerosol}}. \tag{3.1}$$

The SASKTRAN model was used to approximate the molecular radiance because it incorporates the method of successive orders to satisfy multiple scattering events including ground albedo within a limb scattering spherical geometry. Within the model, an atmosphere free of aerosols and clouds was simulated to obtain molecular background radiance profiles. By comparing the measured radiance profiles from OSIRIS to the modelled ones obtained through SASKTRAN, the radiance contributions from clouds and aerosols were determined.

The measured radiance and modelled molecular radiance profiles were directly compared after employing an altitude normalization. That is, each point on the measured radiance curve was normalized by the measured radiance at a reference tangent altitude while each point on the modelled molecular radiance curve was normalized by the modelled molecular radiance at the same reference tangent altitude. The reference tangent altitude was chosen nearest 35 km because it is typically cloud- and aerosol-free at this altitude and because measurements above this altitude start to become contaminated by larger noise due to exponentially falling signal levels. These two normalized variables are shown in the left hand plot in Figure 3.1(a) for typical OSIRIS scans taken in the southern hemisphere tropical latitudinal region during the summer of 2007. Only scans taken during the descending track of Odin's orbit were considered, which for a short time period and latitude band, the scattering angle is roughly constant.

In a cloud- and aerosol-free atmosphere, the normalized measured radiance, $\tilde{I}_{\text{measured}}$, and the normalized molecular radiance, $\tilde{I}_{\text{modelled}}$, profiles should essentially agree within the accuracy of the optically thin approximation. It was shown in Equation 2.65 that the radiance, I, is related to the concentration of the particles, n, in the gas for an optically thin atmosphere: $I \propto n$. Furthermore, referring to Equation 2.2, pressure, p, is also related to the density, ρ, which is further related to the concentration of the particles in the gas: $p \propto \rho \propto n$. Equation 2.5 shows pressure is exponential

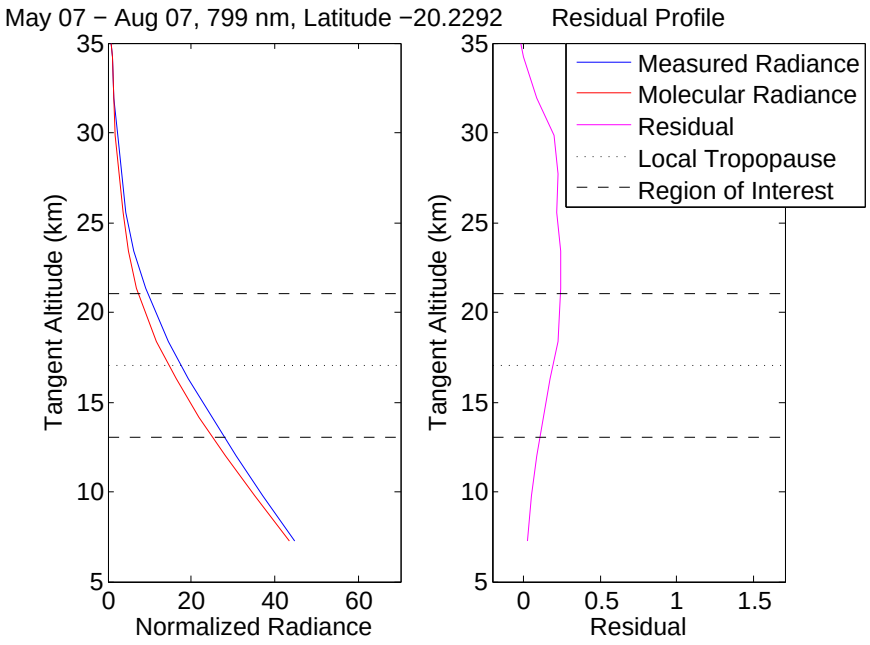

(a) Cloud-free condition

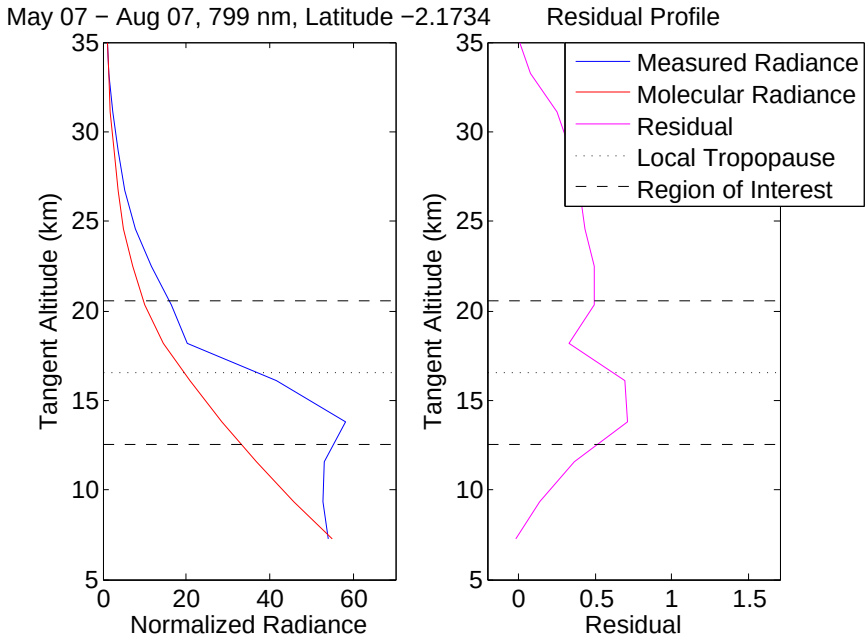

(b) Cloudy condition

Figure 3.1: Normalized radiance, density, and residual profiles as a function of tangent altitude at 800 nm for (a) cloud-free and (b) cloudy conditions.

in altitude, z. Therefore, the radiance must also be approximately exponential in altitude for an optically thin atmosphere.

The discrepancy between the curves within 12 and 35 km tangent altitudes is enhanced scattering due to stratospheric aerosol. Additional discrepancies in the measurements indicate the presence of cloud scattering. Since the scattering of light is increased with the presence of cloud particles, the radiance signal measured by OSIRIS at the cloud altitude is enhanced. The difference between the logarithm of the measured and modelled molecular radiance is here defined as a *scattering residual*, R, that can be used to characterize scattering enhancements,

$$R = \ln\left(\frac{\tilde{I}_{\text{measured}}}{\tilde{I}_{\text{modelled}}}\right). \tag{3.2}$$

Taking the natural logarithmic difference of exponential-like curves as opposed to the straight difference prevents biasing discrepancies at lower tangent altitudes due to the exponential nature of the radiance profiles. In a cloud-free atmosphere, the residual values in the right hand plot of Figure 3.1(a) hover around zero except in the region comprised of stratospheric aerosol. Figure 3.1(b) shows a positive enhancement between 13.7 and 16.1 km tangent altitudes suggesting the presence of clouds.

Residual profiles, such as those shown in the right hand plots of Figure 3.1, were generated and used to create histograms of scattering residuals for altitude and latitude ranges. A histogram peak near zero represents the cloud-free condition. Recall that in the absence of clouds the residual values linger around zero, so collectively they form a histogram peak near zero and represent the cloud-free condition. In the event of a cloud, scattering is enhanced so the residual values are much greater and form a second histogram peak. The histogram was normalized by the total number of measurements to obtain a PDF, shown in Figure 3.2(b). The *Cloud-Free* and *Cloudy* peaks are labelled in the figure. Note the distribution in the residual PDF is not a continuum measurement. Rather, the separation of the peaks, which is a significant result, provides a clear indication of the ability to distinguish the two conditions.

The preceding technique is demonstrated in the following example. For all OSIRIS measurements confined to the northern hemisphere during boreal summer in the year 2007, matching molecular radiance profiles in coordinates and time were modelled using SASKTRAN. Residual profiles were generated as per Equation 3.2 and converted into histograms of scattering residuals for varying altitude and latitude regions of interest. Altitude ranges were defined as layers relative to the local tropopause height, as illustrated in Figure 3.2(a). Latitude ranges were segregated as listed in Table

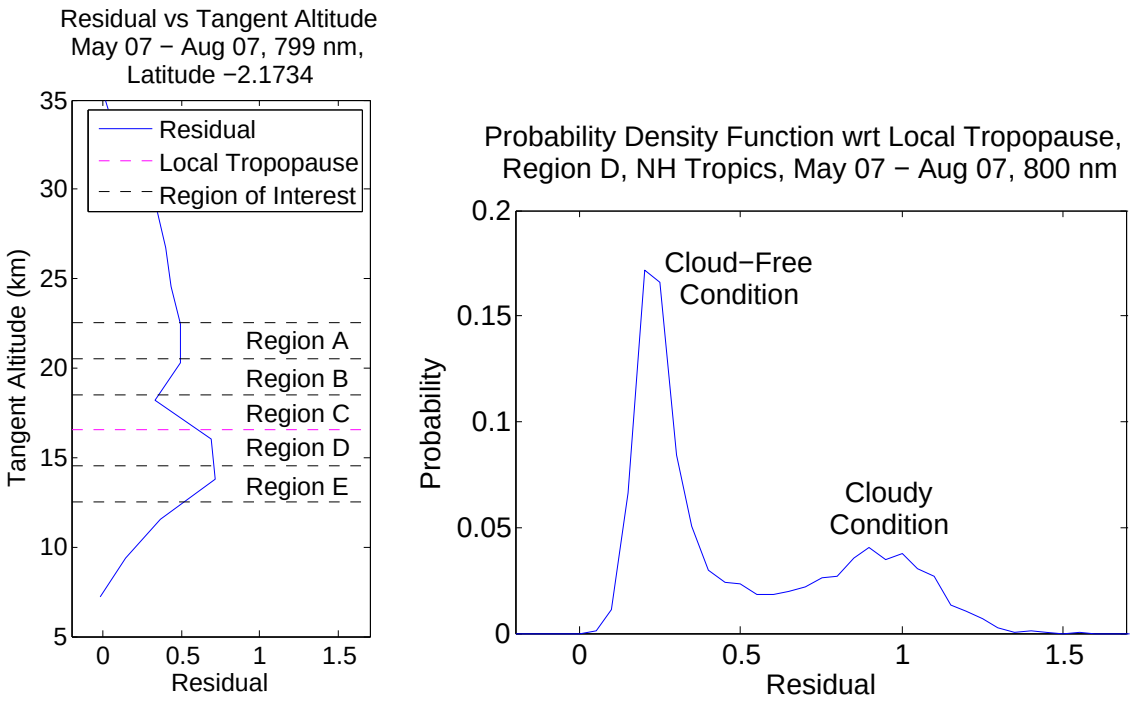

(a) Altitude regions of interest

(b) Probability density function for Region D

Figure 3.2: Residual histograms are determined from normalized residual profiles (800 nm), and normalized to obtain probability density functions: (a) Normalized residual profile showing five altitude regions of interest. (b) Probability density function for Region D for scans taken during the summer of 2007 within the northern hemisphere tropical latitudinal band.

3.1. Figure 3.2(b) shows the PDF of all the residual values that lie within a 2 km thick layer below the local tropopause, namely within Region D (refer to Figure 3.2(a)), for scans residing in the northern hemisphere tropical latitudinal band.

The tangent altitude regions of interest in Figure 3.2(a), which are defined by the local tropopause of the scan, were defined to be 1 km thick and a residual probability density function was made for each region. These probability density functions form a two dimensional probability density surface shown in Figure 3.3. Therefore, the left maximum range represents the cloud-free condition and the smaller right maximum range represents the cloudy condition.

3.2 Cloud-Free Threshold as a Function of Altitude

The probability density function in Figure 3.3 was created from residual profiles, which feature scattering enhancements. Two distributions are observed in the PDF; the left and right distributions represent the cloud-free and cloudy conditions, respectively. Statistically, integrating a PDF between

Table 3.1: Definitions of latitude ranges

Region Name	Latitude Range
Northern Hemisphere, High Latitudes	$55 \leq \theta \leq 90$
Northern Hemisphere, Middle Latitudes	$25 \leq \theta < 55$
Northern Hemisphere, Tropical Latitudes	$0 \leq \theta < 25$
Southern Hemisphere, Tropical Latitudes	$-25 \leq \theta < 0$
Southern Hemisphere, Middle Latitudes	$-55 \leq \theta < -25$
Southern Hemisphere, High Latitudes	$-90 \leq \theta < -55$

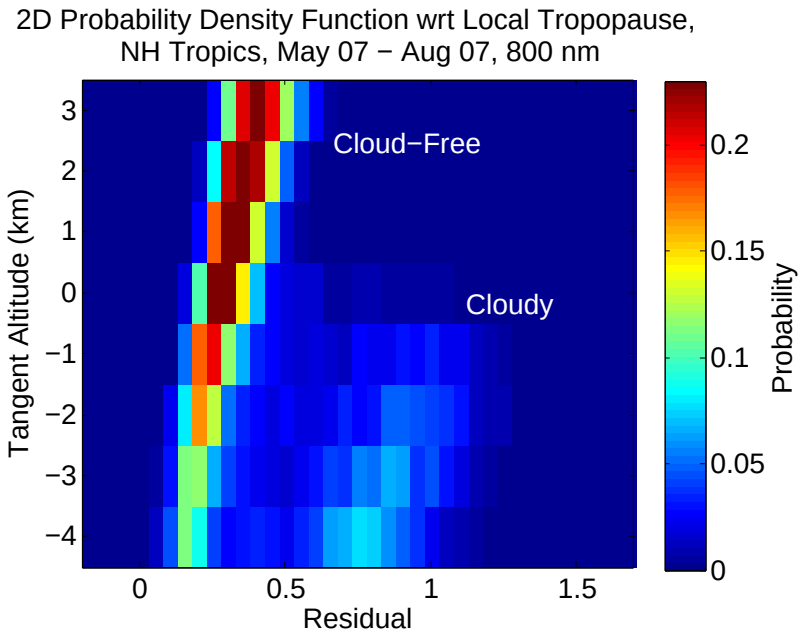

Figure 3.3: Two-dimensional residual probability density function for scans within the northern hemisphere tropical latitudinal band from May to August 2007 at 800 nm. The vertical axis is shown with respect to the local tropopause; negative values correspond to altitudes below the tropopause level.

two limits yields the probability of occurrence of such event within the range of interest. Thus, the object here is to separate the cloudy and cloud-free conditions by defining a threshold value that lies between the two distributions. Integrating from the threshold position over the cloudy distribution yields the probability of cloud occurrence.

To obtain the probability of locating a cloud within the defined tangent altitude region and latitudinal band, the PDF is integrated from a threshold position between the cloud-free and cloudy peaks over the cloudy condition. This cloud-free threshold determines the occurrence of a cloud. From statistics, the probability of a cloud occurrence, P[cloud occurrence], is

$$P[\text{cloud occurrence}] = \int_{\text{threshold}}^{\infty} pdf(R)\mathrm{d}R, \tag{3.3}$$

where R is the scattering residual. For the PDF shown in Figure 3.2(b), the threshold is approximately 0.6. However, as shown in Figure 3.3, the distributions corresponding to the cloud-free and cloudy conditions gradually shift to slightly higher residual values as altitude increases due to increasing stratospheric aerosol concentration with altitude. Thus, the threshold distinguishing the two conditions is not a single value; rather it is a curved line as a function of altitude, which separates the cloud-free and cloudy maxima.

Although they maintain the same general shape, the maxima cloud-free and cloudy distributions are unique for each latitudinal band. Therefore, each two dimensional probability density surface requires a unique cloud-free threshold curve. A technique was developed to determine the threshold based on the PDFs. For each altitude region of interest, the maximum of the cloud-free peak was found and the distance from zero along the residual axis, δ_i, was noted, where i denotes the i-th altitude region of interest. The PDF was then normalized by the maximum value of the cloud-free peak and shifted as to align the maximum with zero. This process is shown in Figure 3.4.

Once the PDFs from each altitude region of interest were shifted so the maxima of the cloud-free peaks were aligned at zero, an average was taken to obtain an averaged PDF. Recall that the PDFs for each altitude region of interest were normalized by the maximum value of the cloud-free peak, so the averaged PDF also had a maximum cloud-free peak of 1 centered at zero. The normalized, shifted PDFs for each altitude region of interest and the averaged PDF are shown in Figure 3.5.

The average cloud-free peak can be closely modelled as a Gaussian distribution. The left hand side of the averaged cloud-free maximum peak was mirrored to obtain a Gaussian-type mirrored shape. Note that the right hand side was neglected as it likely contained traces from the tail end of the cloudy distribution. The mirrored shape was then fitted with a Gaussian. This was accomplished

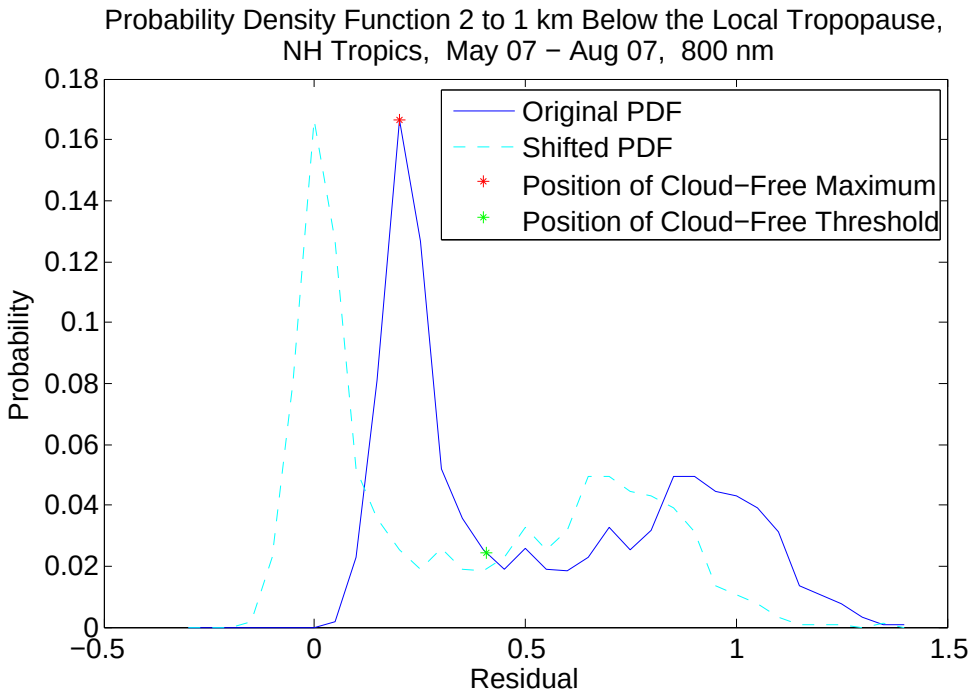

Figure 3.4: Probability density function for scans within 2 to 1 km below the tropopause within the northern hemisphere tropical latitudinal band from May to August 2007 at 800 nm.

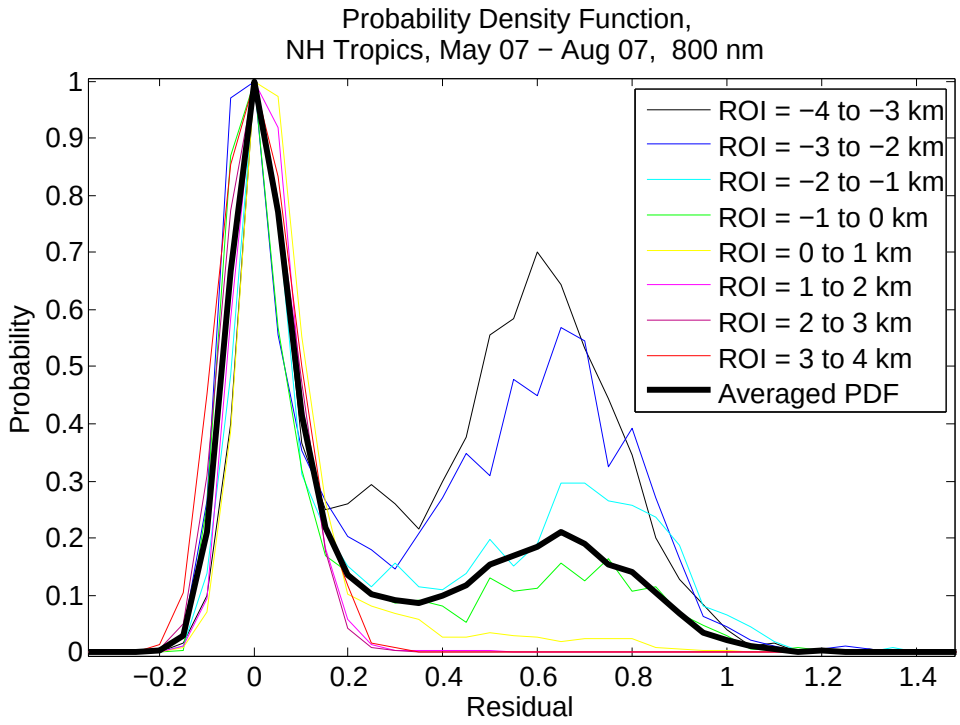

Figure 3.5: Normalized and shifted probability density functions for various altitude regions of interest and averaged probability density function for scans within the northern hemisphere tropical latitudinal band from May to August 2007 at 800 nm.

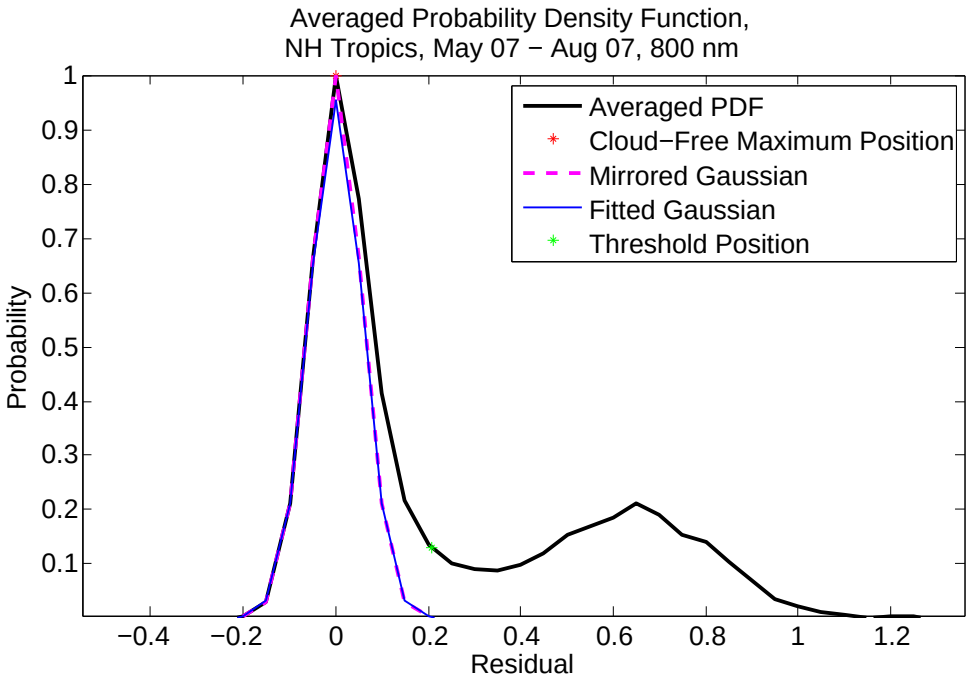

Figure 3.6: Averaged probability density functions and mirrored Gaussian for scans within the northern hemisphere tropical latitudinal band from May to August 2007 at 800 nm.

by fitting a parabola to the natural logarithm of the mirrored shape using a least squares polynomial curve fitting technique. The fitted Gaussian was obtained by taking the exponential of the resulting curve from the polynomial fitting. Figure 3.6 shows the average PDF, the mirrored shape of the left hand side of the cloud-free peak, and the fitted Gaussian.

The variance of the fitted Gaussian, σ^2, was computed such that,

$$\sigma = \frac{|x_o - \mu|}{\sqrt{2 \ln 2}}, \tag{3.4}$$

where x_o and μ are the half-width half-maximum position and the mean of the fitted Gaussian, respectively. The position 2σ was found to be a reliable demarkation of the threshold position between the cloud-free and cloudy conditions. As latitude increases, the distinction between the cloud-free and cloudy distributions becomes blurred especially near lower tangent altitudes. To determine the cloud-free threshold curve as a function of altitude, the 2σ position to the right of the cloud-free peak maximum was determined on the PDFs for each altitude region of interest. That is, the PDFs from each altitude region of interest from Figure 3.5 were unshifted by δ_i, the distance the original PDF was shifted to zero along the residual axis, and the position 2σ to the right of the maximum of the cloud-free peak was marked as the threshold point. Figure 3.7 shows the cloud-free threshold curve as a function of altitude overtop the probability density surface for scans in the

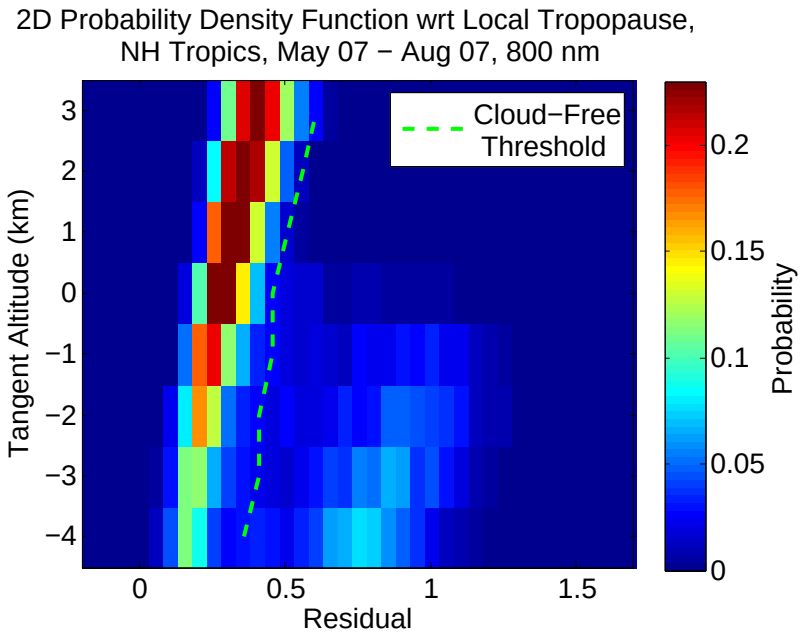

Figure 3.7: Two-dimensional residual probability density function with the cloud-free threshold curve for scans within the northern hemisphere tropical latitudinal band from May to August 2007 at 800 nm. The vertical axis is shown with respect to the local tropopause; negative values correspond to altitudes below the tropopause level.

northern hemisphere tropical latitudinal band from May to August 2007 at 800 nm. The difference between the PDF distribution and the Gaussian fitted shape is the cloudy distribution. All negative points in the difference to the left of the threshold point, which arise from a non-perfect Gaussian fitting, were set to zero and the remaining distribution represents the cloudy condition.

3.3 Change in Solar Scattering Angle with Time

The solar scattering angle, Θ, which is the angle between the satellite's line of sight and the solar direction, varies over the course of a year due to orbital configurations. Figure 3.8 shows the monthly average solar scattering angle from June 2006 to June 2007. One would expect the solar scattering angle to follow an approximate cosinusoidal pattern covering a full period over a year, and generally this is the case. However, during the months of October and November 2006, Odin was tilted off the orbital plane as to acquire data poleward of 82°S; that is beyond the latitude range typically sampled for on-track instrument pointing. As the solar scattering angle changes with time, the amplitude of the radiance signal measured by OSIRIS also varies proportionally with time and causes the cloud-free and cloudy distributions on the PDFs to shift along the residual axis.

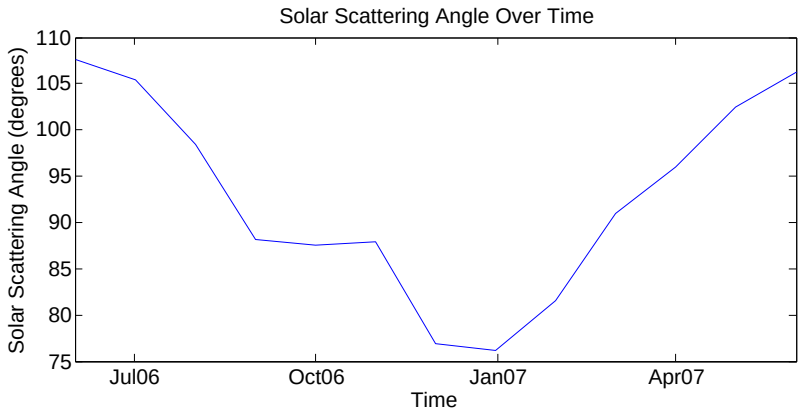

Figure 3.8: Solar scattering angle as a function of time from June 2006 to June 2007.

Referring to Figure 2.9, the phase functions for Mie and cloud particle scattering are predominantly forward scattering and the measured radiance signal is correspondingly amplified as the scattering angle decreases.

When data spanning a large time period are used to form a single PDF, the distributions are blurred as if there are several time-dependent PDFs overlayed on top of each other. Because the amplitude of the measured signal changes over time due to changing solar scattering angles, it is necessary to separate the data into time-dependent sections as to produce PDFs with little blurring. In this work, data were separated into monthly bins. That is, a two-dimensional PDF, such as that shown in Figure 3.3, was made and a unique threshold line was computed for each latitude range and for each month considered.

3.4 Cloud-Top Correction and Probability Maps

In this section, a correction was made to account for a counting bias and probability maps were produced, which show the cloud top occurrence frequency distribution.

The OSIRIS scans were organized on a monthly basis into bins according to their latitude and longitude coordinates where the latitudinal and longitudinal bins were 7.5 and 20 degrees wide, respectively. A probability density surface of scattering residuals was created from radiance profiles measured in the northern hemisphere during boreal summer. A cloud-free threshold curve was determined for each month and latitude band as described in Section 3.2. By integrating from this line over the cloudy maximum range, the probability of locating a cloud for a given altitude range within a latitude-longitude bin on a monthly basis was determined.

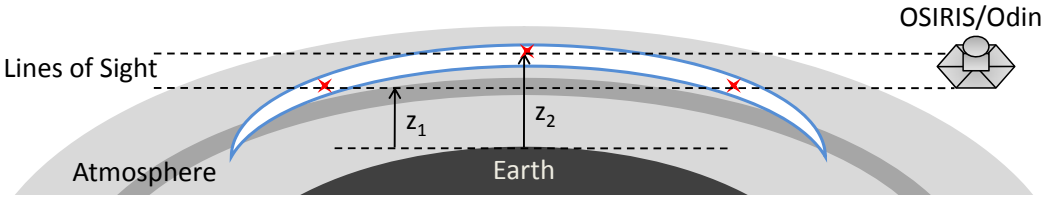

(a) Cloud top measurement

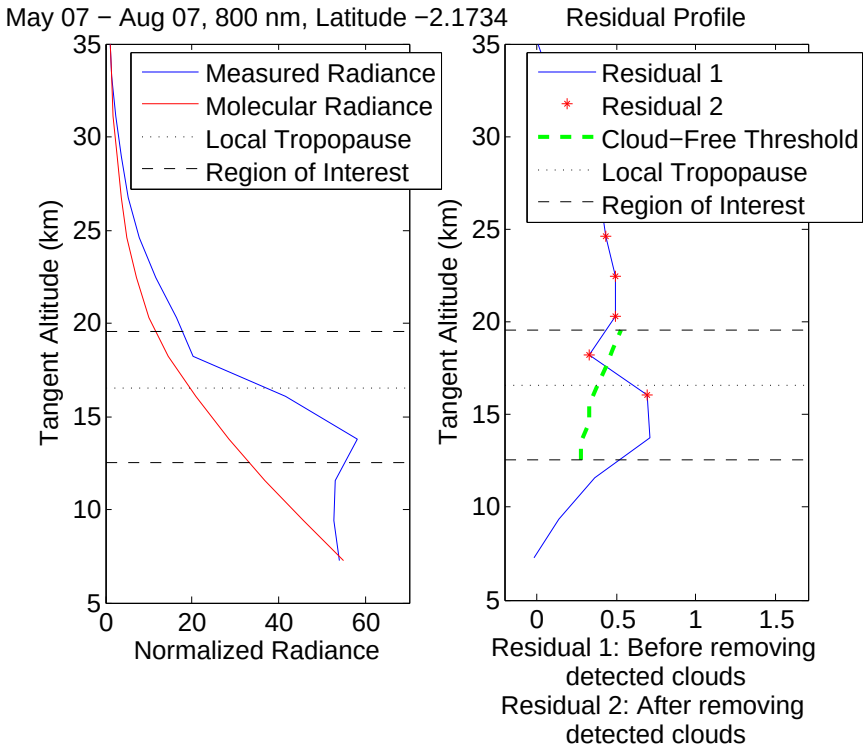

(b) Cloud top correction

Figure 3.9: (a) Multiple measurements of the same thin cloud layer and (b) correction to detecting clouds multiple times.

As neither the vertical thickness nor the horizontal extent of the clouds were taken into account, these probabilities are biased. In the schematic drawing in Figure 3.9(a), the red stars indicate where the limb viewing satellite detects the shown cloud. At tangent altitude z_1, the cloud is detected once, and at tangent altitude z_2, the same cloud is detected a second time. In order to avoid a counting bias, clouds should only be detected once at the highest detected tangent altitude.

As discussed above, the cloud-free threshold curve is a function of altitude; the dashed green line in Figure 3.7 separates the cloud-free and cloudy conditions. This threshold curve is also overlayed on the residual profile plot in Figure 3.9(b). In Figure 3.9(b), clouds are detected at 16.1 and 13.8 km tangent altitude since the residual values exceed the green cloud-free threshold curve at

these altitudes. Due to the discrete nature of the measurement, it cannot be determined if the satellite detected a single cloud several times or multiple clouds.

To correct this bias, each scan was checked for residual values that fell in the tangent altitude region of interest beyond the cloud-free threshold curve. The first and highest occurrence was noted and all other residual values below this altitude were disregarded. Therefore, rather than simply detecting the presence of a cloud at a given altitude, the results show the detection of cloud tops; that is the highest measurement that shows the presence of cloud.

These corrected probabilities are shown in Figure 3.10 for OSIRIS northern hemisphere measurements during boreal summer of 2007. The resolution in this figure is somewhat coarse due to noise and low sampling; over four months of data and depending on the altitude layer, each latitude-longitude bin contains on average between 16 and 23 samples. As observed, there are high probabilities of detecting cloud tops at and just below the tropopause around the Asian monsoon and Central America, both regions of intense convection. Furthermore, there are non-zero detection frequencies above the tropopause, particularly above Indonesia and Asia. This is an important observation considering the influence clouds have on the water vapour distribution in the lower stratosphere, which will be discussed further in Chapter 4.

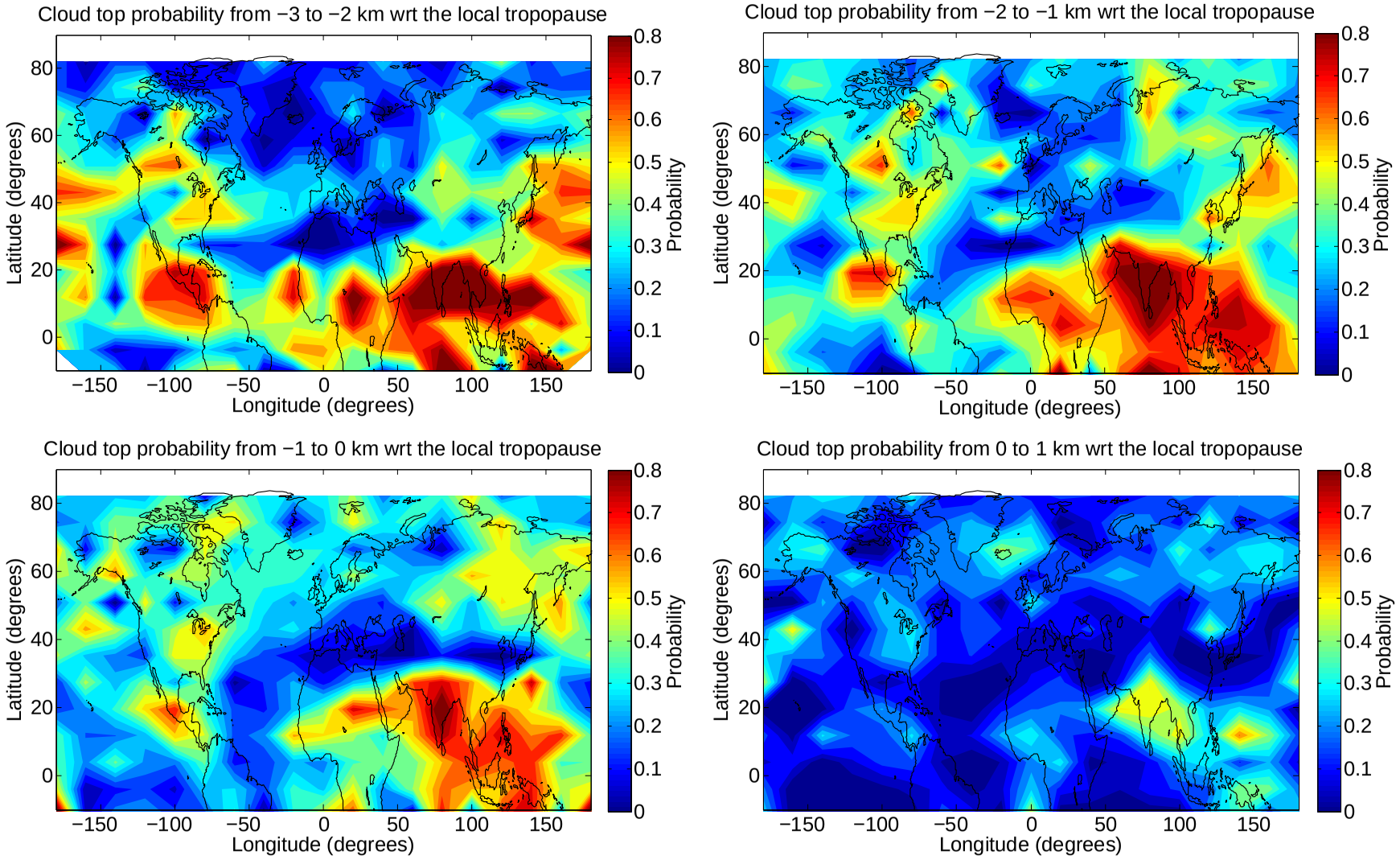

Figure 3.10: Probability of locating cloud tops during May, June, July, and August 2007 derived from OSIRIS measurements at 800 nm.

3.5 Comparison to CALIPSO

Thus far, the details entailed in the cloud detection technique have been presented and some preliminary results have been shown. In an effort to validate and test the technique, results using OSIRIS data are compared to those obtained by *Sassen et al.* (2008) who utilized CALIPSO measurements.

CALIPSO is a joint satellite mission between the National Aeronautics and Space Administration (NASA) Langley Research Center and the French Space Agency, Centre national d'études spatiales, to investigate the impact clouds and aerosols have on the radiative balance of the atmosphere. CALIPSO was launched April 2006 into a circular sun-synchronous polar orbit at about 705 km altitude. Like Odin, CALIPSO has an orbital inclination of 98° from the equator which provides global coverage from 82°S to 82°N. The satellite retraces its track to within ±10 km every 16 days. CALIPSO flies with five other satellites in the international A-train constellation for synchronic measurements of the Earth. The satellites fly sequentially with an on-track separation of two minutes (*Winker et al.*, 2004, 2007).

There are three nadir-viewing instruments onboard CALIPSO: the Cloud-Aerosol Lidar with Orthogonal Polarization (CALIOP), the Imaging Infrared Radiometer, and the Wide Field Camera. Only CALIOP is used in this work. CALIOP is a polarization-sensitive lidar and takes measurements at 0130 h and 1330 h local time of the total attenuated backscatter at 532 and 1064 nm. The lidar profiles contain information on the vertical distribution of clouds and aerosols, the ice/water phase composition of the clouds through the ratio of the signals from two orthogonal polarization channels, and the size distribution of aerosol particles through the wavelength dependence of the backscatter signal (*Winker and Pelon*, 2003).

Sassen et al. (2008) study the global distribution of cirrus clouds from CALIPSO measurements from 15 June 2006 to 15 June 2007. A cirrus cloud identification algorithm was developed to assure only cirrus clouds detected by CALIPSO were used in the analysis and that high altitude non-cirrus ice clouds, such as altostratus and cumulonimbus clouds, were excluded. Cirrus classifications are typically based on radar reflectivity, visible optical depth, cloud height, and temperature (*Sassen et al.*, 2008). Based on empirical results, the visible optical depth of cirrus clouds does not exceed $\tau \approx 3.0$ (*Sassen and Cho*, 1992). Because lidar probing is restricted to $\tau <\sim 3.0 - 4.0$ before the signal is completely attenuated by passing through the cloud layer twice, the lowest detected cloud layer that completely attenuates the signal does not meet the cirrus cloud classification.

With the classifications described above, the presence of cloud and ice layers near the polar

regions, namely PSCs and ice clouds occurring at unusually low altitudes, remain evident. To void such detections, *Sassen et al.* (2008) applied additional constraints on the dataset. Cloud top heights were restricted to < 1.5 km above the local tropopause and the lowest allowable cloud top height was restricted to 4.0 km. Furthermore, because the tropopause height over the South Pole is uncertain during the winter season, an upper cloud top limit of 12.0 km was imposed in this region. Lastly, in order to distinguish cloud layers, clouds must be separated by a minimum of 1.0 km in height.

Figure 3.11(a) shows the global distribution of the average cirrus cloud occurrence frequency as detected by the CALIPSO identification algorithm by *Sassen et al.* (2008) in terms of 5.0° longitude and 5.0° latitude grid boxes. Figure 3.12(a) displays the equivalent distribution as altitude versus latitude in 0.2 km height intervals and 2.5° latitude bins. For comparison, the analogous average cloud top occurrence frequency of clouds detected by OSIRIS using the cloud detection technique described in Sections 3.1 through 3.4 are shown in Figures 3.11(b) and 3.12(b), respectively, with 20° longitude and 7.5° latitude grid boxes and 2 km height intervals. The comparisons reveal good agreement especially considering the different viewing geometries of the instruments.

Equatorial warm air is driven upward due to convective motions and, upon entering the stratosphere, it is dried and forms a poleward pressure gradient force at high altitude near the tropopause. As this air flows poleward from the equator, it is cooled, which causes it to descend at $\sim$30° latitude. This downwelling of dry air forms deserts over continental regions and suppresses the formation of cirrus clouds at high altitudes, which is visible in Figures 3.11 and 3.12. A reverse pressure gradient force at the surface drives the air equatorward. This thermally driven circulation is called the *Hadley Cell* (*Liou*, 2002). Air flowing toward the equator is deflected to the west due to the Coriolis force and the rotation of the Earth creating easterly trade winds. The region where air masses emanating from the southern and northern hemispheres join is called the *Intertropical Convergence Zone* (ITCZ) and is typically characterized by heavy weather and thunderstorms. As *Waliser and Gautier* (1993) explain, "this permanent low pressure feature marks the meteorological equator where the trade winds, laden with heat and moisture from surface evaporation and sensible heating, converge to form a zone of increased mean convection, cloudiness, and precipitation."

The areas where there is maximum cirrus cloud coverage occur predominantly in the tropical belt at relatively high altitudes. In Figure 3.11, the cirrus cloud occurrence frequency is slightly higher than 60% over Indonesia and the western part of the Pacific Ocean, and smaller maxima with $\sim$55% occurrence frequency occur over Central and South America and western-central Africa.

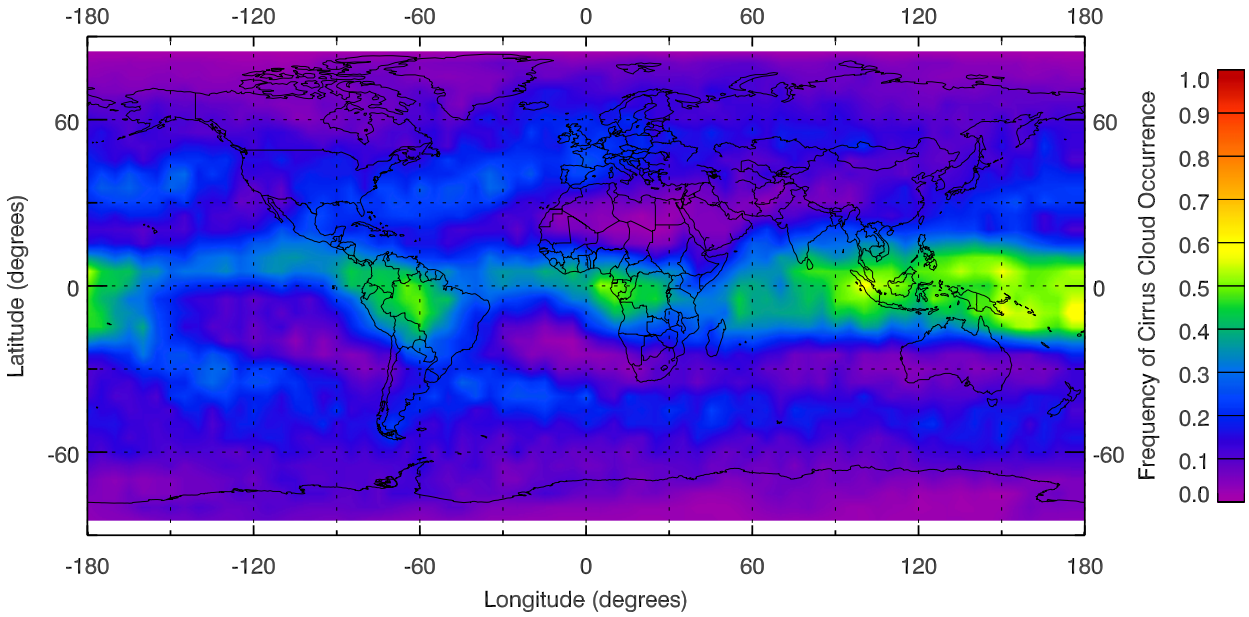

(a) Average cloud top occurrence by CALIPSO

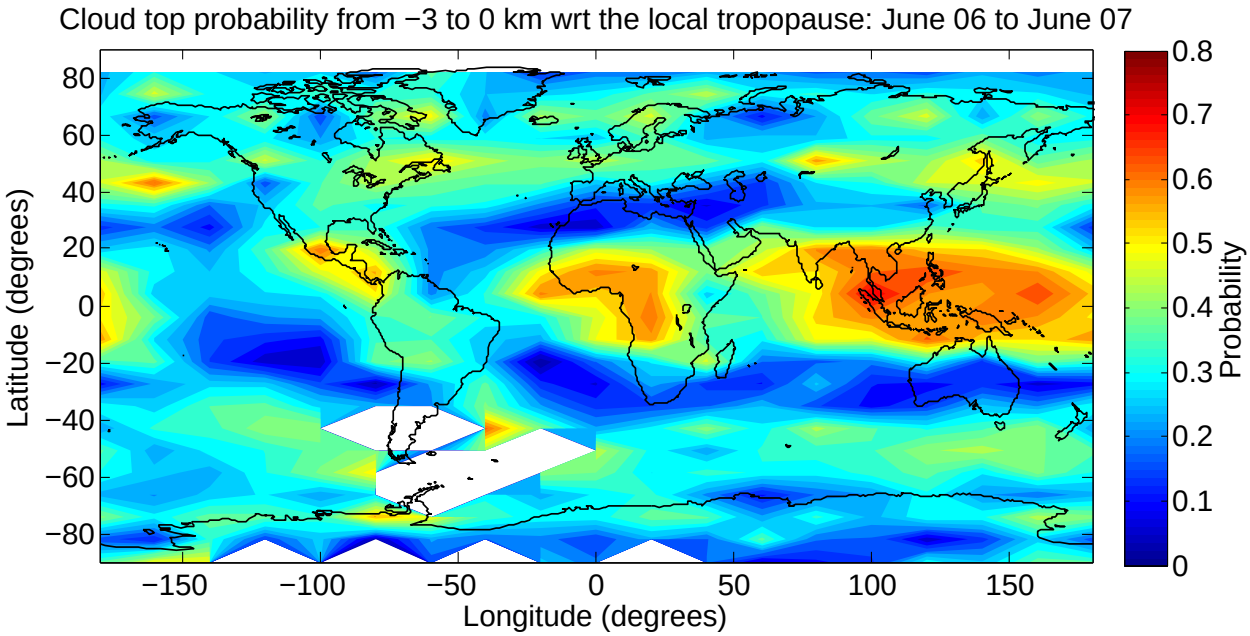

(b) Average cloud top occurrence by OSIRIS

Figure 3.11: (a) Global distribution of the average cirrus cloud occurrence frequency identified by CALIPSO algorithm between 15 June 2006 and 15 June 2007; extracted from *Sassen et al.* (2008) and reproduced by permission of American Geophysical Union. (b) Average cloud top occurrence frequency of clouds detected by OSIRIS algorithm in a three-kilometer thick layer below the local tropopause between June 2006 and June 2007.

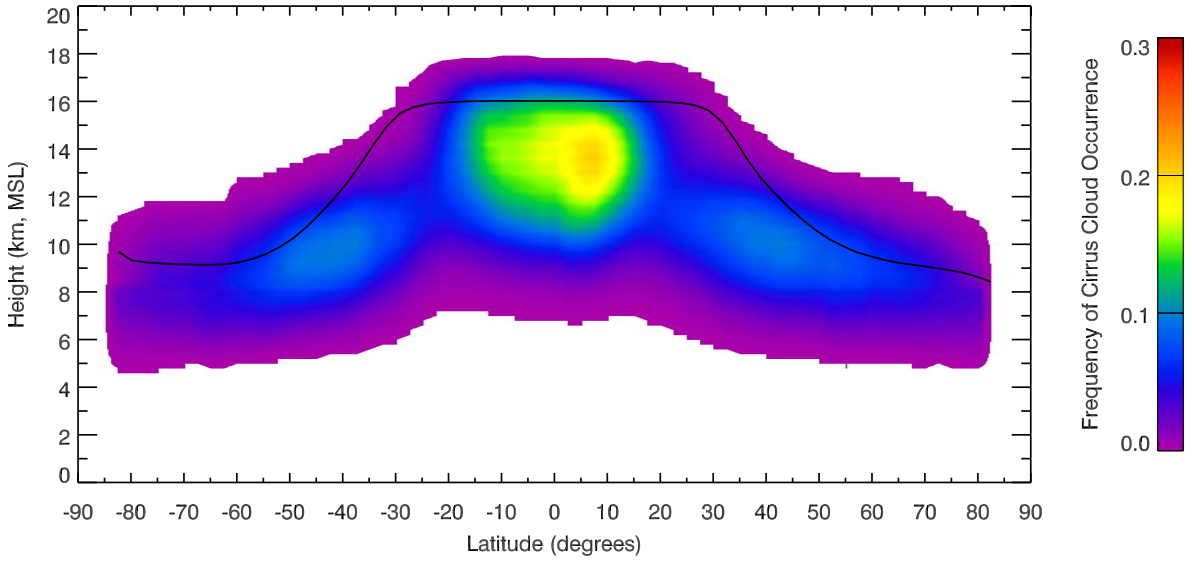

(a) Zonal average cloud top occurrence by CALIPSO

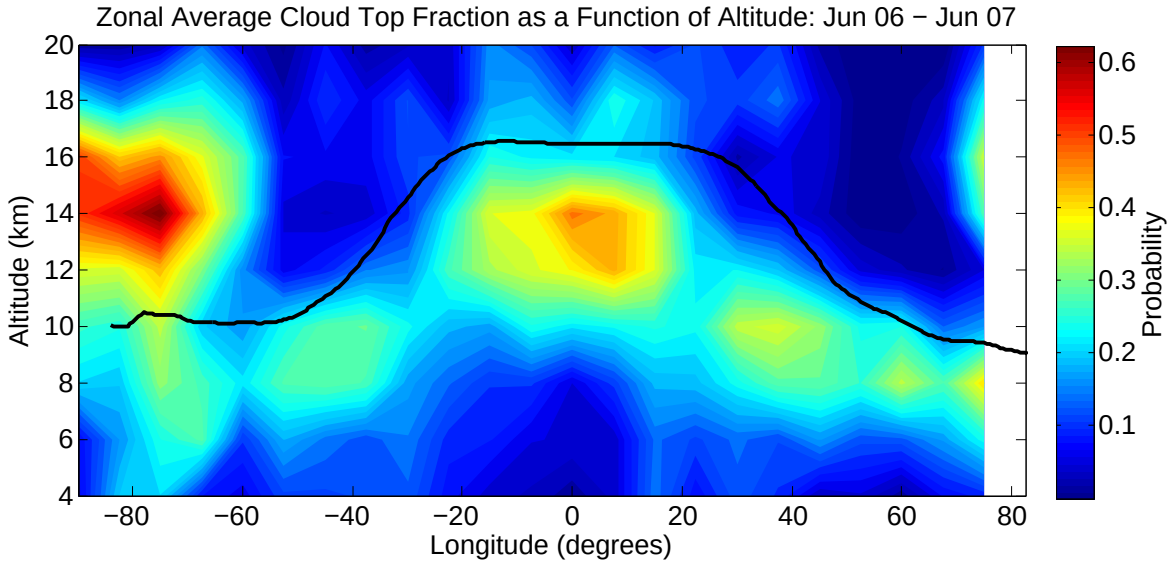

(b) Zonal average cloud top occurrence by OSIRIS

Figure 3.12: (a) Latitudinal distribution of the average cirrus cloud occurrence frequency identified by CALIPSO algorithm between 15 June 2006 and 15 June 2007; extracted from *Sassen et al.* (2008) and reproduced by permission of American Geophysical Union. (b) Zonal average cloud top occurrence frequency of clouds detected by OSIRIS algorithm between June 2006 and June 2007.

These are known regions of intense convective activity: the monsoons in Indonesia, the south-east Asian rainforest, the rainforests in Central America and in the Amazon region, and the Congo Basin rainforest in Africa (*Wang et al.*, 1996; *Dessler and Sherwood*, 2004; *Fu et al.*, 2007; *Sassen et al.*, 2009). From Figure 3.12, the latitudinal distribution shows maximum cirrus cloud occurrence within the tropical belt between $\pm 15^\circ$ latitude at 14 km altitude, which is coincident with the mean location of the ITCZ and the level of maximum convective outflow. There is also about 23% cloud occurrence in the lower stratosphere within the tropics. These ultra thin stratospheric clouds are observed by OSIRIS but are not detected by CALIPSO likely due to differing instrument sensitivities and viewing geometries. Cirrus cloud occurrence generally decreases as the poles are approached except at the South Pole where the presence of PSCs is remarkably strong. PSCs occur well within the stratosphere near 14 km at high southern latitudes and were removed from the CALIPSO detections.

Figure 3.13 was extracted from *Sassen et al.* (2008) and, using the same data set from 15 June 2006 and 15 June 2007, the average global seasonal cirrus cloud coverage as detected by the CALIPSO identification algorithm are shown and are labelled with respect to the northern hemisphere seasons. Correspondingly, Figure 3.14 shows the average seasonal cloud top occurrence frequency as identified by the cloud detection technique using OSIRIS measurements taken during the same seasons for the years 2006, 2007, and 2008. The corresponding number of samples available in the cloud top detection analysis is shown in Figure 3.15 for 7.5° latitude and 20° longitude grid boxes.

Interestingly, the south-north displacement of the ITCZ is evident through the seasonal distributions in Figures 3.13 and 3.14. The convective maxima forming a belt near the equator are shifted latitudinally toward the summer hemisphere in concert with the seasonal changes. The probability of cloud occurrence is around 70% over India during the northern hemisphere summer when monsoon activity is most dynamic.

Figure 3.15 shows the number of samples used in the seasonal cloud top occurrence frequency analysis of Figure 3.14. Areas with fewer than 10 samples are not included in the analysis. A careful look at the sampling maps show there are generally fewer scans taken between -40° and 0° longitude. OSIRIS is routinely turned off for a scheduled rest period and is only turned on once the orbit carries the satellite over Sweden. As a result, there are fewer scans taken in the -40° to 0° longitudinal band. Prior to June 2007, OSIRIS was powered off every other day. Odin is a shared satellite so half of its time was devoted to astronomical research. Since June 2007, the astronomical

instrument onboard Odin is not in operation, so OSIRIS is now turned off every Thursday for a rest period of one day.

Also shown in Figure 3.15, there is an obvious decrease in the number of samples between -100° and -10° longitude and -70° to -10° latitude, which is due to the South Atlantic Anomaly (SAA). The SAA occurs along the magnetic equator where the geomagnetic field of the Earth is weakest and coincides with the region where the Van Allen radiation belt is closest to the Earth. A flux increase in highly energetic solar particles that are trapped within the magnetic field of the Earth causes radiation damage to satellites passing through the area (*Heirtzler*, 2002). Of course, the SAA is typically observed about 22° to the north of this region shown in Figure 3.15. While OSIRIS observes the limb of the atmosphere, the coordinates of the measurement are recorded at the tangent point, which is roughly latitudinally 22° away from the position of the satellite. Thus, when Odin passes through the SAA region and is exposed to intense radiation, these measurements, which are recorded at the coordinates of the tangent point, are affected and are often discarded.

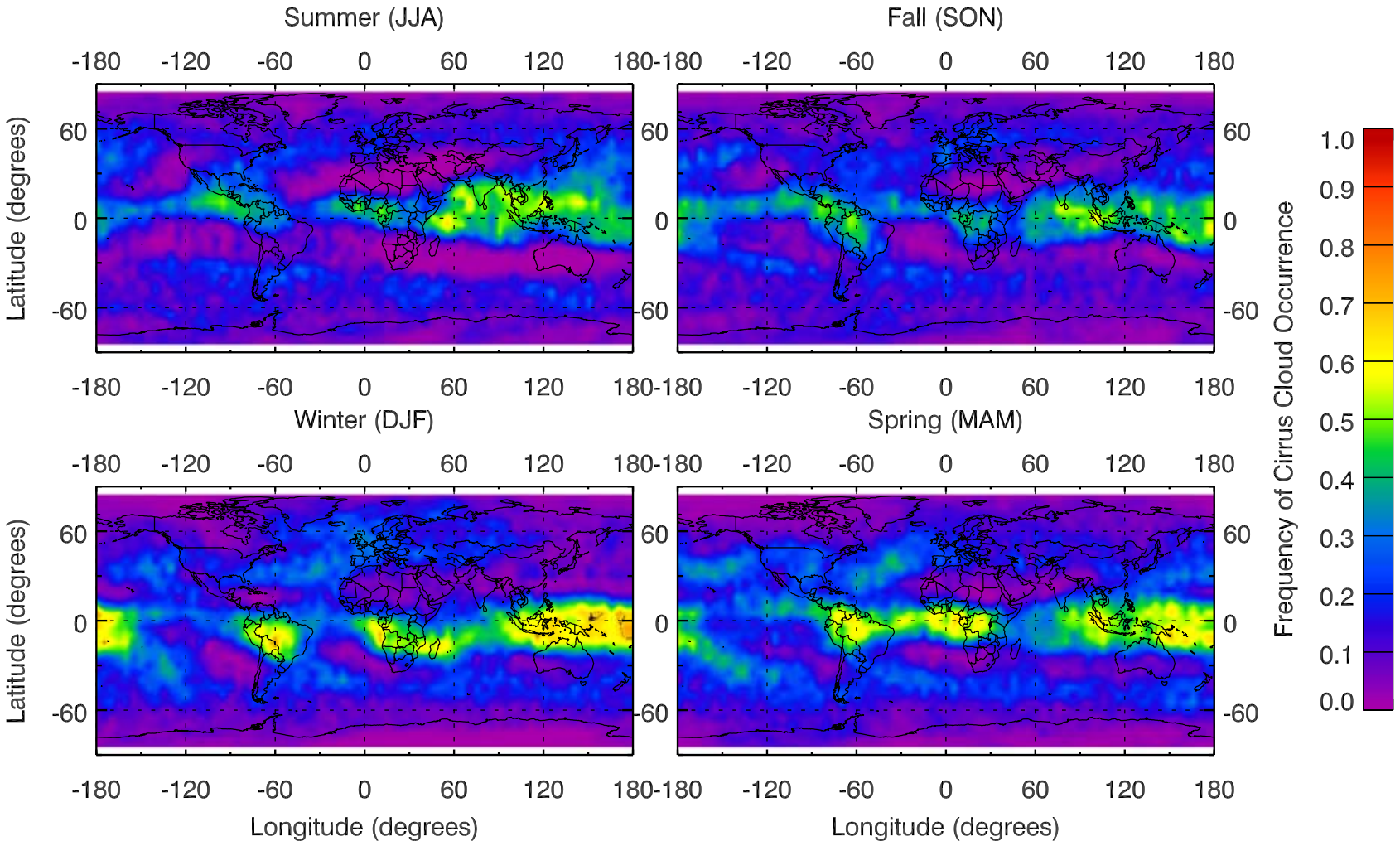

Figure 3.13: Global seasonal distribution of the average cirrus cloud occurrence frequency identified by CALIPSO algorithm from 15 June 2006 and 15 June 2007; extracted from *Sassen et al.* (2008) and reproduced by permission of American Geophysical Union.

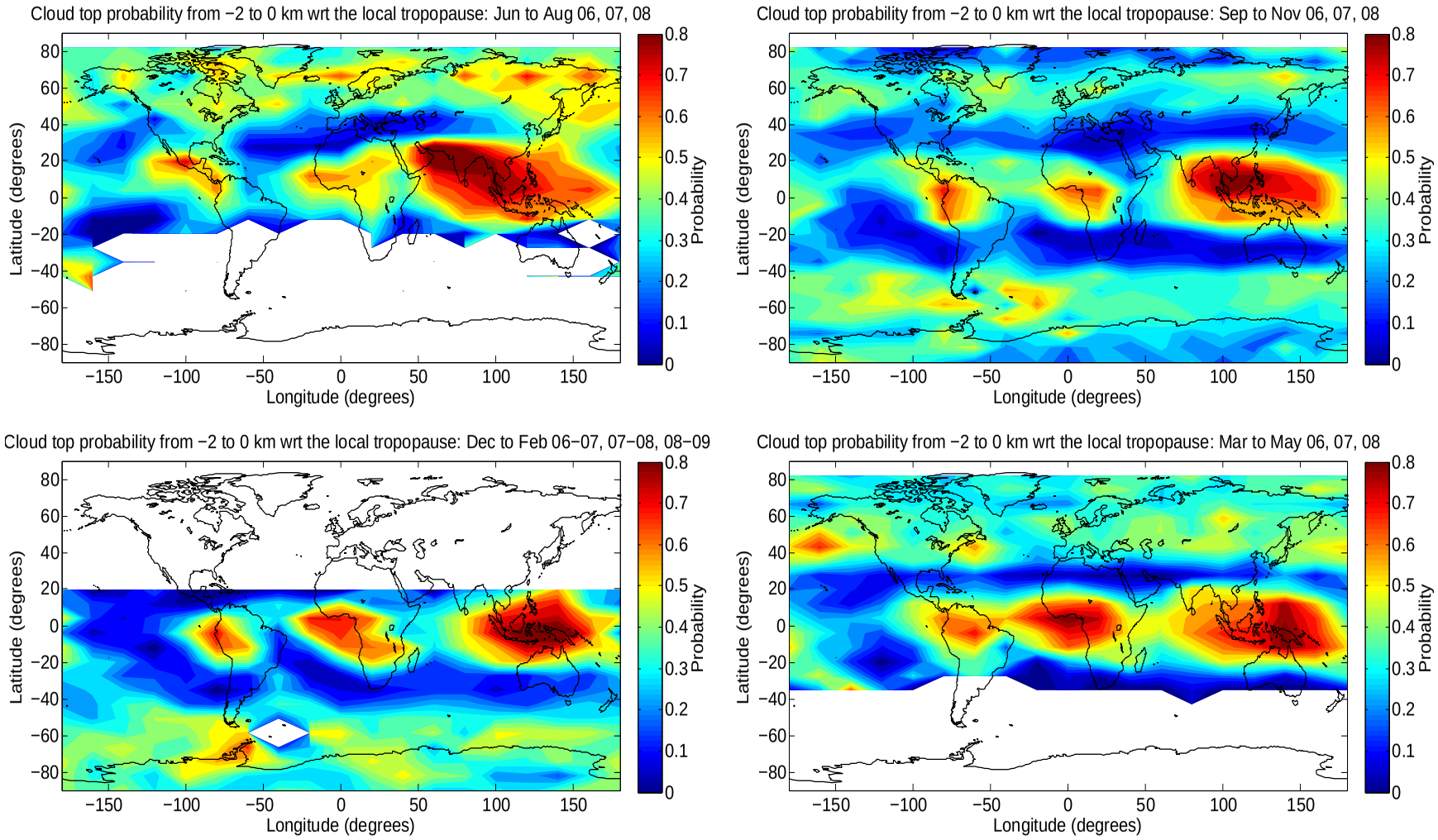

Figure 3.14: Seasonal cloud top occurrence frequency of clouds detected by OSIRIS algorithm in a two-kilometer thick layer below the local tropopause averaged between the years 2006, 2007, and 2008.

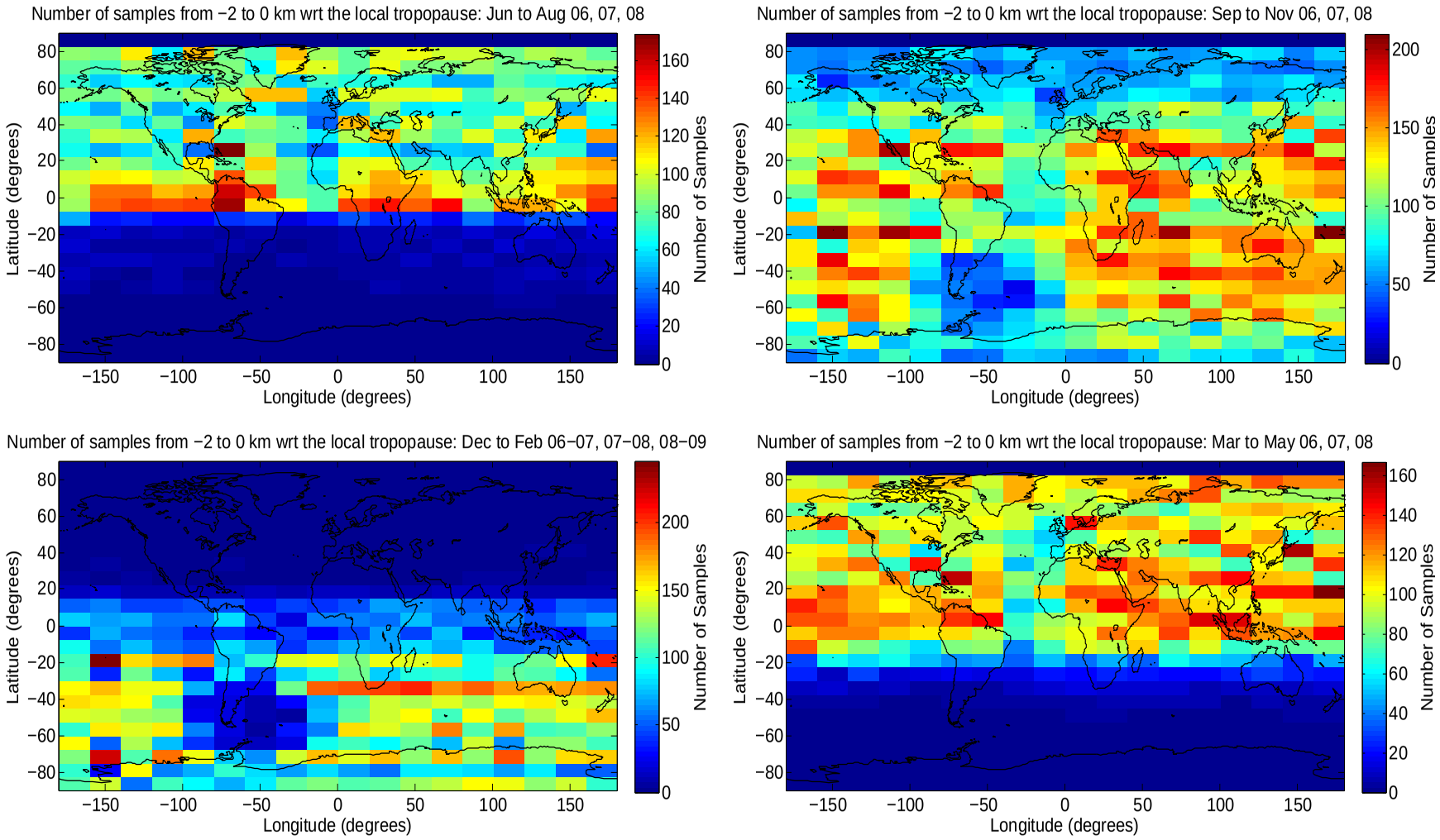

Figure 3.15: Number of samples available for determining the cloud top occurrence frequency of clouds detected by OSIRIS algorithm in a two-kilometer thick layer below the local tropopause between the years 2006, 2007, and 2008.

3.6 Comparison to SAGE II

The cloud detection technique with OSIRIS limb scattering measurements is further compared to those obtained by *Wang et al.* (1996) who used SAGE II occultation measurements as the viewing geometries of these two instruments are similar.

The SAGE II instrument was aboard the Earth Radiation Budget Satellite and its mission was to measure the vertical profiles of ozone, nitrogen dioxide, water vapour, and the aerosol extinction coefficient. The satellite flew in a sun-synchronous orbit with a 90 minute period and a 57° inclination to allow a latitudinal coverage of approximately 135° per month. The latitude extremes varied seasonally, however there was no sampling poleward of 55° during boreal and austral winters (*Wang et al.*, 1996).

SAGE II was a seven-channel radiometer with channels centered at 0.385, 0.448, 0.453, 0.525, 0.600, 0.940, and 1.02 μm. The instrument used the solar occultation technique capturing one sunset and one sunrise measurement per orbit. In one day, 15 sunrise events were measured; these were approximately equally separated in longitude and exhibited a slight shift in latitude between consecutive measurements. The instrument's field of view was 0.5 km vertically and 2.5 km horizontally at the tangent point. SAGE II was in operation from October 1984 to August 2005 (*Wang et al.*, 1996).

Wang et al. (1996) assembled a climatology of cloud occurrence frequency based on six years of SAGE II observations between 1985 and 1990. Subvisual and opaque clouds were distinguished by the measurement upper limit extinction coefficient for aerosols, which for 1.02 μm is roughly $2 \times 10^{-4}\,\mathrm{km}^{-1}$. Using the cirrus cloud classification from *Sassen and Cho* (1992), clouds with extinction coefficients larger than the measurement limit were marked as opaque clouds because the transmitted signal fell beyond the instrument's sensitivity and the cloud profile was restricted to that altitude (*Wang et al.*, 1996). Furthermore, clouds were distinguished from aerosols through the ratio for the extinction coefficients at two wavelengths, namely at 0.52 and 1.02 μm. Such a ratio contains information on the particle size.

Shown in Figure 3.16(a), *Fueglistaler et al.* (2009) compare the mean cirrus cloud occurrence frequencies for opaque and cirrus clouds derived from CALIPSO and SAGE II instruments. The left-hand plot incorporates CALIPSO cloud occurrence frequency profiles from 20°S to 20°N for optical thicknesses $\tau < 0.1$ (thin line), $\tau > 0.5$ (thick line), and all (dashed line) and is adapted from *Fu et al.* (2007). The right-hand plot uses SAGE II profiles from 10°S to 10°N for optically

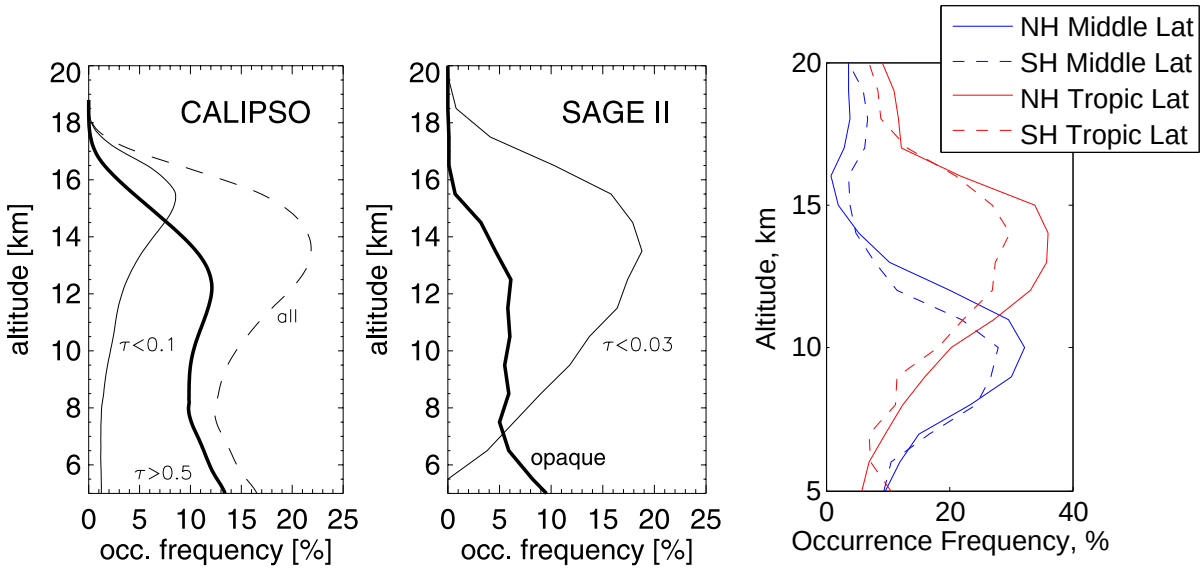

(a) Mean cloud occurrence frequency by CALIPSO and SAGE II

(b) Mean cloud occurrence frequency by OSIRIS

Figure 3.16: (a) Mean cloud occurrence frequency versus altitude for data from June 2006 to February 2007 as measured by (left) CALIPSO using profiles from 20°S to 20°N, adapted from *Fu et al.* (2007), and (right) SAGE II with profiles from 10°S to 10°N, updated from *Wang et al.* (1996); extracted from *Fueglistaler et al.* (2009) and reproduced by permission of American Geophysical Union. (b) Mean cloud occurrence frequency versus altitude as measured by OSIRIS from June 2006 to June 2007. The latitudinal bands are defined in Table 3.1.

thick (thick line) and subvisual cirrus (thin line) and is updated from *Wang et al.* (1996). Although both instruments demonstrate thinner cirrus clouds occur within the TTL and opaque clouds occur at lower altitudes, the curves illustrating the occurrence frequencies do not agree well. The $\tau < 0.03$ thin line from the right-hand SAGE II plot should be contained within the $\tau < 0.1$ thin line from the left-hand CALIPSO plot. According to *Fueglistaler et al.* (2009), the differences between the CALIPSO and SAGE II occurrence frequencies are partly due to the dissimilar viewing geometries of the instruments and to the different optical depth thresholds. SAGE II is very sensitive to thin clouds. Figure 3.16(b) demonstrates the cloud top occurrence frequency from OSIRIS measurements between June 2006 and June 2007. Upon visual inspection, the shapes of the tropical latitudinal curves agree nicely with the SAGE II thin cirrus curve. This result is encouraging especially because the two instruments have similar viewing geometries. OSIRIS detected roughly 10% more cirrus clouds than SAGE II possibly because of a higher limb viewing sensitivity. This result leads to a confirmation of the theory presented in *Fueglistaler et al.* (2009).

Figure 3.17(a) shows the global distribution of cirrus cloud occurrence frequency between 1985 to 1990 as measured by SAGE II at three altitude slices: 12.5, 14.5, and 16.5 km. This figure can be compared to Figure 3.11. Note, however, that the data used in these figure do not cover the same time period, so differences are to be expected. The comparison between figures must be carried out with care as the figures using CALIPSO and SAGE II data are produced on an absolute altitude scale while the OSIRIS analysis utilizes an altitude scale relative to the local tropopause. The OSIRIS analysis is carried out in this way to compensate how the tropopause height falls in altitude as the poles are approached, as shown in Figure 2.3. In order to make a direct comparison, Figure 3.18 shows the global distribution of cirrus cloud top occurrence frequency as measured by OSIRIS at discrete altitude layers; that is the plots were generated using an absolute altitude scale rather than a relative scale to the local tropopause altitude. Similarly, the six-year average zonal mean occurrence frequency distribution of SAGE II subvisual clouds is shown in Figure 3.17(b) and can be compared to Figure 3.12. In agreement between Figures 3.12, 3.16, 3.17(b), and 3.18, the maximum cirrus cloud occurrence is between 14 and 15 km altitude within the tropical latitudinal band. While there are differences between CALIPSO, SAGE II, and OSIRIS measurements, the general positions and magnitudes of the maxima and minima cloud occurrence frequencies occur in relatively close agreement.

Figure 3.19 shows the seasonal cloud occurrence frequency distributions from SAGE II observations between 1985 to 1990 and is analogous to Figures 3.13 and 3.14. The cloud maximum during

the summer season over India and southern China coincides with the active convection system associated with the Indian summer monsoons. Also, the subvisual cloud maximum occurring over Micronesia, namely around 120° longitude near the equator, shifts latitudinally with the seasons; it shifts toward India and southern China then intensifies during June to August, then migrates southeast to Indonesia during September to November and December to February.

To assure adequate sampling, *Wang et al.* (1996) average six years of SAGE II occultation data together to obtain results shown in Figures 3.17 and 3.19. Since OSIRIS captures enough sampling to form seasonal and yearly figures, an average figure representing multiple years of data is not necessary and an analysis can be made on a yearly basis. Figure 3.20 shows the yearly average cloud top occurrence frequency of clouds detected by OSIRIS in a three-kilometer layer below the local tropopause for the years 2005-2006, 2006-2007, 2007-2008, and 2008-2009, where each year begins in June. Here again, there are clear maxima cloud occurrences over Indonesia, the Congo rainforest in Africa, and over Central American rainforests and the Amazon and minima bands along ±30° latitude corresponding to the dry downwelling on the edge of the Hadley cells.

Wang et al. (1996) infer interpretations regarding STE and the dehydration processes of the stratosphere. From the SAGE II solar occultation measurements, *Wang et al.* (1996) explain how the dryness of the stratosphere is maintained by the cold trap dehydration mechanism. Here, tropospheric air passing into the stratosphere is dehydrated as the cool temperatures near the tropopause enforce the formation of clouds and precipitation effectively removing moisture from the air. They reason that regions subject to the cold trap dehydration mechanism coincide with regions having intense cloud activity. Furthermore, "the correspondence of the subvisual clouds to times and locations favorable to the cirrus formation is not surprising. It provides evidence that subvisual clouds are related either directly or indirectly to the development of ordinary cirrus clouds or cumulonimbus anvils" (*Wang et al.*, 1996).

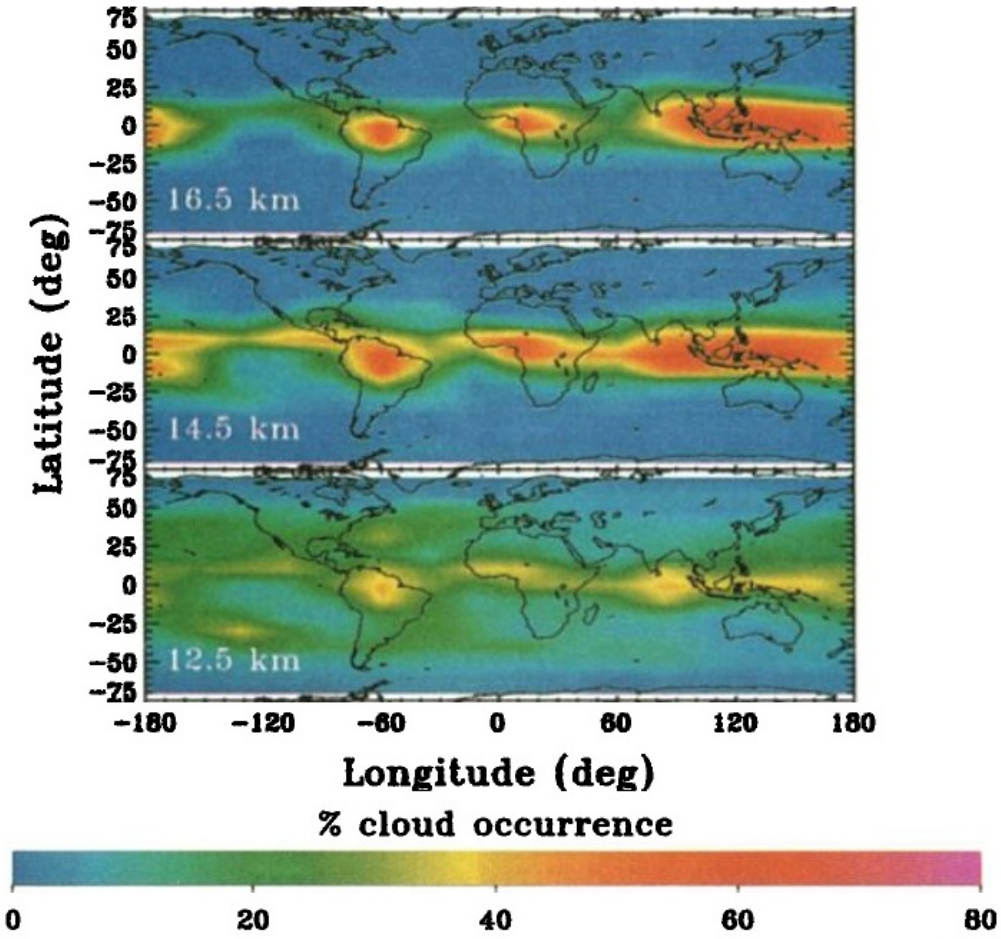

(a) Subvisual cloud occurrence frequency by SAGE II

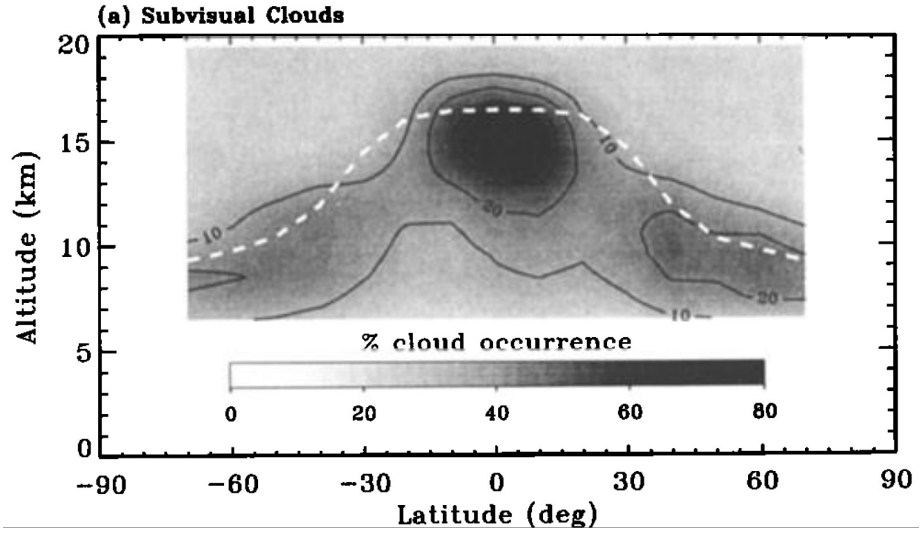

(b) Zonal subvisual cloud occurrence by SAGE II

Figure 3.17: (a) Global distribution, and (b) zonal average distribution between 1985 to 1990 of SAGE II subvisual cloud occurrence frequency; extracted from *Wang et al.* (1996) and reproduced by permission of American Geophysical Union.

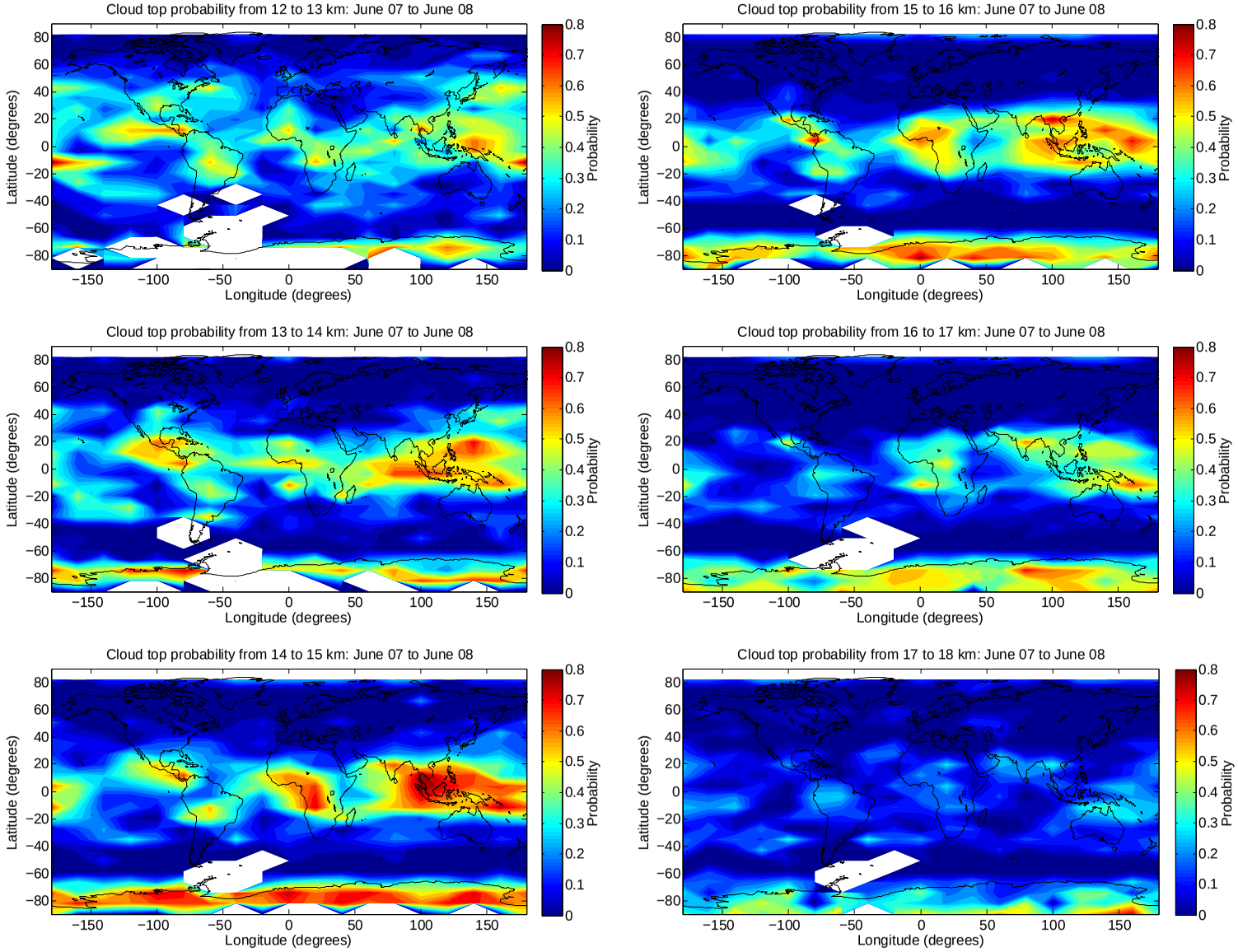

Figure 3.18: Average cloud top occurrence frequency of clouds detected by OSIRIS algorithm on an absolute altitude scale between June 2006 and June 2007.

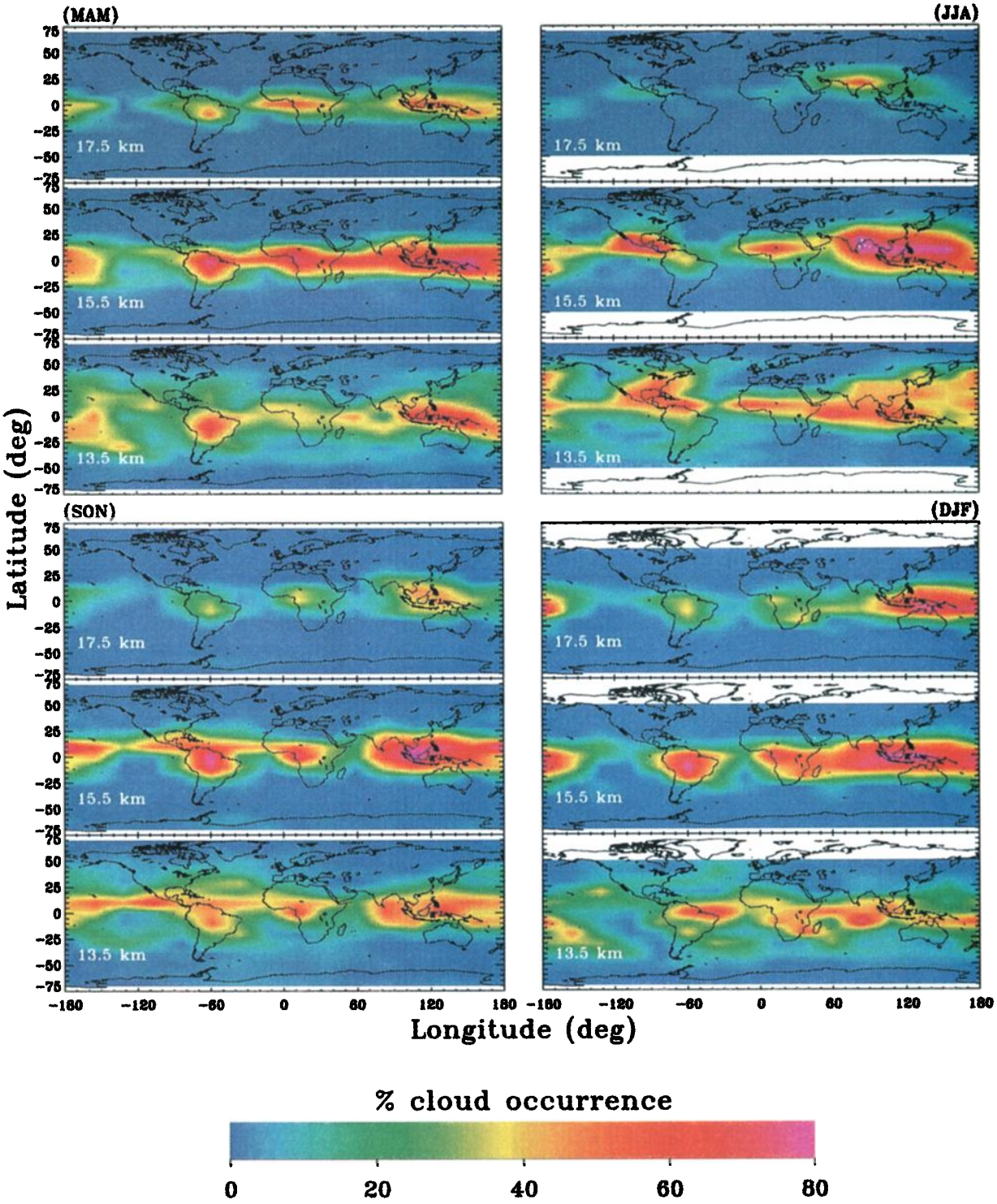

Figure 3.19: (a) Global seasonal distribution of SAGE II subvisual cloud occurrence frequency between 1985 to 1990; extracted from *Wang et al.* (1996) and reproduced by permission of American Geophysical Union.

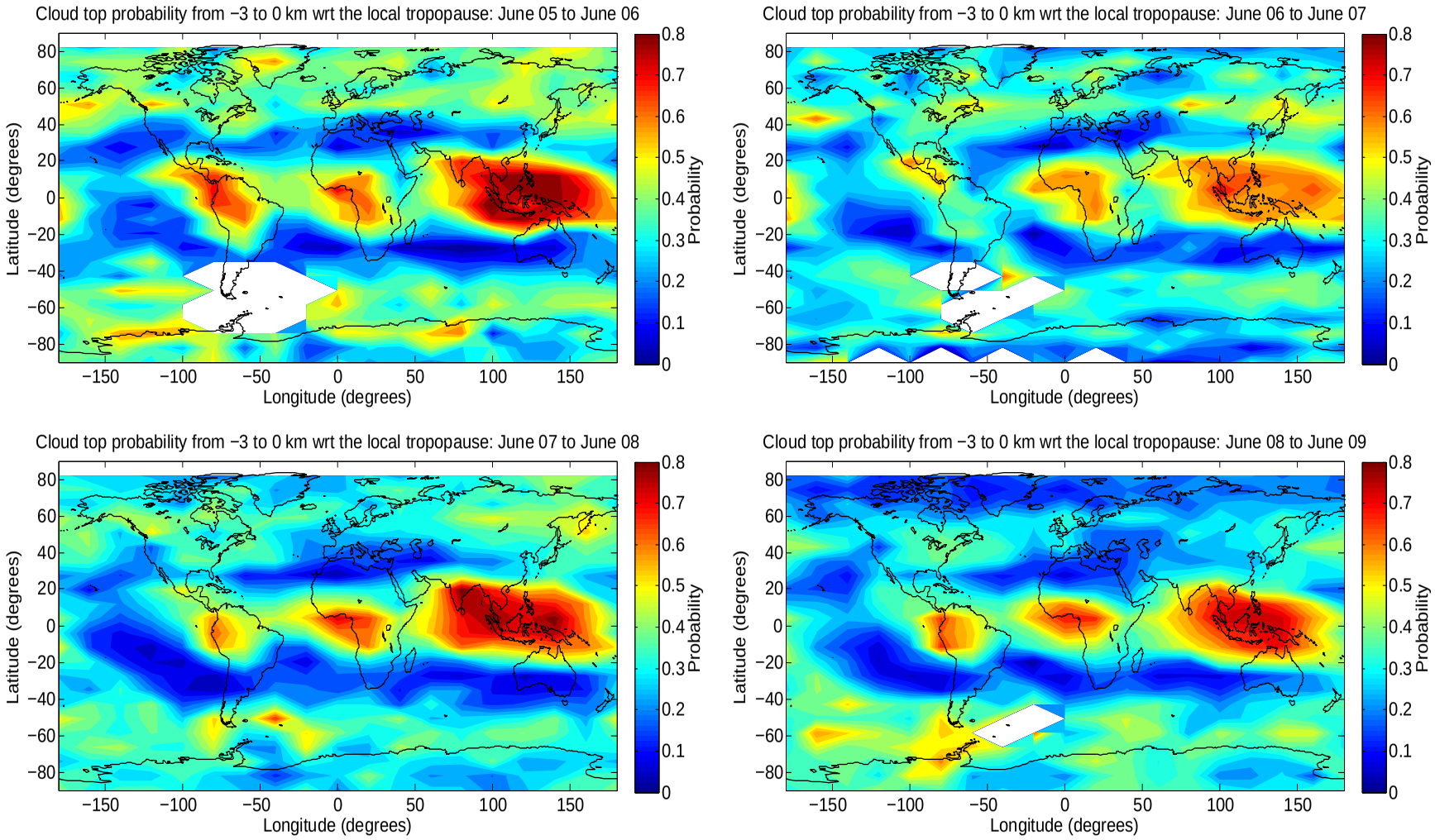

Figure 3.20: Yearly average cloud top occurrence frequency of clouds detected by OSIRIS algorithm in a three-kilometer thick layer below the local tropopause.

Chapter 4

Case Studies

The cloud detection technique developed in Chapter 3 is used in the following three case studies. The first study aims at connecting cloud occurrence frequencies to the distribution of water vapour in the lower stratosphere and is based on *Dessler* (2009). The interchange between transport and freeze-drying controls the water vapour balance within the stratosphere (*Read et al.*, 2008). Therefore, the formation of clouds can either contribute to the hydration or to the dehydration of the stratosphere. OSIRIS cloud detections along with water vapour measurements from the ACE instrument are used to confirm the measurements presented by *Dessler* (2009).

The second study makes use of the cloud detection technique to eliminate cloud-containing scans as to identify an ATAL in support of *Vernier et al.* (2011). The recently discovered presence of the ATAL accentuates the involvement deep convection has with the transport of aerosols into the upper atmosphere. The study undertaken as part of this work suggests the aerosol layer exhibits a diurnal cycle, which may be tied to the formation of cloud condensation nuclei from sulfur dioxide, as proposed by *Laaksonen et al.* (2000).

Finally, the cloud detection technique is applied to track the volcanic plume emitted from the Sarychev volcano eruption on 12 June 2009. Ash and dust in the volcanic plume cause enhanced scattering that can be detected and located in altitude using the limb technique. Tracking and monitoring volcanic plumes using satellite-derived data proves to be an effective way to mitigate aviation hazards.

4.1 Cloud Top Fraction and Connection to Water Vapour

Dynamical processes govern the chemical composition of the UTLS. The mechanisms responsible for the formation of clouds have a significant impact on the abundance of species, especially water vapour, in the stratosphere.

Water vapour is a prominent greenhouse gas and consequently has a significant effect on atmo-

spheric circulation through its involvement in the redistribution of energy and latent heat exchanges (*Schneider et al.*, 2010). Stratospheric water vapour is critical in determining stratospheric chemistry (*Kirk-Davidoff et al.*, 1999) and the radiative balance at the tropopause level (*de F. Forster and Shine*, 1999). An increase in stratospheric water vapour warms the troposphere and cools the stratosphere (*Solomon et al.*, 2010) through more longwave emissions to space (*Flury et al.*, 2012).

Stratospheric water vapour and the formation of clouds result from convective processes and vertical transport. Within the tropics, deep convection can extend into the stratosphere (*Alcala and Dessler*, 2002; *Gettelman et al.*, 2002) and is critical in determining the chemical composition of stratospheric air, including the abundance of trace species (*Dessler*, 2002). As *Brewer* (1949) recognized from observing the reduced concentration of water vapour in the lower stratosphere, air is dehydrated and clouds are created as it is transported upward through the cold-point tropopause.

The accepted understanding of transport in the lower stratosphere, namely the region above the tropopause in the extratropics and below the 380 K potential temperature level (*Hoskins*, 1991; *Holton et al.*, 1995), as in Figure 2.3, is that air is carried horizontally and isentropically through the tropical tropopause and vertically through slow downwelling of stratospheric air. Extratropical convection affects the lowermost stratosphere (*Roach*, 1967; *Poulida et al.*, 1996; *Fischer et al.*, 2003; *Hegglin et al.*, 2004; *Hess*, 2005), albeit its impact is subtle (*Holton et al.*, 1995). Convection driven by fossil fuel burning can also reach the overworld (*Fromm et al.*, 2000; *Fromm and Servranckx*, 2003; *Wang*, 2003; *Jost et al.*, 2004; *Livesey et al.*, 2004), that is the region beyond the 380 K potential temperature level.

The reciprocity between transport and freeze-drying regulates the amount of water vapour lofted into the stratosphere (*Read et al.*, 2008). Work by *Grosvenor et al.* (2007), *Corti et al.* (2008), and *Yang et al.* (2010) propose overshooting convection will radiatively lift water vapour into the stratosphere. Consequently, stratospheric water vapour and the growth of clouds are tied to convective processes and vertical ascent. Yet the question remains: Does the formation of clouds in the UTLS contribute to the hydration or to the dehydration of the stratosphere? By obtaining an understanding of cloud formation, a clearer picture outlining the distributions of trace species, such as water vapour, and the transport of air between the troposphere and the stratosphere can be achieved.

Using the CALIPSO cloud measurements, *Dessler* (2009) quantified the occurrence of clouds in the UTLS and correlated their presence with the water vapour distribution using measurements solely from the summertime nighttime northern hemisphere. Nighttime measurements were used because the signature of thin cirrus is too weak to reliably measure when the lidar signal is con-

taminated by sunlight. Thus, since daytime measurements were excluded from this analysis, the diurnal cycle of cloud formation and distribution changes are not captured in this study. Cloud measurements between June to September 2007 and 2008 were used because this corresponds to the time of year when convection is most likely to reach into the extratropical stratosphere.

Dessler (2009) showed there are high occurrences of clouds over regions where there is intense convective activity. In particular, there are strong maxima over the Asian monsoon and over Central America. He noted the zonal variability in cloud occurrence decreases with increasing latitude. This is shown in Figure 4.1(a) where the percent of cloud top observations per kilometer as observed by CALIPSO is plotted for longitude-altitude segments for three latitude ranges: 25°N to 30°N, 40°N to 45°N, and 55°N to 60°N. This figure is extracted from *Dessler* (2009). The thick black lines outline the tropopause altitude as obtained from the Goddard Earth Observing System Model (GEOS) version 5 reanalysis data, which is a combination of the lapse rate tropopause at low latitudes and the dynamical tropopause at middle and high latitudes. For comparison, Figure 4.1(b) shows the cloud top occurrence frequency as measured by OSIRIS using the cloud top detection technique developed in the previous chapter. The altitude-longitude slices correspond to the 22.5°N to 30°N, 37.5°N to 45°N, and 52.5°N to 60°N latitudinal ranges. The thick black lines show the tropopause height in accordance with the WMO definition based on calculated lapse rates from reanalysis NCEP data.

The agreement between the data sets is quite good. The shapes and longitudinal positions of the cloud maxima over the Asian monsoon and over Central America occur in relatively close agreement. At high latitudes, the cloud distribution is somewhat even over all longitudes. However, the features in Figure 4.1(b) occur at lower altitudes relative to the tropopause than those in Figure 4.1(a), which can be attributed to two reasons. First, the instruments have different vertical resolutions; OSIRIS and CALIPSO have approximately 2 and 0.5 km vertical resolutions, respectively. Thus, CALIPSO's enhanced resolution allows positioning cloud detections vertically with greater accuracy. Second, OSIRIS measurements are subjected to a limb viewing bias from detecting clouds on the near or far side of the tangent point. As illustrated in Figure 4.2, a cloud detected on the far side of the tangent point is recorded at the altitude of the tangent point, namely at altitude z_1. However, the detected cloud is actually positioned at a higher altitude $z_2 > z_1$ as its location is shifted latitudinally relative to the location of the tangent point, hence introducing a limb viewing bias. Successive measurements made by OSIRIS are spaced on average 2 to 2.5 km vertically, so on average this effect will lower the measured OSIRIS distribution by approximately 1 km.

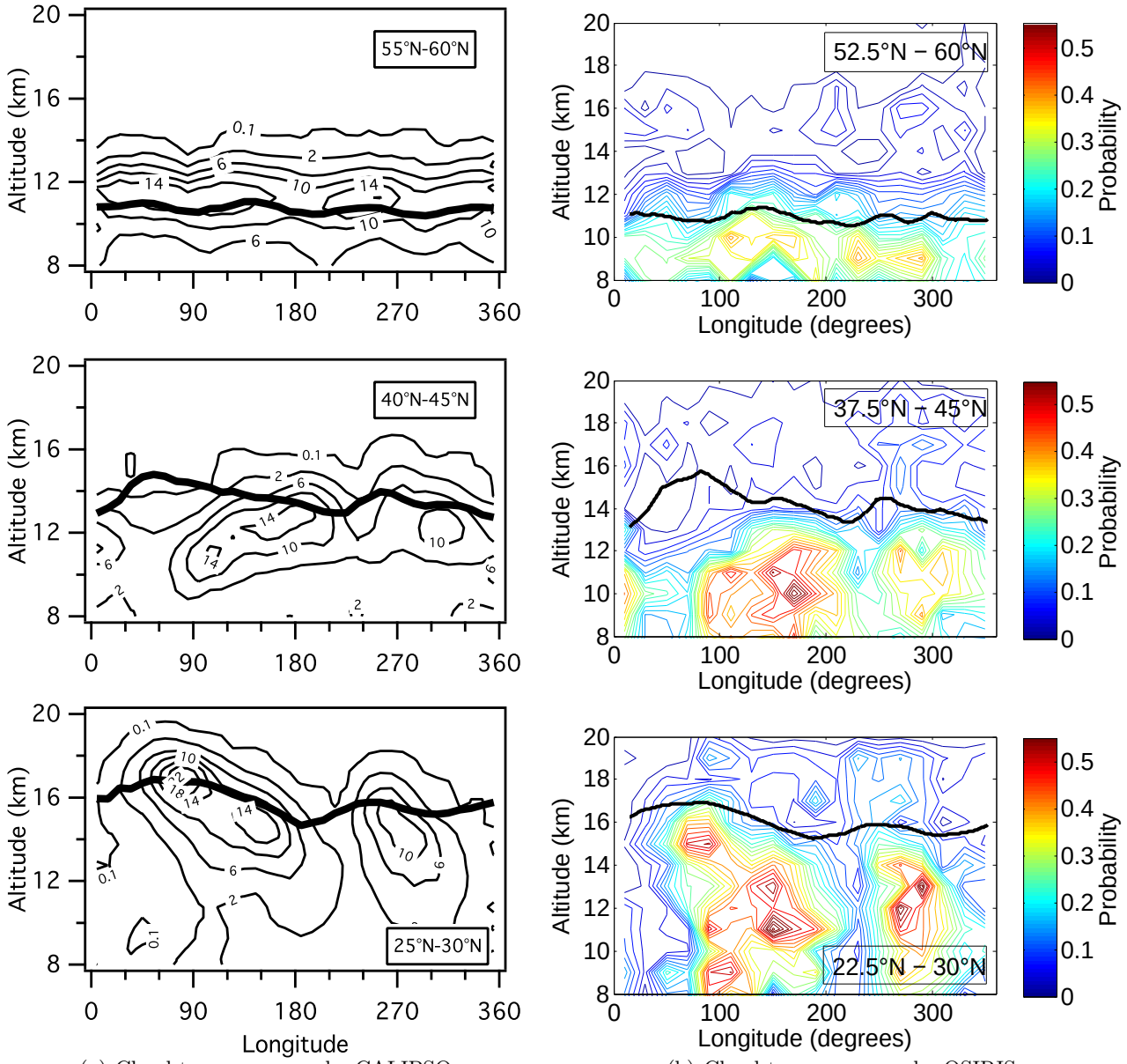

(a) Cloud top occurrence by CALIPSO

(b) Cloud top occurrence by OSIRIS

Figure 4.1: Percent of cloud top observations per kilometer as observed by (a) CALIPSO, which is extracted from *Dessler* (2009) and reproduced by permission of American Geophysical Union, and (b) OSIRIS from June to September 2007 and 2008. The thick black lines outline the tropopause altitude.

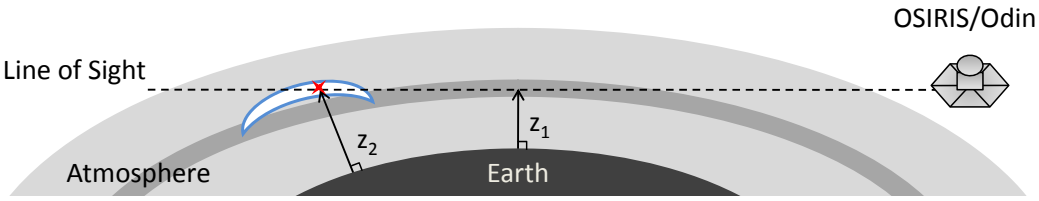

Figure 4.2: Cloud measurement on the far side of the tangent point.

Also evident in Figure 4.1, the tropopause height falls in altitude with increasing latitude. *Dessler* (2009) showed convection falls off more slowly with latitude over Central America than it does over the Asian monsoon. He further explained that the number of cloud tops seen above the tropopause increases with latitude because the cloud top distribution in potential temperature remains fixed while the tropopause height descends with increasing latitude.

In an effort to compare the dominant convective regions, *Dessler* (2009) computed the zonal average cloud top fraction as a function of latitude for two sectors, one ranging from 45° to 145° longitude covering the Asian sector, and a second ranging from 235° to 305° longitude covering the North American sector. That is, longitudinal slices from the cloud top observation maps were selected and averaged across the longitude dimension as to obtain the mean altitude-latitude cloud top distributions, or *zonal* average distributions. Figures 4.3(a) and 4.3(c) show the zonal average cloud top fraction in percent for the Asian and North American sectors, respectively, from June to September 2008 of CALIPSO cloud measurements and are extracted from *Dessler* (2009). The zonal average cloud top fraction as measured by OSIRIS using the technique developed here was also computed for the Asian and North American sectors and are shown in Figures 4.3(b) and 4.3(d), respectively. The thick black lines trace the tropopause altitude following the descriptions above. The sectors are, generally speaking, similar because the contour lines follow the tropopause level and the maxima cloud top frequency occur at tropical latitudes. Again, the features measured by OSIRIS in both sectors are approximately 2 km lower than those measured by CALIPSO as a result of the different vertical resolutions and the limb viewing bias.

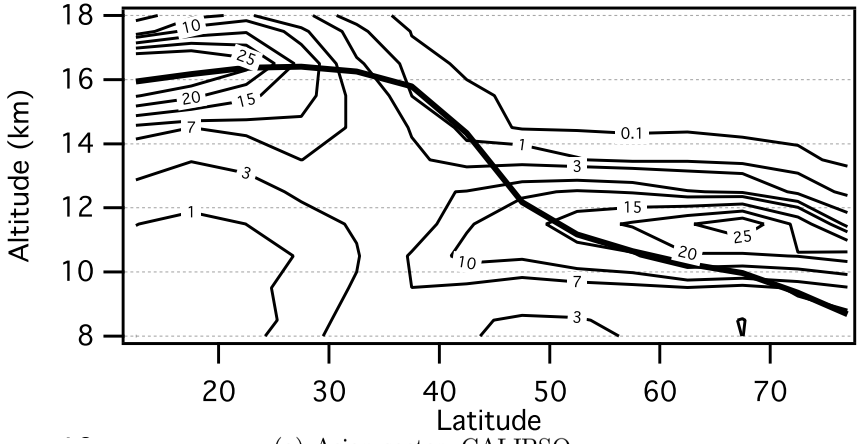

(a) Asian sector; CALIPSO

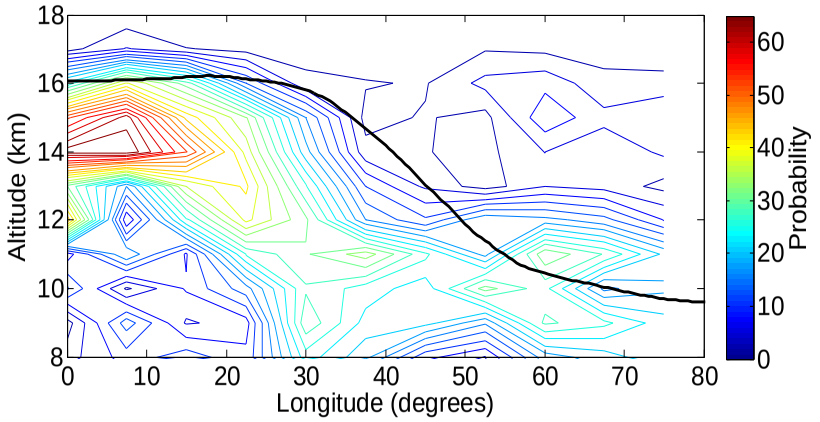

(b) Asian sector; OSIRIS

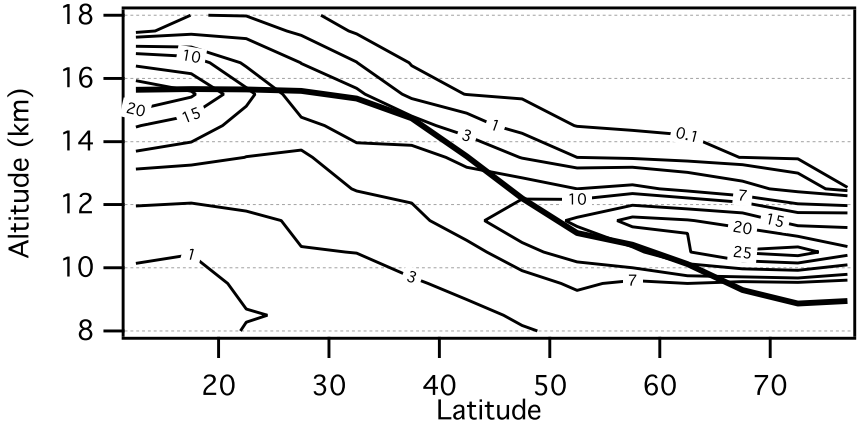

(c) North American sector; CALIPSO

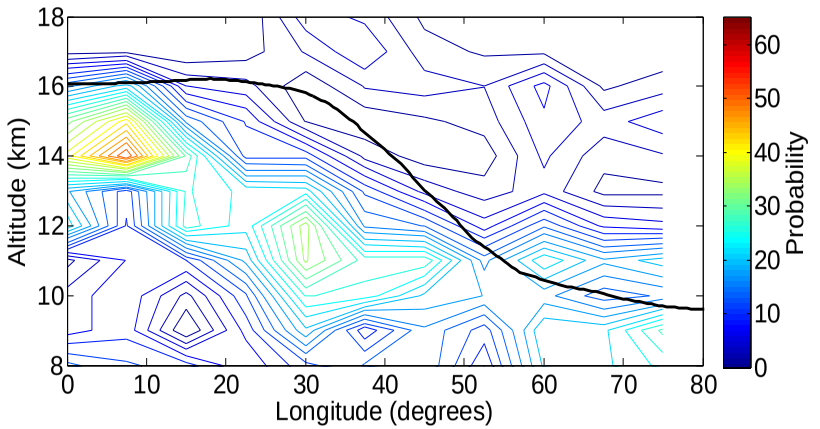

(d) North American sector; OSIRIS

Figure 4.3: Zonal average cloud top fraction in percent from June to September 2008 for (a), (b) the Asian sector ranging between 45° and 145° longitude, and (c), (d) the North American sector ranging between 235° and 305° longitude. The left column was obtained using CALIPSO measurement and is extracted from *Dessler* (2009) and reproduced by permission of American Geophysical Union and the right column was obtained using the cloud detection technique from OSIRIS measurements. The thick black lines outline the average tropopause altitude.

A quantitative comparison between the two sectors is presented in Figures 4.4(a) and 4.4(b), which show the straight difference between these two sectors. Positive anomalies correspond to higher frequencies in the Asian sector. At tropical latitudes, the positive maximum near the tropopause and the negative maximum below correspond to higher cloud top occurrence frequencies in the Asian and North American sectors, respectively. In agreement with *Dunkerton* (1995), the convection system over the Asian monsoon is higher and deeper relative to that over Central America. At mid-latitudes, the converse is true: the negative anomaly at the tropopause level confirms the observation from Figure 4.1 where convection falls off more slowly in the North American sector than it does in the Asian sector. Finally, at high latitudes, the positive maximum shows there are higher cloud top occurrence frequencies in the Asian sector.

In a similar manner, the zonally averaged water vapour mixing ratio for the Asian and the North American sectors between June to September 2008 were plotted. These are shown in Figure 4.5(a) where the top and bottom plots correspond to the Asian and North American sectors, respectively. In this work, water vapour measurements from the ACE solar occultation satellite are used. ACE is a Canadian satellite and its mission is to further our understanding in the dynamical and chemical processes involved with the ozone distribution in the stratosphere. ACE was launched August 2003 and flies in a circular polar orbit near 650 km altitude with a 74° inclination while capturing measurements in the tropical, mid-latitude, and high latitude bands, specifically between 85°S to 85°N. A Fourier transform infrared spectrometer (FTS) is onboard ACE. ACE-FTS operates from 750 to 4400 cm^{-1} with resolution 0.02 cm^{-1} and measures the vertical profiles of trace gases, including water vapour, and temperature with a 3 to 4 km vertical resolution from cloud tops up to around 150 km (*Bernath et al.*, 2005). In Figure 4.5(a), the mixing ratio at the tropopause level increases with latitude as the tropopause height falls in altitude with latitude. Generally, the water vapour contour lines follow isentropic levels. There is no outstanding difference between the distributions of the two sectors.

Figure 4.5(b) shows the straight difference in the zonal average water vapour mixing ratio distributions between the Asian and the North American sectors where positive anomalies correspond to higher mixing ratios in the Asian sector. The top image is the difference between the plots in Figure 4.5(a) from ACE-FTS water vapour data while the bottom plot is the analogous difference using measurements from the Microwave Limb Sounder (MLS) reported in *Dessler* (2009).

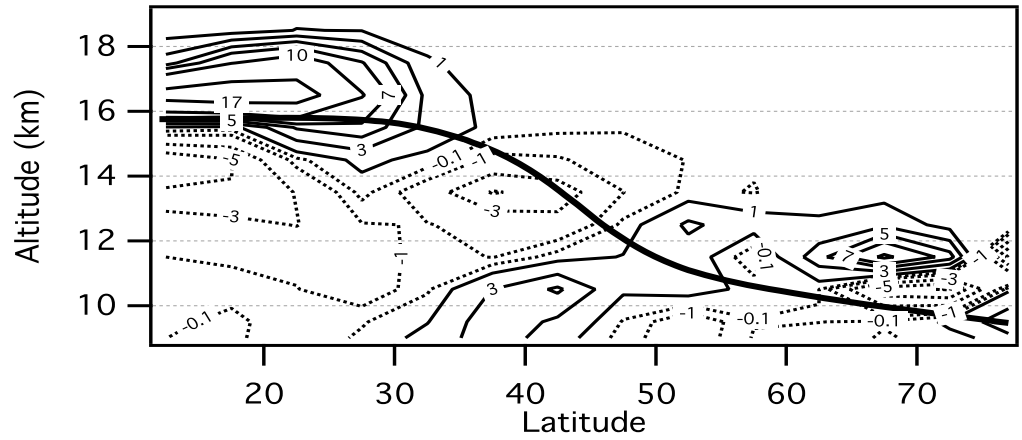

(a) Zonal difference, CALIPSO

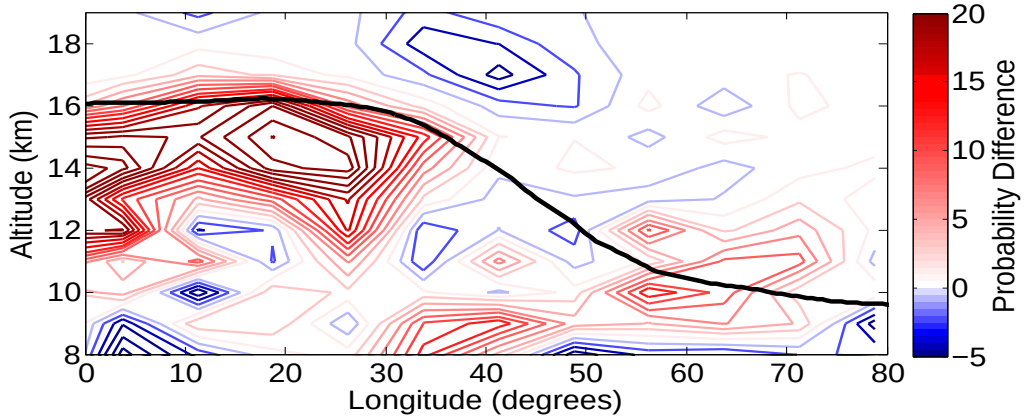

(b) Zonal Difference, OSIRIS

Figure 4.4: The straight difference in the zonal average cloud top fraction between the Asian and the North American sectors with positive values corresponding to higher values in the Asian sector from June to September 2008. Figure 4.4(a) was obtained using CALIPSO measurement and is extracted from *Dessler* (2009) and reproduced by permission of American Geophysical Union and Figure 4.4(b) was obtained using the cloud detection technique from OSIRIS measurements. The thick black lines outline the average tropopause altitude.

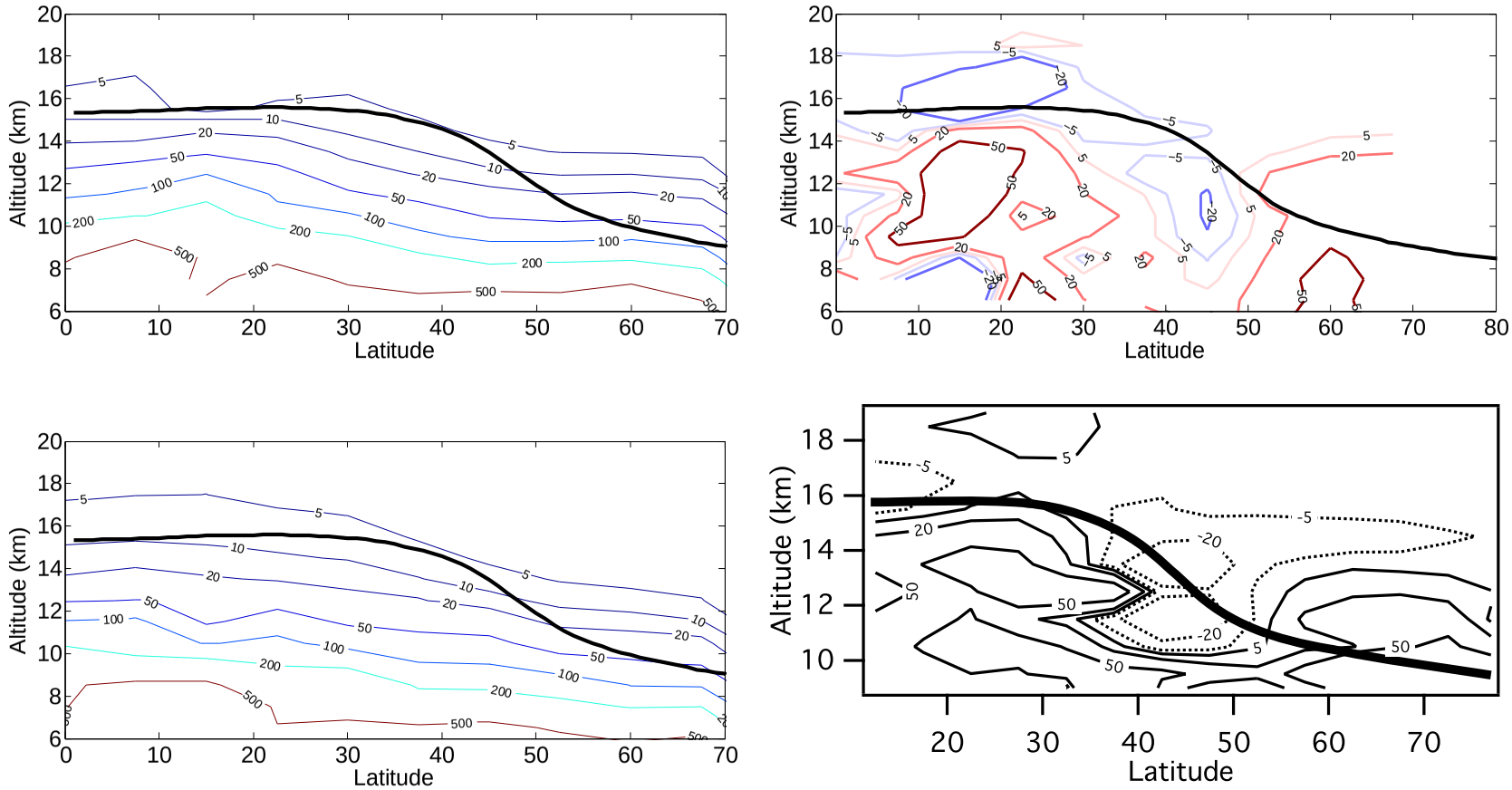

(a) Zonal average water vapour mixing ratio by ACE

(b) Zonal difference between sectors by ACE and MLS

Figure 4.5: Zonal average water vapour mixing ratio in parts per million by volume of (a, top) the Asian sector ranging between 45° and 145° longitude, and (a, bottom) the North American sector ranging between 235° and 305° longitude; and (b) the straight difference between the two sectors, with positive values corresponding to higher values in the Asian sector. All plots were obtained from ACE water vapour data from June to September 2008 except for the plot (b, bottom), which was obtained using MLS measurement and is extracted from *Dessler* (2009) and reproduced by permission of American Geophysical Union. The thick black lines outline the average tropopause altitude.

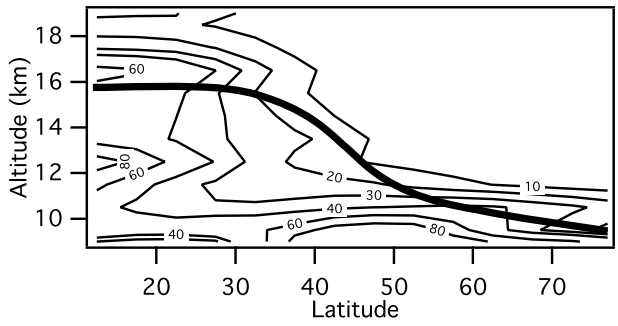

Figure 4.6: Zonal average relative humidity in percent from June to September 2008; extracted from *Dessler* (2009) and reproduced by permission of American Geophysical Union. The thick black lines outline the average tropopause altitude.

MLS is onboard NASA's Aura satellite. The satellite was launched July 2004 and flies in a sun-synchronous orbit at approximately 705 km altitude with a 98° inclination providing a 82°S to 82°N latitudinal coverage. Aura has an ascending north-bound equatorial crossing at 1345 h local time and has a 98.8 min orbit. The MLS instrument consists of five radiometers at 118, 190, 240, 640, and 2500 GHz and its field of view scans the limb of the atmosphere while observing millimeter- and submillimeter-wavelength thermal emissions. The MLS has a forward look-direction, that is its field of view is pointed in the forward direction of orbital motion (*Waters et al.*, 2006). Vertical water vapour profiles are retrieved in the UTLS region about every 1.5 km where measurements have a vertical resolution of 2 to 3 km, a horizontal along-track resolution near 300 km, and an accuracy between 10 to 20% (*Dessler*, 2009).

The plots in Figure 4.5(b) exhibit similar features with higher zonal average water vapour mixing ratio in the Asian sector than in the North American sector below the tropopause at low latitudes. At mid-latitudes, the zonal average water vapour mixing ratio is nearly 20% higher in the North American sector than it is in the Asian sector, consistent with *Gettelman et al.* (2004).

In Figure 4.6, *Dessler* (2009) demonstrates the zonal average relative humidity in percent from June to September 2008. Relative humidity was computed from GEOS temperature fields and is high in the troposphere and low in the stratosphere. Within the stratosphere, relative humidity is higher at lower latitudes than it is at higher latitudes because of the low temperatures there; temperature increases with latitude in the stratosphere so relative humidity consequently decreases.

Dessler (2009) made an important connection between cloud top occurrences, water vapour mixing ratio, relative humidity, and the process of dehydration of air entering the stratosphere.

He showed that at low latitudes, enhanced cloud occurrences and high water vapour mixing ratio are anticorrelated, especially in the Asian sector where there is intense convective activity. *Dessler* (2009) attributed this disassociation to the high relative humidity occurring in regions of maximum cloud top occurrences, which prevents ice lofted by convection to evaporate and encourages in situ formation of clouds. Hence, convection has little effect on water vapour mixing ratio there. At mid-latitudes, regions of high cloud occurrences and high water vapour mixing ratio are closely matched. Here, deep convection over Central America drives cloud ice into the stratosphere where the relative humidity is low, allowing the cloud ice to evaporate leading to enhanced water vapour. In summary, the effect clouds have on water vapour is largely controlled by relative humidity. At low latitudes, in-situ formation of clouds in regions of high relative humidity reduces the water vapour mixing ratio and possibly leads to irreversible dehydration (*Dessler*, 2009). At middle and high latitudes, clouds are highly correlated with convection and tend to moisten (*Dessler and Sherwood*, 2004) as cloud ice evaporates in regions of low relative humidity and consequently increases water vapour. OSIRIS cloud detections and ACE water vapour measurements developed as part of this work show a similar result and lend further credence to this theory.

4.2 Asian Tropopause Aerosol Layer

The TTL is often regarded as a gateway for tropospheric air entering the stratosphere (*Holton et al.*, 1995; *Fueglistaler et al.*, 2009). This route, however, is not exclusive because the Asian monsoonal circulation, consisting of a large anticyclone driven by deep and vigorous convection, provides an additional course (*Gettelman et al.*, 2004; *Randel et al.*, 2010). Anthropogenic atmospheric sulfur from Asia is transported into the lower stratosphere through monsoonal convection; the anticyclone advects boundary layer air vertically and horizontally into the upper atmosphere (*Randel and Park*, 2006). Transport of anthropogenic and volcanic species to higher altitudes through the anticyclone can potentially alter the chemical balance of the stratosphere and affect climate below. As *Vernier et al.* (2011) question, does the Asian monsoonal circulation also carry aerosols and their gaseous precursors to the upper atmosphere?

Vernier et al. (2011) reported the presence of an ATAL extending between eastern Mediterranean to western China and vertically between 14 and 18 km from measurements made by CALIPSO. Nighttime polarization measurements at 532 nm were used to detect the presence of clouds and scans containing clouds or ice crystals, meaning those with a mean volume depolarization ratio

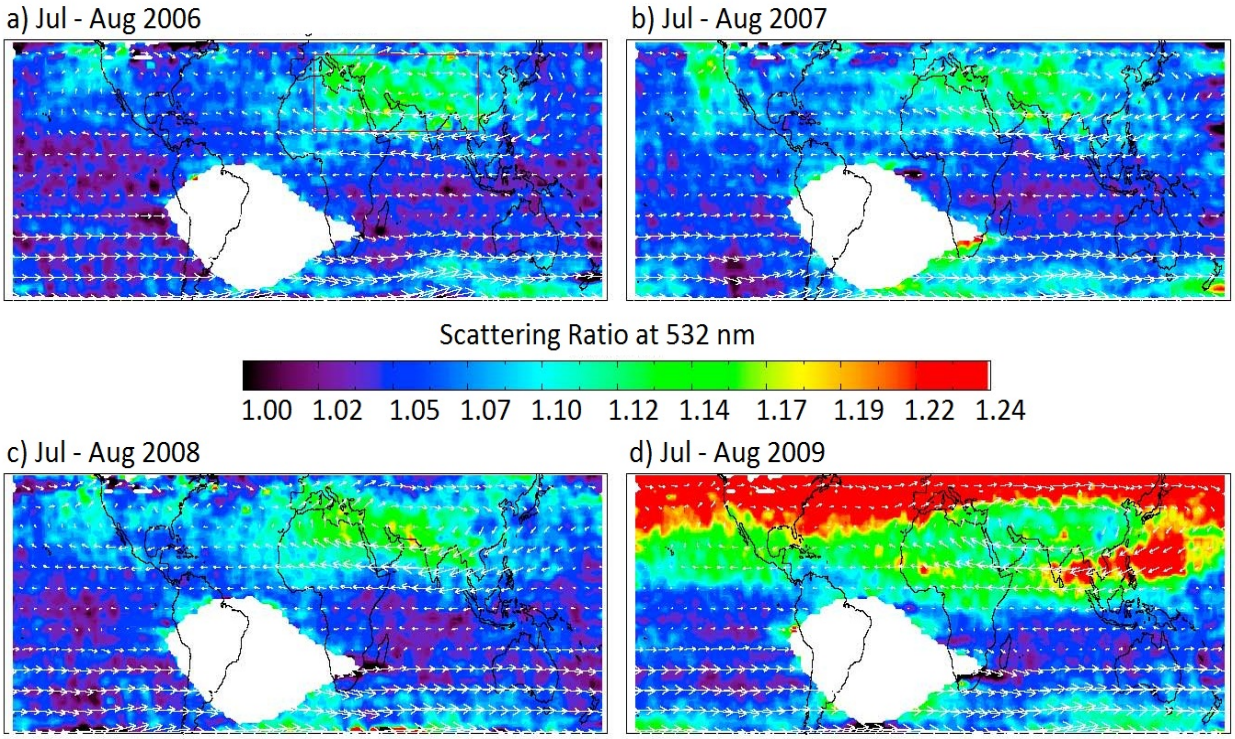

Figure 4.7: Mean scattering ratio maps between 15 and 17 km at 532 nm from CALIPSO between July and August 2006, 2007, 2008, and 2009; extracted from *Vernier et al.* (2011) and reproduced by permission of American Geophysical Union.

greater than 5%, were removed. The remaining measurements were used to identify an aerosol layer. Recall that the lidar takes nighttime measurements at 0130 h local time.

In their work, *Vernier et al.* (2011) show maps of the mean scattering ratio (SR) between 15 and 17 km altitude in July and August, which reveal the aerosol layer confined by the Asian anticyclone. The scattering ratio is the ratio of aerosol plus molecular backscatter to the molecular alone and was computed using the total backscatter (aerosol and molecular) from CALIPSO. Molecular backscatter is modelled using ECMWF model density (*Vernier et al.*, 2011).

Results extracted from *Vernier et al.* (2011) from July and August 2006, 2007, 2008, and 2009 are shown in Figure 4.7. The mean wind fields from ECMWF are superimposed and clearly outline the Asian anticyclone spanning between eastern Mediterranean to northern Africa and stretching from western China to Thailand. Data within the SAA region are discarded. The mean SR shows an aerosol layer confined within the anticyclone with SR values ranging between 1.12 and 1.18 occurring in the years 2006 to 2008. The repetitive occurrence both in time and position suggest

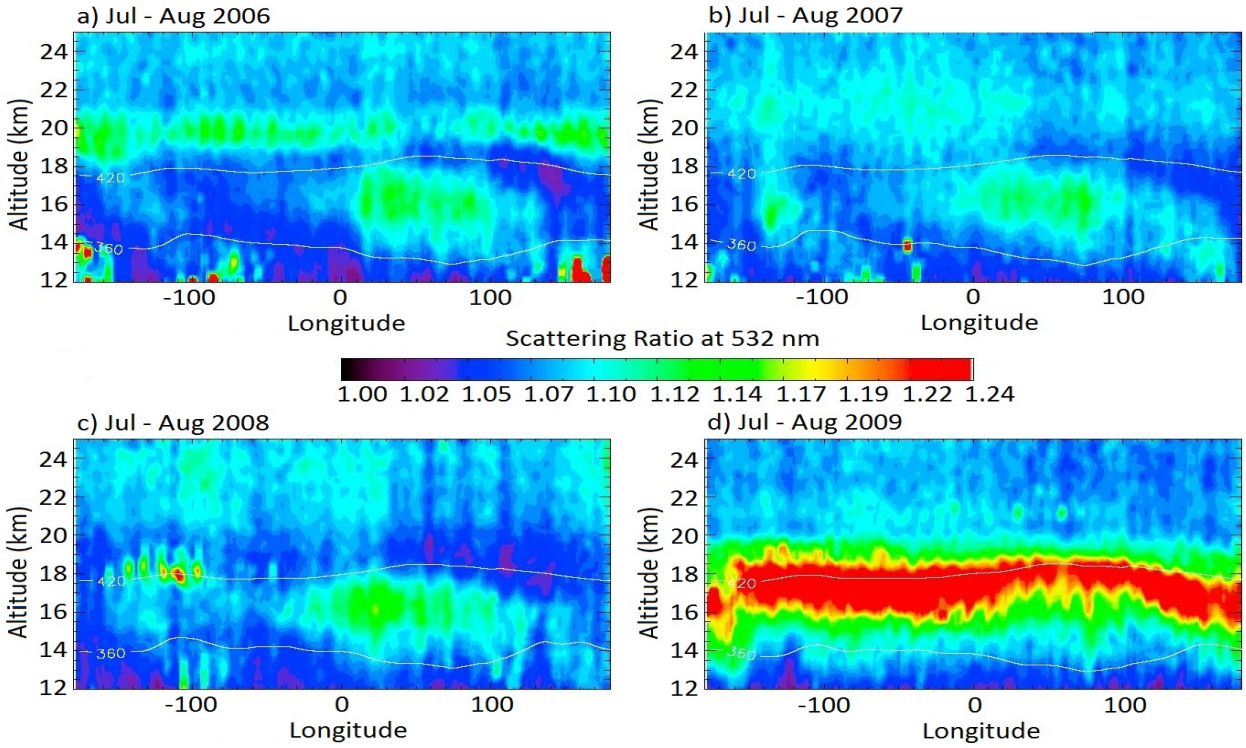

Figure 4.8: Mean scattering ratio longitudinal cross section between 15° and 45° latitude at 532 nm from CALIPSO between July and August 2006, 2007, 2008, and 2009; extracted from *Vernier et al.* (2011) and reproduced by permission of American Geophysical Union.

the aerosol layer is likely of non-volcanic origin. However, the results for the year 2009 are quite different; the northern hemisphere is largely saturated with volcanic aerosols. On 12 June 2009, the Sarychev volcano, located in the Kuril Islands northeast of Japan, erupted releasing approximately 1.2 ± 0.2 Tg of volcanic sulfur dioxide into the atmosphere (*Haywood et al.*, 2010). Interestingly, the volcanic plume circumvents northern Asia emphasizing the isolation of the air within the anticyclone, consistent with *Park et al.* (2008). Details regarding the volcanic plume follow in the next section. *Vernier et al.* (2011) also show the longitudinal cross section of the SR between 15° and 45° latitude, shown in Figure 4.8. The aerosol layer is observed between 14 and 18 km in height.

The PDF of the SR from cloud-free scans is used to understand the optical properties of the ATAL. In Figure 4.9, *Vernier et al.* (2011) compare four SR distributions during the monsoon season of July and August for every year between 2006 to 2009 to the SR distribution during a reference period of December and January 2008 when monsoon activity was minimal. The tail of positive SR values in the 2009 distribution is due to volcanic aerosols lingering in the atmosphere

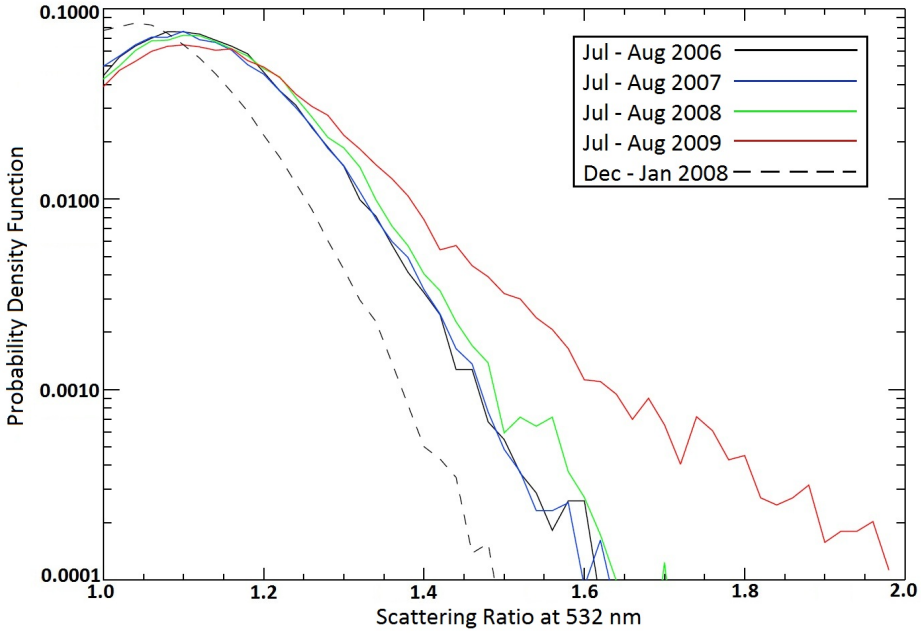

Figure 4.9: Probability density function of scattering ratio values for cloud-free scans taken between 15° and 45° latitude, 15 to 17 km altitude; extracted from *Vernier et al.* (2011) and reproduced by permission of American Geophysical Union.

during the monsoon season. The PDFs of the scattering ratio are normally distributed and the maxima of these peaks are the mean SR values for the corresponding seasons. The maximum SR for distributions representing the monsoon season is approximately 1.1 and the maximum SR for the reference season curve is below 1.05. The shift in the mean SR value occurs because the signal is brighter due to enhanced scattering within the ATAL.

The Gaussian distributions in Figure 4.9 are analogous to the cloud-free distribution peak shown in Figure 3.2(b). Since *Vernier et al.* (2011) removed scans containing clouds with polarization measurements, only the cloud-free distribution remained. Therefore, the shift in the Gaussian maxima between the monsoon season and the reference season demonstrates that the average SR calculated in Figure 4.9 is not influenced by some cloudy points sifting through the sorting algorithm, but rather due to an increase in aerosol background (*Vernier et al.*, 2011).

To further explore the work done by *Vernier et al.* (2011), the mean scattering residual (R) between 15° and 45° latitude for July and August was computed using OSIRIS limb scattered radiance profiles measured on the descending track of Odin's orbit at 800 nm. Note that OSIRIS measurement on the descending track occur around 0600 h local time. The spectral wavelength of 800 nm is chosen because, as explained in Section 2.6.3, the atmosphere is optically thin down to the troposphere at long wavelengths. The objective is to use the cloud detection technique to remove

cloudy measurements and determine if the ATAL is detectable with limb scatter measurements. Note that R is essentially the logarithm of SR. As in Section 3.1, the scattering residual, R, compares the measured radiance to the molecular radiance from an aerosol- and cloud-free atmosphere. The molecular radiance was obtained from the SASKTRAN model and an altitude normalization was performed. Figure 4.10 shows the R longitudinal cross section distributions derived from OSIRIS radiance measurements and SASKTRAN molecular profiles on an altitude scale relative to the local tropopause.

In Figure 4.10(a), all scans falling within the latitudinal limits of 15° and 45° during the months of July and August 2006, 2007, and 2008 were included; all cloud-free and cloud-containing scans were considered. The mean scattering residual was computed as a logarithmic difference between the normalized measured and the normalized molecular radiance profiles. That is,

$$R = \ln\left(\frac{\tilde{I}_{\text{measured}}}{\tilde{I}_{\text{modelled}}}\right). \tag{3.2}$$

The high R regions between -125° and -75° longitude and 50° and 170° longitude correspond to the Central American and Asian monsoon sectors, respectively. These regions, as shown previously, are areas of intense convective activity and correspondingly have high probabilities of cloud occurrences.

Figure 4.10(b) is analogous to Figure 4.10(a), but was generated using only cloud-free scans. The cloud detection technique described in Chapter 3 was employed to identify scans containing clouds thus making it possible to select only those scans deemed cloud-free. Since this plot represents the mean cloud-free R longitudinal cross section for scans between 15° and 45° latitude for July and August 2006, 2007, and 2008, it is compared to the work done by *Vernier et al.* (2011) in Figure 4.8. Note that Figure 4.8 is plotted on an absolute altitude scale while Figure 4.10 is plotted on a scale relative to the local tropopause. The high R in the stratosphere is due to the stratospheric aerosol layer. In Figure 4.10(b), there is a subtle indication of the presence of an ATAL.

The anomaly of the cloud-free scans was computed and is shown in Figure 4.10(c). Here, the average vertical profile from Figure 4.10(b) was subtracted from the mean cloud-free R longitudinal cross section distribution. As a result, the ubiquitous stratospheric aerosol layer is less apparent and protruding features are more visible. Features suggesting the presence of an ATAL appear in Figure 4.10(c), which was generated from the same set of cloud-free scans used in Figure 4.10(b). Similar to Figure 4.8 by *Vernier et al.* (2011), aerosol enhancements are seen between -150° and -75° longitude over the Central American sector and between 10° and 125° longitude over the Asian sector.

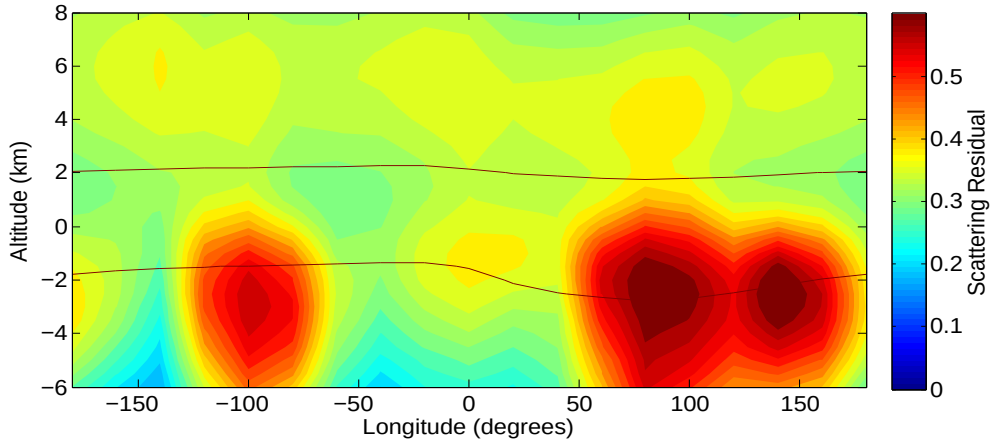

(a) All scans

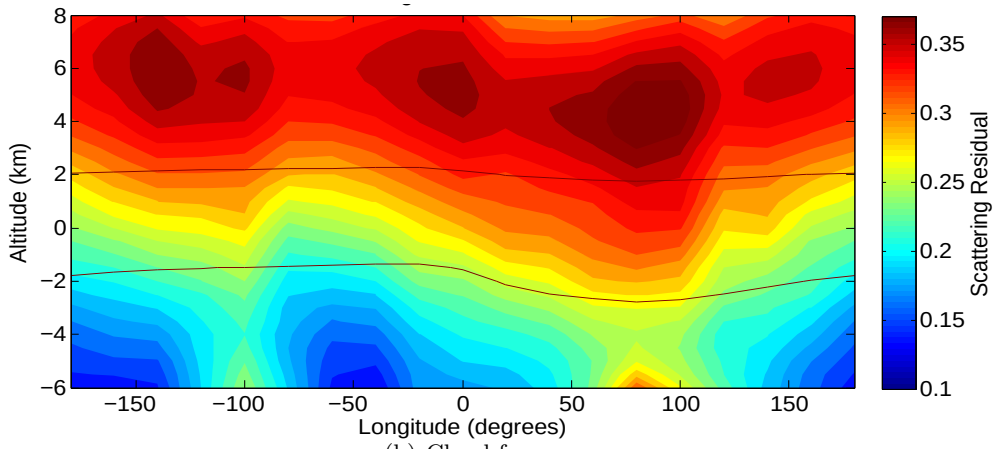

(b) Cloud-free scans

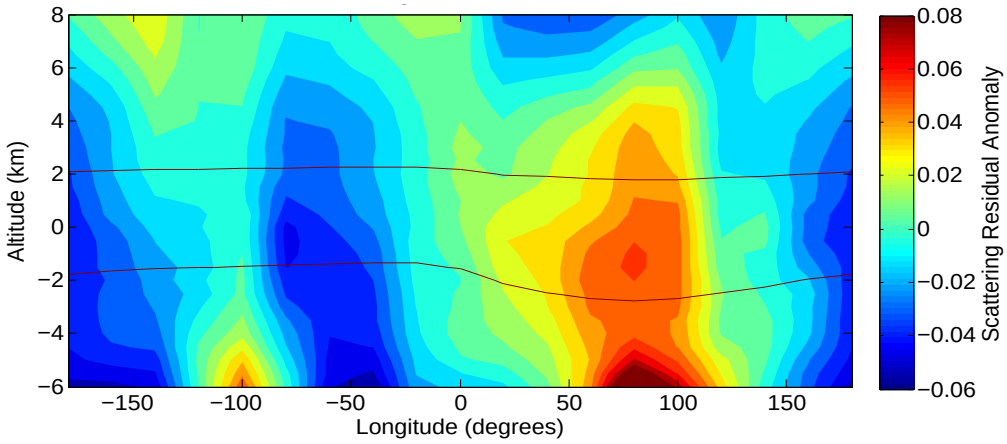

(c) Anomaly of cloud-free scans

Figure 4.10: The mean scattering residual longitudinal cross section between 15° and 45° latitude for July and August 2006, 2007, and 2008 using OSIRIS limb scattered radiance profiles measured on the descending track of Odin's orbit at 800 nm; (a) all scans, (b) cloud-free scans, and (c) anomaly of cloud-free scans. The mean potential temperature levels at 380 and 420 K are plotted in solid dark red. The vertical axis is shown with respect to the local tropopause; negative values correspond to altitudes below the tropopause level.

From the results presented in Figure 4.10(c), it is clear the cloud detection technique can be used to identify the ATAL. The cognate yearly anomaly mean cloud-free R longitudinal cross section distributions are shown in Figure 4.11 for the years 2006 to 2009 and are compared to the mean SR longitudinal cross sections in Figure 4.8 from *Vernier et al.* (2009). Recall that R is equivalent to the logarithm of SR, so the colour scales will not be identical. Furthermore, Figure 4.8 is plotted on an absolute altitude scale and Figure 4.11 is plotted on a scale relative to the local tropopause. With these differences in mind, the anomalies in the yearly plots occur in relatively close agreement.

The composition of the ATAL remains unclear. According to *Vernier et al.* (2011), these aerosols are of non-volcanic origin because the ATAL occurs consistently between the years 2006 and 2008 in July and August when there is minimal volcanic activity in roughly the same position. Also, since profiles with a mean volume depolarization ratio greater than 5% were excluded in the analysis, these aerosols are not ice crystals. The optical characteristics suggest these particles are spherical. However, they could plausibly be very small aerosols with effective radius smaller than $0.1\,\mu$m, which complies with the Mie theory and T-matrix calculations (*Vernier et al.*, 2011).

The vertical upwelling structures occurring within the convective regions over Central America and the Asian monsoon are notable features in Figures 4.10(c) and 4.11. Consistent with *Gettelman et al.* (2004) and *Randel et al.* (2010), these regions of deep convection, which are characterized by large vertical ascent of air masses, channel air between the troposphere and the stratosphere. Although the origin and nature of the ATAL is uncertain accroding to *Vernier et al.* (2011), its presence underlines the involvement deep convection has in the transport of aerosols and their precursors into the upper atmosphere.

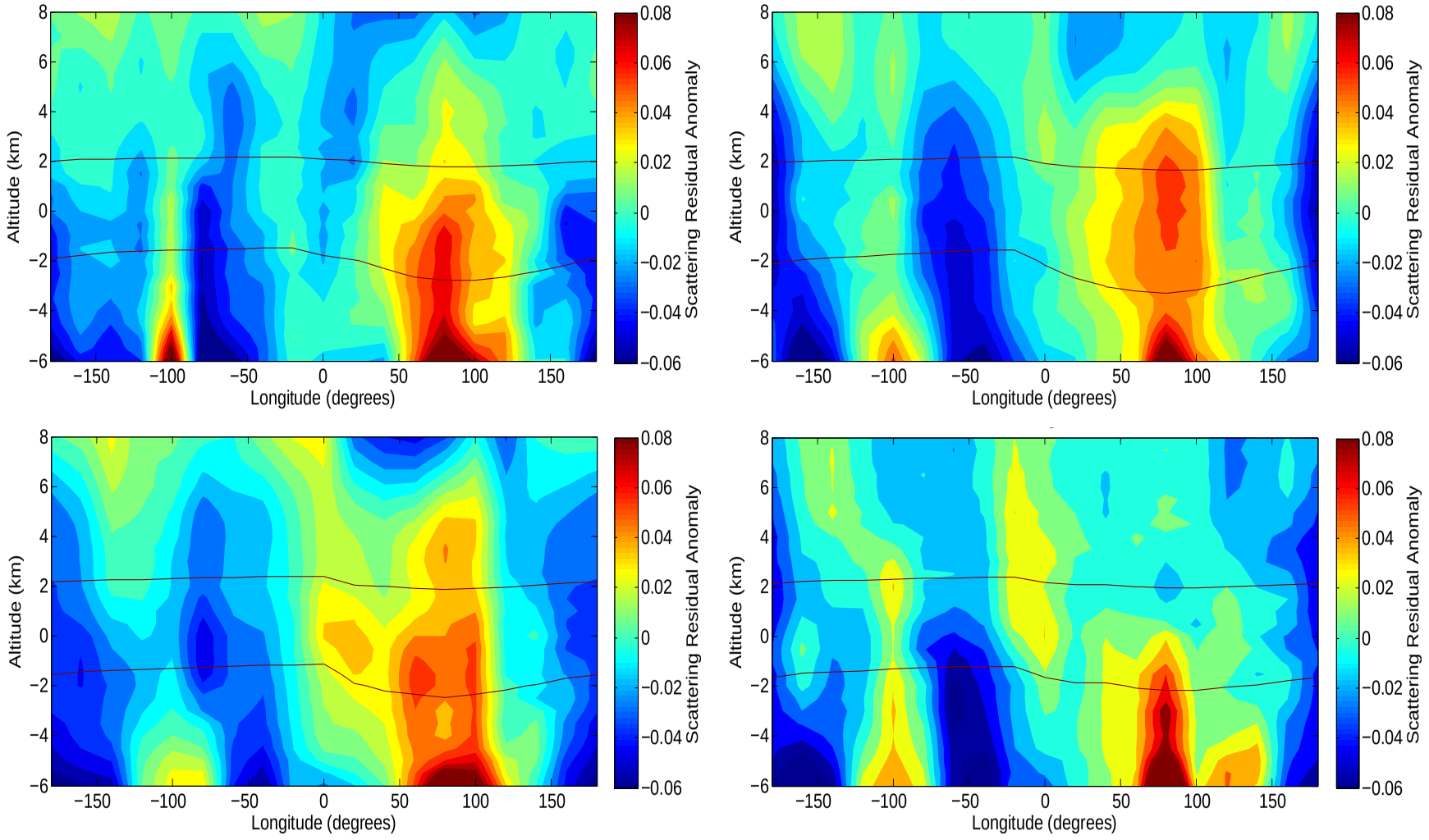

Figure 4.11: Anomaly of the mean cloud-free scattering residual longitudinal cross sections between 15° and 45° latitude for July and August 2006, 2007, 2008, and 2009 using OSIRIS limb scattered radiance profiles measured on the descending track of Odin's orbit at 800 nm. These are the yearly equivalent to Figure 4.10(c), which show the anomaly of the cloud-free scans. The mean potential temperature levels at 380 and 420 K are plotted in solid dark red. The vertical axis is shown with respect to the local tropopause; negative values correspond to altitudes below the tropopause level.

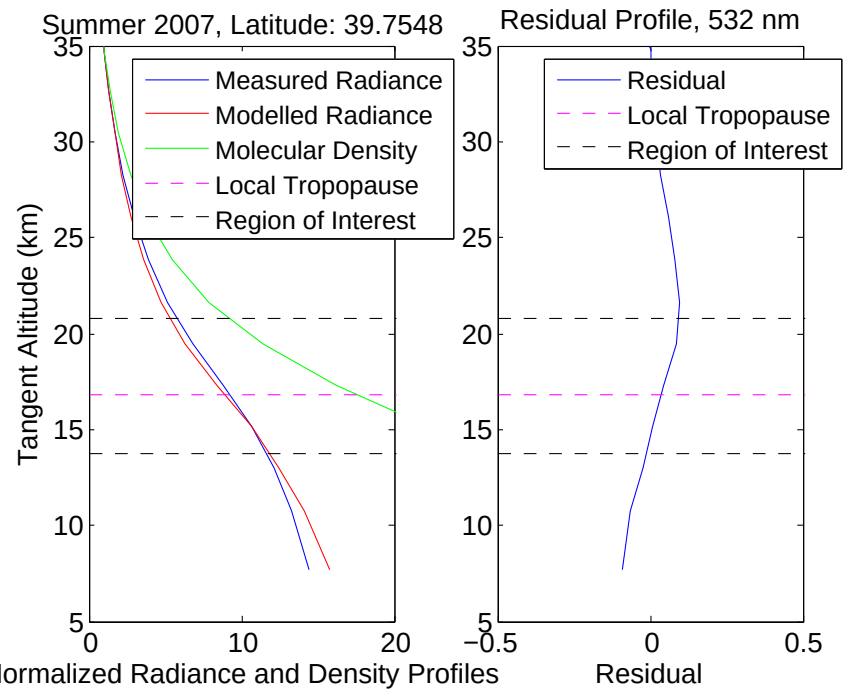

Figure 4.12: Normalized radiance, density, and residual profiles as a function of tangent altitude at 532 nm.

Although these results at 800 nm are encouraging, it is important to consider results obtained at the same wavelength used by *Vernier et al.* (2011), namely at 532 nm, and also results derived from alternative viewing geometries. The work described above was repeated using OSIRIS measurements during the descending track of Odin's orbit at 532 nm, which is the wavelength measured by CALIPSO. Here, the radiance profile in the left-hand plot of Figure 4.12 shows signs that the atmosphere is optically thick at 532 nm down to the troposphere. Radiance profiles modelled in an aerosol- and cloud-free atmosphere were obtained from the SASKTRAN radiative transfer model. The radiance measured at 532 nm by OSIRIS is plotted in blue, the radiance modelled at 532 nm by SASKTRAN is plotted in red, and the molecular density is plotted in green for reference. The 532 nm radiance profiles is attenuated down to the tropospheric level since it falls below the molecular density radiance profile. This implies the optically thin atmosphere approximation no longer holds. Clouds occurring at altitudes lower than the altitude where the atmosphere becomes optically thick are not distinguishable because the atmosphere becomes too thick to detect them. As a result, the residual profile is essentially zero and does not show the presence of clouds. As the cloud detection technique in Chapter 3 depends on the residual profile's ability to characterize the presence of clouds, a proper analysis at 532 nm was not possible with the given data set.

The same analysis conducted with OSIRIS data at 800 nm was repeated, but with a different viewing geometry; the solar scattering angle, Θ, of the scans was changed by using measurements taken during the ascending track of Odin's orbit. During the ascending track, the solar scattering angle is closer to 60° while on the descending track, the solar scattering angle is near 120°; refer to Figure 2.9. Also, measurements taken on the ascending track occur around 1800 h local time. This analysis was performed separately from the descending node scans as the change in scattering angle changes the magnitude of the scattering ratio PDFs.

One striking difference between the mean cloud containing R longitudinal cross sections of the descending and ascending tracks, that is between Figures 4.10(a) and 4.13(a), respectively, is the lack of a cloud high over the Asian monsoon sector in Figure 4.13(a). Since the solar scattering angle during the ascending track is closer to the forward scattering scenario, clouds appear very bright causing some of the pixels on the instrument to saturate. Scans measured with saturated pixels were rejected. Thus, many of the cloud-containing scans were immediately rejected due to an excessively bright signal and hence are not included in the figure.

Figure 4.13(b) for the ascending node is comparable to Figure 4.10(b) and represents the mean cloud-free R longitudinal cross section. However, rather than excluding all the cloudy scans, clouds were removed by truncating the profile downward from the altitude of the detected cloud. Therefore, more accurately, Figure 4.13(b) shows all ascending node scans falling within the latitudinal region of interest while neglecting portions of scans containing clouds. This alternative approach is used because, otherwise, there are too few ascending node scans available to produce a representative figure. Due to Odin's orbit, fewer scans were available on the ascending track because the northern hemisphere was in darkness at the ascending node local time. Notice how the colour scales in Figures 4.13(a) and 4.13(b) are identical and how the details within the stratospheric aerosol layer are the same yet the cloud maxima are removed within the troposphere.

Finally, the anomaly of Figure 4.13(b) was computed and is shown in Figure 4.13(c). In these results, the presence of an ATAL is unclear. The lack of a strong ATAL at the tropopause level above the Asian monsoon region suggests the aerosol layer experiences a diurnal cycle as traces of the ATAL are seen in the early morning and not in the evening; the ATAL is visible in Figure 4.10(c) during the descending track, namely at 0600 h, and is not present in Figure 4.13(c) during the ascending track, at 1800h.

Laaksonen et al. (2000) present interesting work on the formation of cloud condensation nuclei from sulfur dioxide, SO_2, which provides a possible explanation for the sulfuric origin of the ATAL.

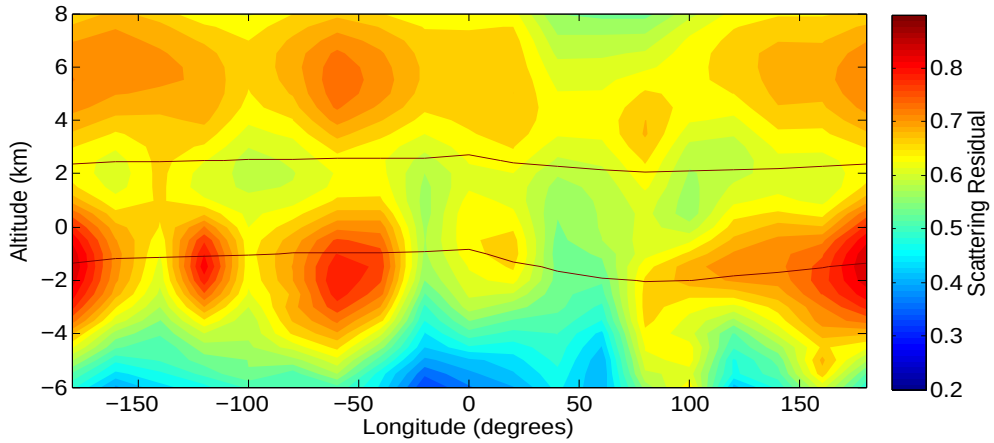

(a) All scans

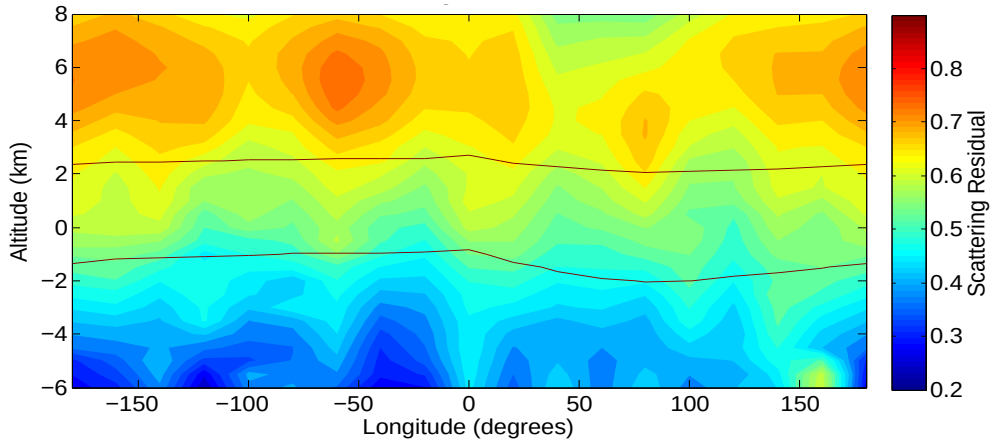

(b) Cloud-free scans

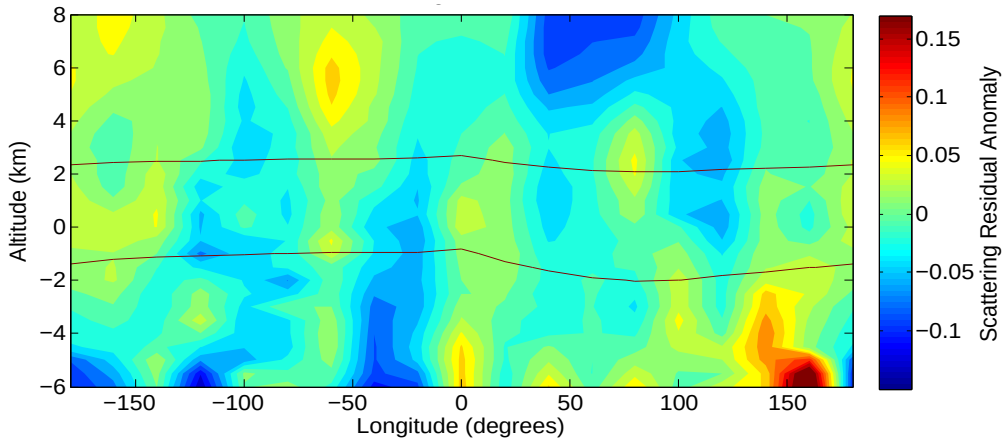

(c) Anomaly of cloud-free scans

Figure 4.13: The mean scattering residual longitudinal cross section between 15° and 45° latitude for July and August 2006 and 2007 using OSIRIS limb scattered radiance profiles measured on the ascending track of Odin's orbit at 800 nm; (a) all scans, (b) cloud-free scans, and (c) anomaly of cloud-free scans. The mean potential temperature levels at 380 and 420 K are plotted in solid dark red. The vertical axis is shown with respect to the local tropopause; negative values correspond to altitudes below the tropopause level.

The meteorological, chemical, and microphysical states of the upper troposphere make this altitude ideal for the formation of new particles. Photochemical reactions occur with relatively strong intensity, low temperatures encourage condensation, and homogeneous nucleations accumulate as a result of high supersaturation and low concentration of condensational sinks (*Laaksonen et al.*, 2000).

Stratospheric aerosols are primarily sulfuric-based (*Junge et al.*, 1961; *Turco et al.*, 1979, 1982). Gaseous sulfuric acid, H_2SO_4, results from a series of chemical reactions initially involving sulfur dioxide:

$$SO_2 + OH + M \rightarrow HSO_3 + M \tag{4.1}$$

$$HSO_3 + O_2 \rightarrow SO_3 + HO_2 \tag{4.2}$$

$$SO_3 + H_2O + M \rightarrow H_2SO_4 + M \tag{4.3}$$

The occurrence of the first reaction is regulated by hydroxyl, OH, because it is photochemically produced.

According to the model in *Laaksonen et al.* (2000), H_2SO_4 is produced as of 0700 h local time once the OH molecules are available and its concentration reaches a maximum around 1300 h. Come evening, the production of H_2SO_4 ceases as the OH radicals are no longer abundant. Due to nucleation and coagulation, the concentration of gaseous sulfuric acid falls to zero as the particle size of sulfuric aerosol increases. The nighttime concentration of gaseous H_2SO_4 is four orders of magnitude smaller than afternoon concentrations. Over time, the particles grow by bonding to water molecules. The newly formed H_2SO_4 droplets are of suitable size to act as cloud condensation nuclei (*Laaksonen et al.*, 2000).

During the OSIRIS ascending node measurement at 1800 h, the sulfuric aerosol mean radius is less than 3 nm since it has not had sufficient time to grow. Referring back to Section 2.4.1, the size parameter, $x \equiv \frac{2\pi a}{\lambda}$, of such particles falls within the Rayleigh scattering regime at 800 nm, where a and λ are the particle radius and wavelength, respectively, and the aerosols are washed into the molecular background distribution. However, during the OSIRIS descending node measurements at 0600 h, the particles have coagulated and grown such that the mean radius falls well within the Mie scattering regime. Once the droplets are large enough to assume the role of cloud condensation nuclei, they form cirrus clouds and fall within the cloudy condition in the cloud detection technique. Therefore, based on the observed diurnal cycle, speculations that the ATAL can possibly be composed of coagulated sulfuric aerosol are plausible.

4.3 Volcanic Plume Tracking

Volcano eruptions with a Volcanic Explosivity Index (VEI) greater than 4 or 5 have the potential to inject volcanic mass, such as sulfur dioxide, SO_2, into the upper troposphere and lower stratosphere. According to *Newhall and Self* (1982), eruptions with VEI 4 and 5 have *definite* and *significant* injections into the stratosphere, respectively. Within the last 50 years, the largest three eruptions are Agung in 1963 on the West coast of Bali, Indonesia with VEI 5, El Chichón in 1982 in Chiapas, Mexico with VEI 5, and Mount Pinatubo in 1991 in Luzon, Philippines with VEI 6 (*Haywood et al.*, 2010), although *Newhall and Self* (1982) include Mount St. Helen in 1980 in Washington, United States with VEI 5 as a fourth.

Robock (2000) presents a comprehensive overview of the climate response to volcanic eruptions. The most abundant gases released during an eruption are water vapour, H_2O, carbon dioxide, CO_2, nitrogen gas, N_2, and sulfuric species. Sulfur gases, such as sulfur dioxide, SO_2, are injected into the atmosphere and are converted into sulfuric aerosol, namely H_2SO_4, through oxidation; refer to Reactions 4.1, 4.2, 4.3 (*Stockwell and Calvert*, 1983; *Margitan*, 1984; *Pinto et al.*, 1989; *Zhao et al.*, 1995; *SPARC*, 2006). The atmospheric lifetimes of volcanic gaseous species from smaller eruptions leading to tropospheric injections are about a week and the climatic response is insipid (*Seinfeld and Pandis*, 2006). Stratospheric e-folding residency times for larger eruptions are roughly a year (*Budyko*, 1977; *Stenchikov et al.*, 1998; *Robock*, 2000; *Gao et al.*, 2007) and the subsequent climate effects can be substantial and last for multiple years (*Robock*, 2000). Aerosol clouds tend to cool the surface of the Earth and the troposphere by increasing albedo and reflectivity of shortwave solar radiation to space, which inevitably heats the stratosphere through the absorption of both solar and terrestrial radiation. Detectable climatic responses vary in intensity according to the geographical position of the volcano, the time of year and magnitude of the eruption, seasonal fluctuations in isolation patterns, and the deposition rates of sulfuric species (*Kravitz and Robock*, 2011). Tropical eruptions lead to larger heating in the tropics than at higher latitudes, which manifests a pole-to-equator temperature gradient (*Robock*, 2000). Furthermore, aerosol clouds provide surfaces whereupon heterogeneous chemical reactions occur and lead to the destruction of stratospheric ozone. Consequently, ultraviolet absorption is reduced as well as lower stratospheric heating.

Volcanic eruptions have repercussions on more than just climate and temperature; aviation is also impacted. Volcanic ash can damage navigation systems, clog sensors, restrict the pilot's view,

scratch the surface of the aircraft, and cause the engines to stall due to melted ash within (*Van Geffen et al.*, 2007). However, although ash and dust are the primary hazards to aviation, SO_2 also poses a risk. Sulfur dioxide leads to the production of sulfuric acid, which is corrosive and damages the aircraft surface and windows. Sulfate deposits within the engines block cooling holes and cause overheating (*Bernard and Rose*, 1990; *Casadevall et al.*, 1996). The SO_2 cloud need not strictly be contained in the ash cloud. Generally, ash descends due to gravity faster than sulfur dioxide, so a separation between the ash and SO_2 clouds is not uncommon at some distance from the eruption source (*Van Geffen et al.*, 2007). Unfortunately, winds disperse the volcanic plume over long distances and transport it to the jet streams wherein it is exposed to aircrafts, which use the jet streams to reduce fuel consumptions and flight duration (*Rix et al.*, 2009).

The simplest and safest way to mitigate hazards to aviation is to avoid flying near or through the plume. Since onboard sensors cannot detect micron-size particles and because SO_2 is colourless, satellite tracking is a potential solution. Sulfur dioxide is a reliable indicator of volcanic activity. The Support to Aviation Control Services is a service based on satellite SO_2 measurements with purpose to track volcanic eruptions and plumes in near-real time and to convey such information to the Volcanic Ash Advisory Centers (VAACs). The VAACs then advise airlines to reroute or cancel flights and issue alerts of the potential dangers associated with volcanic plumes (*Van Geffen et al.*, 2007).

Cirrus clouds and volcanic plume particle sizes are roughly on the same order of magnitude, and both yield enhanced scattering signals when measured by OSIRIS. Hence, the scattering physics presented in Section 2.4 applies to volcanic aerosols. In the limb viewing geometry, an OSIRIS radiance profile will register the presence of volcanic aerosol through an enhanced scattered signal, much like the presence of cirrus clouds shown in Figure 3.1(b). Therefore, the cloud detection technique described in Chapter 3 is a convenient procedure that can be used to locate and track volcanic plumes.

The Sarychev volcano located at 48°N and 153°E in the Kuril Islands underwent a sequence of eruptions between 12 June to 19 June 2009. A small SO_2 plume was first detected by the Infrared Atmospheric Sounding Interferometer (IASI) alert system on 11 June, which foreshadowed future eruptions. Multiple small plumes totalling less than 0.1 Tg of SO_2 ensued until 15 June when the first large eruption estimated at 0.5 Tg of SO_2 occurred. A second large eruption was detected 16 June with an approximate emission of 0.7 Tg of SO_2 for a total emission of 1.2 ± 0.2 Tg of SO_2 into the lower stratosphere (*Haywood et al.*, 2010). The 2009 Sarychev eruption ranks among the

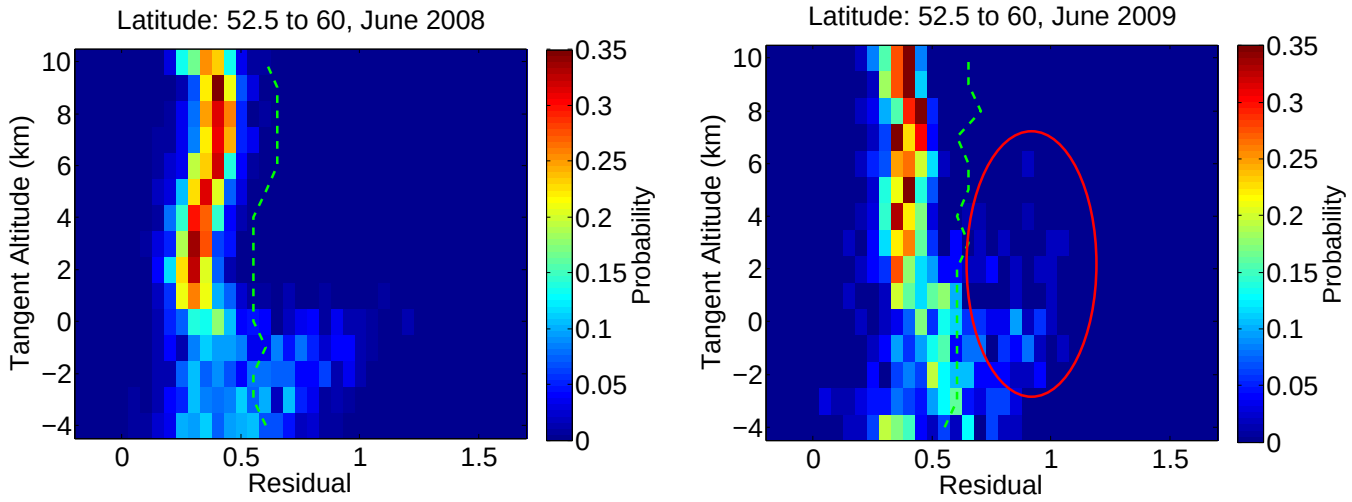

Figure 4.14: Two-dimensional residual probability density function with the cloud-free threshold curve for scans within the 52.5° to 60°N latitudinal band during June 2008 (left) and 2009 (right) at 800 nm. Traces of stratospheric-penetrating volcanic aerosols are present in 2009 and are circled in red. The vertical axis is shown with respect to the local tropopause; negative values correspond to altitudes below the tropopause level.

top ten largest stratospheric injections within the last half a century.

The cloud detection technique was applied to OSIRIS measurements taken in the northern hemisphere during the month of June 2008 and 2009. Shown in Figure 4.14, the residual probability density functions for the 52.5°N to 60°N latitudinal band compares the 2008 volcano-free scenario to that of 2009 when Sarychev erupted. The vertical axis is shown with respect to the local tropopause. The respective cloud-free threshold lines are overlayed and outline the distinction between the cloud-free background molecular and the cloudy or volcanic aerosol conditions; the cloud-free and cloudy conditions occur in the distributions to the left and to the right of the lines, respectively. In June 2009, the upper atmosphere was heavily infused with volcanic aerosol, especially ash, dust, and sulfur dioxide and its presence is circled in red. Notice how this aerosol is detected well within the stratosphere. At this time, the majority of the SO_2 has not yet been oxidized into sulfuric aerosol, so the detected stratospheric aerosol consists mainly of ash and dust.

Figure 4.15 shows the cloud top height with respect to the local tropopause for three weeks in June for the years 2008 and 2009. Wherever a cloud or volcanic aerosol was detected, the altitude and geographical location were noted. The altitude colour scale is in kilometers and is measured with respect to the local tropopause level, so hot colours correspond to levels within the stratosphere.

In 2008 when volcanic activity was minimal, the cloud top heights do not vary greatly and occur at most a few kilometers above the local tropopause. At high latitudes, cloud tops occur at higher relative altitudes compared to those in the tropics because the tropopause level falls in altitude as latitude increases, refer to Figure 4.1. In 2009, however, the volcanic plume is clearly seen within the stratosphere as well as its westward dispersion over time. In both years, the apparent lack of cloud top detections around 30°N latitude is not surprising as this aligns with the edge of the Hadley cell and the downwelling branch of the circulation.

Using IASI measurements, *Haywood et al.* (2010) track the SO_2 plume emitted from the 2009 Sarychev volcanic eruption to estimate the amount of sulfur dioxide injected into the upper atmosphere. IASI consists of a Fourier transform spectrometer onboard the MetOp-A satellite, which was launched October 2006 into a polar sun-synchronous orbit. This nadir-viewing instrument provides thermal outgoing radiation measurements of the Earth between 645 and 2760 cm^{-1} on a global basis twice a day with a footprint of 12 km diameter and a swath width of 2200 km. IASI has a high spectral resolution of 0.5 cm^{-1} and a spectral sampling of 0.25 cm^{-1}. The instrument's primary mission concerns meteorological applications, however its spatial coverage proves convenient for measuring a variety of atmospheric species (*Clerbaux et al.*, 2009), most notably for detecting and tracking SO_2 (*Clarisse et al.*, 2008, 2010).

In Figure 4.16, the concentration of sulfuric dioxide is measured in Dobson units (DU) where 1 DU corresponds to a 10 μm thick SO_2 layer at standard temperature and pressure. That is, 1 DU is approximately equal to 0.0285 g of SO_2 per square meter. The cloud top diffusion in Figure 4.15 and the SO_2 plume dispersion in Figure 4.16 can be compared because the volcanic ash plume and the SO_2 cloud dispersion rates are roughly on the same order of magnitude. Both figures show the plume evolving westward and remaining at middle to high latitudes. This demonstrates the potential to use limb scatter measurements to perform altitude resolved tracking of early ash plumes from volcanic eruptions.

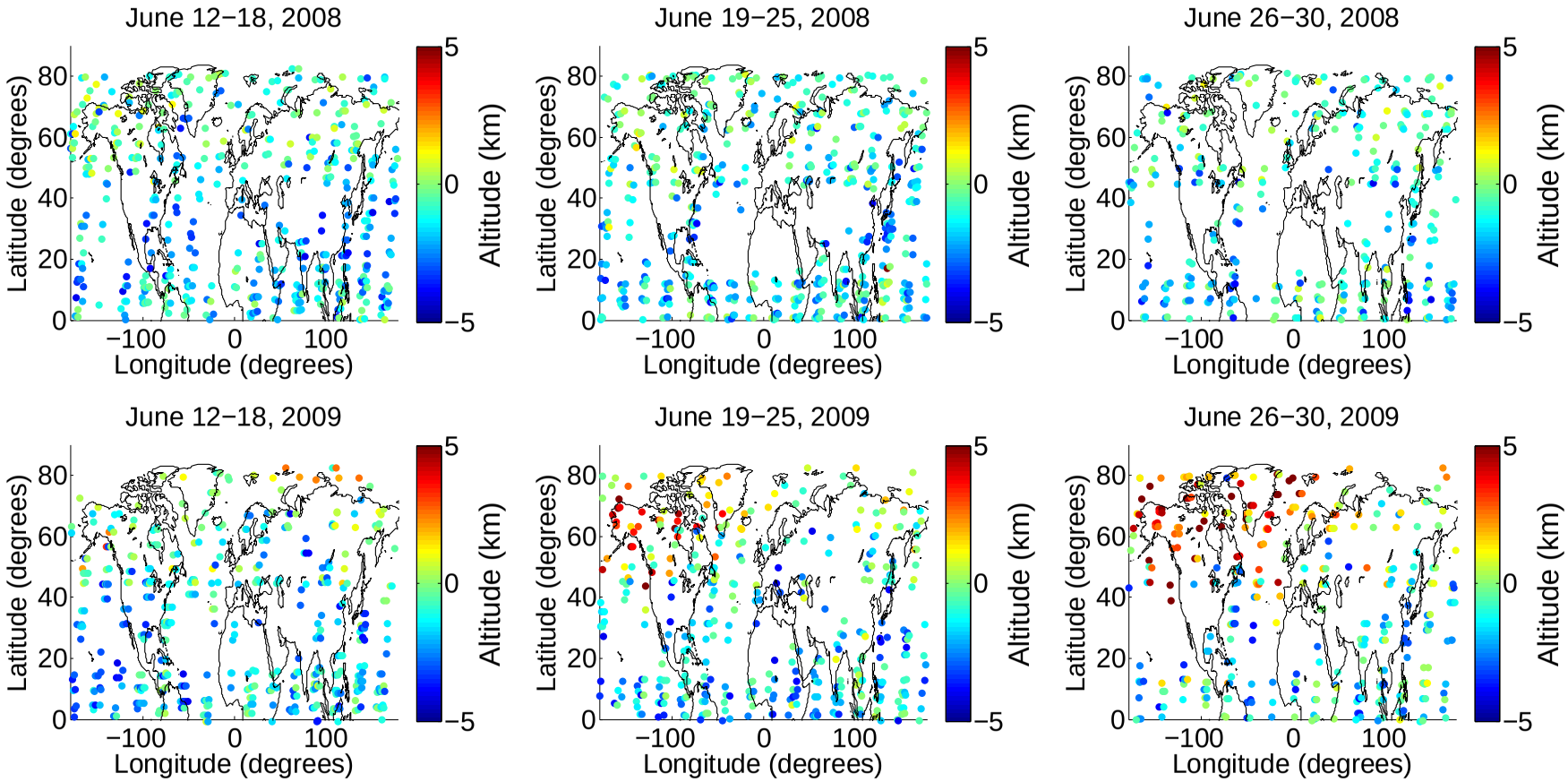

Figure 4.15: Cloud top height with respect to the local tropopause for three consecutive weeks following the Sarychev volcano eruption on 12 June 2009 (bottom row) and, for comparison, the same weeks one year before the eruption (top row). The colour scale is in kilometers relative to the local tropopause where negative values correspond to altitudes below the tropopause level.

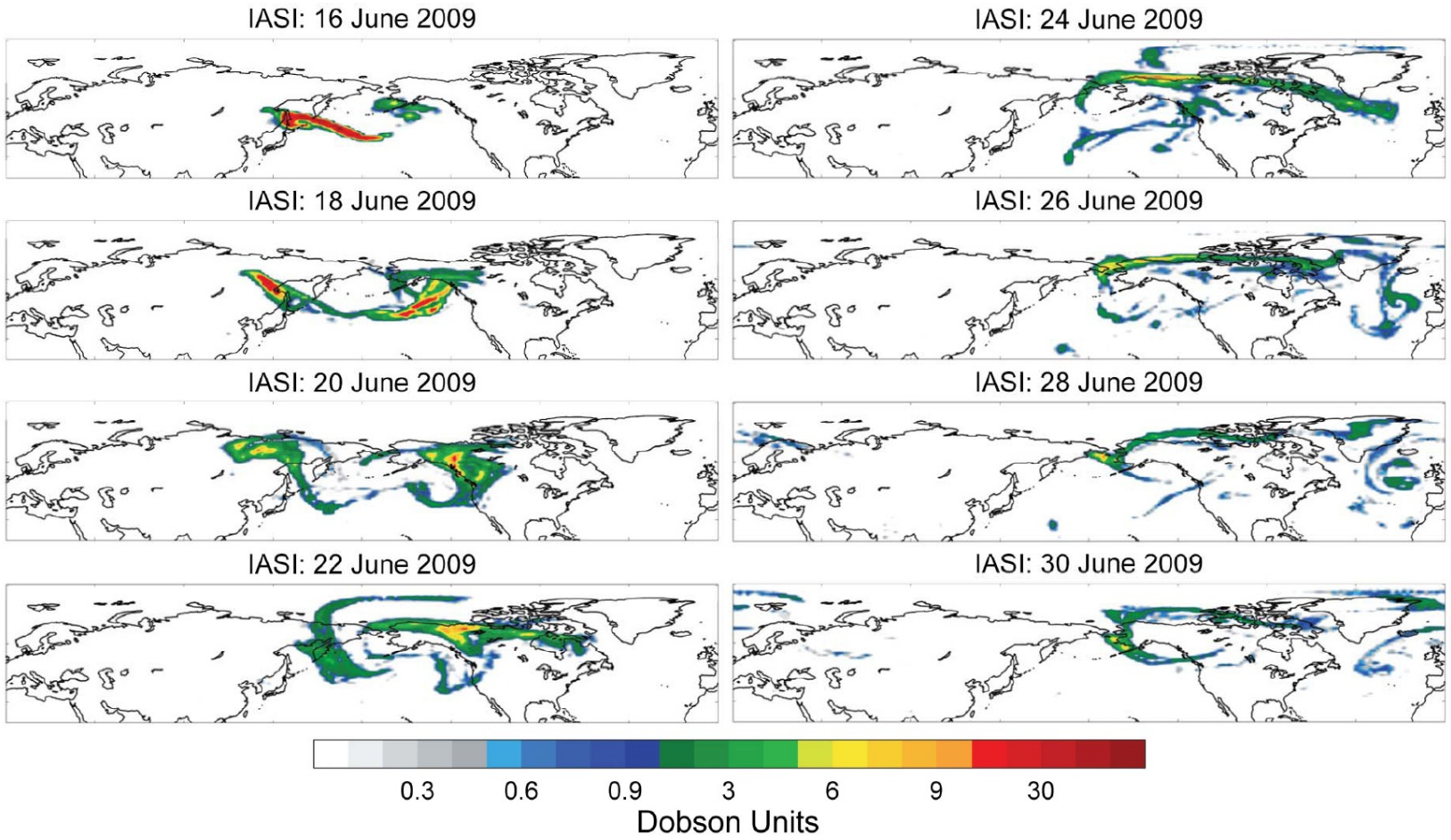

Figure 4.16: The evolution of the SO_2 plume emitted from the Sarychev volcano eruption as measured by ISAI in Dobson units between 16 June to 30 June 2009; extracted from *Haywood et al.* (2010) and reproduced by permission of American Geophysical Union.

Chapter 5

Summary and Conclusions

Through the development of aeronomy and remote sensing techniques, quantitative and qualitative measurements of atmospheric signatures on a global basis are now possible. The limb scattering technique relies on measurements of scattered sunlight that carry information of atmospheric composition. As light is scattered through the Earth's limb, the atmosphere filters parts of the electromagnetic spectrum creating absorption features in the resulting signature. OSIRIS employs the limb scattering technique and measures the radiance of the atmosphere to infer information on the distribution of ozone, nitrogen dioxide, and aerosols within the stratosphere. Although clouds are not measured directly, OSIRIS measurements are used in the development of a high altitude cloud detection technique.

The efficiency and reliability of the cloud detection technique depends on the residual profile's ability to characterize the occurrence of clouds. The scattering residual is computed as the logarithmic difference between the measured radiance profile at 800 nm where the atmosphere is optically thin down to tropospheric altitudes and the modelled molecular radiance profile. The logarithmic difference is used rather than a straight difference as to avoid biasing scattering enhancements at lower tangent altitudes. PDFs are produced from the scattering residual profiles for separate latitudinal bands on a monthly basis. Because the solar scattering angle changes over the course of a year, the variation in the amplitude of the measured radiance signal causes a shift in the PDF distribution along the residual axis. Thus, producing separate time resolved PDFs prevents blurring distributions.

The PDFs reveal the scattering residual distribution is not a continuum measurement. The ability to distinguish the cloudy and cloud-free conditions is key to the success of the technique. A Gaussian curve is fitted to the cloud-free distribution and its standard deviation is computed. Threshold residual lines are drawn as a function of altitude two standard deviations to the right of the cloud-free range along the residual axis and delimit the occurrence of clouds. By overlaying these threshold lines onto the residual profiles, the presence of a cloud within the altitude region of

interest can be determined.

A useful application of the cloud detection technique is to produce probability maps showing the distributions of cloud top occurrence frequencies. Cloud top maxima were found over Central America and over Indonesia as these correspond to highly convective regions. The average global seasonal cirrus cloud coverage as measured by CALIPSO reported in *Sassen et al.* (2008) and by SAGE II reported in *Wang et al.* (1996) were compared to the global seasonal cloud top occurrence frequency distributions measured by OSIRIS. CALIPSO and SAGE II are nadir viewing and solar occultation instruments, respectively. The comparisons reveal good agreement and the north-south shift of the ITCZ is fairly apparent.

Fueglistaler et al. (2009) showed profiles of the mean cloud occurrence frequency versus altitude in the tropics as measured by CALIPSO and SAGE II and theorized the inconsistency between the profiles is a result of the different viewing geometries and optical depth thresholds of the instruments. For comparison, the cloud detection technique was used to plot the cloud top occurrence frequency versus altitude profiles derived from OSIRIS measurements for tropical and mid-latitude regions. The shape of the tropical profiles compared relatively well with the analogous cirrus cloud profile from SAGE II, which is an encouraging result because SAGE II and OSIRIS have similar viewing geometries. This agreement supports the theory presented in *Fueglistaler et al.* (2009).

The interchange between the transport of air and freeze-drying alters the water vapour distribution and can contribute to the hydration or dehydration of the lower stratosphere. Using CALIPSO measurements of cirrus clouds, *Dessler* (2009) made a fundamental connection between cloud occurrence, water vapour, and relative humidity distributions and, in an effort to show the effects of hydration and dehydration, compared the dominant Asian monsoon and North American convective regions. The high altitude cloud detection technique was used to map the zonal average cloud top fraction for both of these sectors using OSIRIS measurements in support of *Dessler* (2009). In the tropics, cloud occurrences are high and water vapour mixing ratio is low. Because relative humidity is high in regions of maximum cloud top occurrence, evaporation of ice ascended by convection is inhibited. In situ formation of clouds is stimulated leading to possible irreversible dehydration and consequently convection has little effect on the water vapour mixing ratio there. At mid-latitudes, both cloud occurrence and water vapour mixing ratio are high in regions of low relative humidity. Convection drives cloud ice into the stratosphere and, because of the low relative humidity, evaporates leading to an increase in water vapour. At mid-latitudes, the lower stratosphere is hydrated and clouds are correlated with convection.

Vernier et al. (2011) recently detected the presence of an ATAL using CALIPSO measurements. Scans with a mean volume depolarization ratio greater than 5% contained clouds and were removed from the analysis such that the remaining cloud-free scans were used to identify the ATAL. According to *Vernier et al.* (2011), the origin and nature of the aerosol layer are unclear, however its presence links deep convection with the transport of aerosols and their gaseous precursors into the upper atmosphere. In support of *Vernier et al.* (2011), the cloud detection technique was used to remove cloud-containing scans measured by OSIRIS. The computed anomaly of the mean cloud-free scattering residual longitudinal cross sections showed signs of an aerosol layer at the tropopause level over Asia for scans measured around 0600 h. Weak signs of an aerosol layer were present in the anomaly for measurements taken at 1800 h, which suggests the aerosol layer exhibits a diurnal cycle. *Laaksonen et al.* (2000) suggest stratospheric cloud condensation nuclei have sulfuric origin, which leads to speculations on the nature of the ATAL.

A practical application of the high altitude cloud detection technique is to monitor and track volcanic plumes to mitigate hazards to aviation. Although ash and dust are the primary hazards, sulfur dioxide and sulfuric aerosol also impose substantial risk because they damage the aircraft by leaving sulfur deposits inside the engines. Within the first month since the eruption, the sulfur dioxide plume travels in relatively close proximity with the ash and dust. Satellite measurements of sulfuric oxide and aerosol particles are useful to oversee the evolution of the plume. The cloud detection technique was employed to track the dispersion of the volcanic plume across the northern hemisphere following the Sarychev eruption on 12 June 2009. OSIRIS measurements provide information on the geographic location as well as the height profile of volcanic aerosols.

The applications and use of the cloud detection technique have not been exhausted in this work. Future work includes integrating the high altitude cloud detection technique in the OSIRIS operational retrievals. Since complex radiative transfer is required to accurately model scattering through optically thick layers of atmosphere or clouds, the cloud detection technique can be used to identify the presence of clouds as well as the cloud top altitude within the scans. Furthermore, the cloud detection technique can be employed to study trends in the background aerosol loading of the atmosphere as suggested by *Solomon et al.* (2011), the evolution of cloud top occurrence frequencies and distributions, and detecting polar stratospheric clouds at high southern latitudes during austral spring. A study using the technique would be useful in understanding the intricate involvement cirrus clouds have with the climate system and the radiative budget of the atmosphere since, at present, they remain unsolved.

Bibliography

Alcala, C. M., and A. E. Dessler (2002), Observations of deep convection in the tropics using the Tropical Rainfall Measuring Mission (TRMM) precipitation radar, *J. Geophys. Res.*, *107*, 4792, doi:10.1029/2002JD002457.

Bernard, A., and W. I. Rose (1990), The injection of sulfuric acid aerosols in the stratosphere by the el chichon volcano and its related hazards to the international air traffic, *Nat. Hazards*, *3*, 59–67, doi:10.1007/BF00144974.

Bernath, P. F., C. T. McElroy, M. C. Abrams, C. D. Boone, M. Butler, C. Camy-Peyret, M. Carleer, C. Clerbaux, P.-F. Coheur, R. Colin, P. DeCola, M. DeMazière, J. R. Drummond, D. Dufour, W. F. J. Evans, H. Fast, D. Fussen, K. Gilbert, D. E. Jennings, E. J. Llewellyn, R. P. Lowe, E. Mahieu, J. C. McConnell, M. McHugh, S. D. McLeod, R. Michaud, C. Midwinter, R. Nassar, F. Nichitiu, C. Nowlan, C. P. Rinsland, Y. J. Rochon, N. Rowlands, K. Semeniuk, P. Simon, R. Skelton, J. J. Sloan, M.-A. Soucy, K. Strong, P. Tremblay, D. Turnbull, K. A. Walker, I. Walkty, D. A. Wardle, V. Wehrle, R. Zander, and J. Zou (2005), Atmospheric Chemistry Experiment (ACE): Mission overview, *Geophys. Res. Lett.*, *32*, L15S01, doi:10.1029/2005GL022386.

Bourassa, A. (2007), Stratospheric aerosol retrieval from OSIRIS limb scattered sunlight spectra, Ph.D. thesis, University of Saskatchewan.

Bourassa, A. E., D. A. Degenstein, R. L. Gattinger, and E. J. Llewellyn (2007), Stratospheric aerosol retrieval with OSIRIS limb scatter measurements, *J. Geophys. Res.*, *112*, D10,217, doi:10.1029/2006JD008079.

Bourassa, A. E., D. A. Degenstein, and E. J. Llewellyn (2008), SASKTRAN: A spherical geometry radiative transfer code for efficient estimation of limb scattered sunlight, *J. Quant. Spectros. Radiat. Trans.*, *109*, 52–73, doi:10.1016/j.jqsrt.2007.07.007.

Brewer, A. W. (1949), Evidence for a world circulation provided by the measurements of helium and water vapour distribution in the stratosphere, *Quart. J. Roy. Meteor. Soc.*, *75*, 351–363, doi:10.1002/qj.49707532603.

Budyko, M. I. (1977), *Climate Changes*, AGU, Washington, D. C.

Casadevall, T. J., P. J. Delos Reyes, and D. J. Schneider (1996), The 1991 pinatubo eruptions and their effects on aircraft operations, *Fire and Mud: Eruptions and Lahars of Mount Pinatubo, Phillipines*, edited by C. G. Newhall and R. S. Punongbayan, 1071–1088, Univ Washington Press.

Chahine, M. T. (1992), The hydrological cycle and its influence on climate, *Nature*, *359*, 373–380, doi:10.1038/359373a0.

Chen, P., and W. A. Robinson (1992), Propagation of planetary waves between the troposphere and stratosphere, *J. Atmos. Sci.*, *49*, 2533–2545, doi:10.1175/1520-0469(1992)049<2533:POPWBT>2.0.CO;2.

Clarisse, L., P. F. Coheur, A. J. Prata, D. Hurtmans, A. Razavi, T. Phulpin, J. Hadji-Lazaro, and C. Clerbaux (2008), Tracking and quantifying volcanic SO_2 with IASI, the September 2007 eruption at Jebel at Tair, *Atmos. Chem. Phys.*, *8*, 16,917–16,949.

Clarisse, L., D. Hurtmans, A. J. Prata, F. Karagulian, C. Clerbaux, M. de Mazière, and P.-F. Coheur (2010), Retrieving radius, concentration, optical depth, and mass of different types of aerosols from high-resolution infrared nadir spectra, *App. Opt.*, *49*, 3713, doi:10.1364/AO.49.003713.

Clerbaux, C., A. Boynard, L. Clarisse, M. George, J. Hadji-Lazaro, H. Herbin, D. Hurtmans, M. Pommier, A. Razavi, S. Turquety, C. Wespes, and P.-F. Coheur (2009), Monitoring of atmospheric composition using the thermal infrared IASI/MetOp sounder, *Atmos. Chem. Phys.*, *9*, 8307–8339.

Corti, T., B. P. Luo, Q. Fu, H. Vömel, and T. Peter (2006), The impact of cirrus clouds on tropical troposphere-to-stratosphere transport, *Atmos. Chem. Phys.*, *6*, 2539–2547.

Corti, T., B. P. Luo, M. de Reus, D. Brunner, F. Cairo, M. J. Mahoney, G. Martucci, R. Matthey, V. Mitev, F. H. dos Santos, C. Schiller, G. Shur, N. M. Sitnikov, N. Spelten, H. J. Vössing, S. Borrmann, and T. Peter (2008), Unprecedented evidence for deep convection hydrating the tropical stratosphere, *Geophys. Res. Lett.*, *35*, L10810, doi:10.1029/2008GL033641.

de F. Forster, P. M., and K. P. Shine (1999), Stratospheric water vapor changes as a possible contributor to observed stratospheric cooling, *Geophys. Res. Lett.*, *26*, 3309–3312, doi: 10.1029/1999GL010487.

Degenstein, D. A., E. J. Llewellyn, and N. D. Lloyd (2003), Volume emission rate tomography from a satellite platform, *Appl. Opt.*, *42*, 1441–1450, doi:10.1364/AO.42.001441.

Degenstein, D. A., E. J. Llewellyn, and N. D. Lloyd (2004), Tomographic retrieval of the oxygen infrared atmospheric band with the OSIRIS infrared imager, *Can. J. Phys.*, *82*, 501–515, doi: 10.1139/p04-024.

Dessler, A. E. (2002), The effect of deep, tropical convection on the tropical tropopause layer, *J. Geophys. Res.*, *107*, 4033, doi:10.1029/2001JD000511.

Dessler, A. E. (2009), Clouds and water vapor in the northern hemisphere summertime stratosphere, *J. Geophys. Res.*, *114*, D00H09, doi:10.1029/2009JD012075, Copyright 2009 American Geophysical Union.

Dessler, A. E., and K. Minschwaner (2007), An analysis of the regulation of tropical tropospheric water vapor, *J. Geophys. Res.*, *112*, D10120, doi:10.1029/2006JD007683.

Dessler, A. E., and S. C. Sherwood (2004), Effect of convection on the summertime extratropical lower stratosphere, *J. Geophys. Res.*, *109*, D23,301, doi:10.1029/2004JD005209.

Dessler, A. E., and P. Yang (2003), The distribution of tropical thin cirrus clouds inferred from terra MODIS data, *J. Clim.*, *16*, 1241–1247, doi:10.1175/1520-0442(2003)16<1241:TDOTTC>2.0.CO;2.

Dunkerton, T. J. (1995), Evidence of meridional motion in the summer lower stratosphere adjacent to monsoon regions, *J. Geophys. Res.*, *100*, 16,675–16,688, doi:10.1029/95JD01263.

Ertel, H. (1942), Ein neuer hydrodynamischer wirbelsatz, *Met. Z.*, *59*, 271–281.

Eyring, V., T. Shepherd, and D. Waugh (Eds.) (2010), *Chemistry-Climate Model Validation*, Report No. 5, Stratosphere-Troposphere Processes and their Role in Climate.

Fischer, H., M. de Reus, M. Traub, J. Williams, J. Lelieveld, J. de Gouw, C. Warneke, H. Schlager, A. Minikin, R. Scheele, and P. Siegmund (2003), Deep convective injection of boundary layer air into the lowermost stratosphere at midlatitudes, *Atmos. Chem. Phys.*, *3*, 739–745.

Flury, T., D. L. Wu, and W. G. Read (2012), Correlation among cirrus ice content, water vapor and temperature in the TTL as observed by CALIPSO and Aura/MLS, *Atmos. Chem. Phys.*, *12*, 683–691, doi:10.5194/acp-12-683-2012.

Fromm, M., J. Alfred, K. Hoppel, J. Hornstein, R. Bevilacqua, E. Shettle, R. Servranckx, Z. Li, and B. Stocks (2000), Observations of boreal forest fire smoke in the stratosphere by POAM III, SAGE II, and lidar in 1998, *Geophys. Res. Lett.*, *27*, 1407, doi:10.1029/1999GL011200.

Fromm, M. D., and R. Servranckx (2003), Transport of forest fire smoke above the tropopause by supercell convection, *Geophys. Res. Lett.*, *30*, 1542, doi:10.1029/2002GL016820.

Fu, Q., Y. Hu, and Q. Yang (2007), Identifying the top of the tropical tropopause layer from vertical mass flux analysis and CALIPSO lidar cloud observations, *Geophys. Res. Lett.*, *34*, L14813, doi: 10.1029/2007GL030099.

Fueglistaler, S., A. E. Dessler, T. J. Dunkerton, I. Folkins, Q. Fu, and P. W. Mote (2009), Tropical tropopause layer, *Rev. Geophys.*, *47*, doi:10.1029/2008RG000267, Copyright 2009 American Geophysical Union.

Gao, C., L. Oman, A. Robock, and G. L. Stenchikov (2007), Atmospheric volcanic loading derived from bipolar ice cores: Accounting for the spatial distribution of volcanic deposition, *J. Geophys. Res.*, *112*, D09109, doi:10.1029/2006JD007461.

Gates, W. L. (1961), Static stability measures in the atmosphere, *J. Atmos. Sci.*, *18*, 526–533, doi:10.1175/1520-0469(1961)018<0526:SSMITA>2.0.CO;2.

Gettelman, A., M. L. Salby, and F. Sassi (2002), Distribution and influence of convection in the tropical tropopause region, *J. Geophys. Res.*, *107*, 4080, doi:10.1029/2001JD001048.

Gettelman, A., P. M. F. Forster, M. Fujiwara, Q. Fu, H. Vomel, L. K. Gohar, C. Johanson, and M. Ammeraman (2004), The radiation balance of the tropical tropopause layer, *J. Geophys. Res.*, *109*, doi:10.1029/2003JD004190.

Gettelman, A., P. Hoor, L. L. Pan, W. J. Randel, M. I. Hegglin, and T. Birner (2011), The extratropical upper troposphere and lower stratosphere, *Rev. Geophys.*, *49*, doi:10.1029/2011RG000355.

Grosvenor, D. P., T. W. Choularton, H. Coe, and G. Held (2007), A study of the effect of overshooting deep convection on the water content of the TTL and lower stratosphere from Cloud Resolving Model simulations, *Atmos. Chem. Phys.*, *7*, 4977–5002.

Hartmann, D. L., and D. A. Short (1980), On the use of earth radiation budget statistics for studies of clouds and climate, *J. Atmos. Sci.*, *37*, 1233–1250, doi:10.1175/1520-0469(1980)037<1233:OTUOER>2.0.CO;2.

Hartmann, D. L., M. E. Ockert-Bell, and M. L. Michelsen (1992), The effect of cloud type on earth's energy balance: Global analysis, *J. Clim.*, *5*, 1281–1304, doi:10.1175/1520-0442(1992)005<1281:TEOCTO>2.0.CO;2.

Haywood, J. M., A. Jones, L. Clarisse, A. Bourassa, J. Barnes, P. Telford, N. Bellouin, O. Boucher, P. Agnew, C. Clerbaux, P. Coheur, D. Degenstein, and P. Braesicke (2010), Observations of the eruption of the Sarychev volcano and simulations using the HadGEM2 climate model, *J. Geophys. Res.*, *115*, D21212, doi:10.1029/2010JD014447, Copyright 2010 American Geophysical Union.

Hegglin, M. I., D. Brunner, H. Wernli, C. Schwierz, O. Martius, P. Hoor, H. Fischer, U. Parchatka, N. Spelten, C. Schiller, M. Krebsbach, U. Weers, J. Staehelin, and T. Peter (2004), Tracing troposphere-to-stratosphere transport above a mid-latitude deep convective system, *Atmos. Chem. Phys.*, *4*, 741–756.

Heirtzler, J. (2002), The future of the South Atlantic anomaly and implications for radiation damage in space, *J. Atmos. Terrest. Phys.*, *64*, 1701–1708, doi:10.1016/S1364-6826(02)00120-7.

Held, I. M. (1982), On the height of the tropopause and the static stability of the troposphere, *J. Atmos. Sci.*, *39*, 412–417, doi:10.1175/1520-0469(1982)039<0412:OTHOTT>2.0.CO;2.

Herman, G. F., M.-L. C. Wu, and W. T. Johnson (1980), The effect of clouds on the earth's solar and infrared radiation budgets, *J. Atmos. Sci.*, *37*, 1251–1261, doi:10.1175/1520-0469(1980)037<1251:TEOCOT>2.0.CO;2.

Hertz, H. (1889), Uber Strahlen elecktrischen Kraft, *Wiedem. Ann. Phys. Chem.*, *36*, 769–783.

Hess, P. G. (2005), A comparison of two paradigms: The relative global roles of moist convective versus nonconvective transport, *J. Geophys. Res.*, *110*, D20302, doi:10.1029/2004JD005456.

Heymsfield, A. J. (1993), Microphysical structure of stratiform and cirrus clouds, *Aerosol-Cloud-Climate Interactions*, edited by P. V. Hobbs, 97–121, Academic, San Deigo, Ca. (USA).

Highwood, E. J., and B. J. Hoskins (1998), The tropical tropopause, *Quart. J. Roy. Meteor. Soc.*, *124*, 1579–1604, doi:10.1002/qj.49712454911.

Hobbs, P. V. (1993), Aerosol-Cloud-Climate Interactions, Academic, San Diego, Ca. (USA).

Holton, J. R. (1979), *An Introduction to Dynamic Meteorology*, 2 ed., Academic Press, San Diego, Ca. (USA).

Holton, J. R., P. H. Haynes, M. E. McIntyre, A. R. Douglass, R. B. Rood, and L. Pfister (1995), Stratosphere-troposphere exchange, *Rev. Geophys.*, *33*, 403–439, doi:10.1029/95RG02097.

Hoskins, B. J. (1991), Towards a PV-θ view of the general circulation, *Tellus Ser. A.*, *43*, 27, doi:10.1034/j.1600-0889.1991.t01-3-00005.x.

Jost, H.-J., K. Drdla, A. Stohl, L. Pfister, M. Loewenstein, J. P. Lopez, P. K. Hudson, D. M. Murphy, D. J. Cziczo, M. Fromm, T. P. Bui, J. Dean-Day, C. Gerbig, M. J. Mahoney, E. C. Richard, N. Spichtinger, J. V. Pittman, E. M. Weinstock, J. C. Wilson, and I. Xueref (2004), In-situ observations of mid-latitude forest fire plumes deep in the stratosphere, *Geophys. Res. Lett.*, *31*, L11101, doi:10.1029/2003GL019253.

Junge, C. E., C. W. Chagnon, and J. E. Manson (1961), Stratospheric aerosols, *J. Atmos. Sci.*, *18*, 81–108.

Kirk-Davidoff, D. B., E. J. Hintsa, J. G. Anderson, and D. W. Keith (1999), The effect of climate change on ozone depletion through changes in stratospheric water vapour, *Nature*, *402*, 399–401, doi:10.1038/46521.

Kravitz, B., and A. Robock (2011), Climate effects of high-latitude volcanic eruptions: Role of the time of year, *J. Geophys. Res.*, *116*, D01105, doi:10.1029/2010JD014448.

Laaksonen, A., L. Pirjola, M. Kulmala, K.-H. Wohlfrom, F. Arnold, and F. Raes (2000), Upper tropospheric SO_2 conversion into sulfuric acid aerosols and cloud condensation nuclei, *J. Geophys. Res.*, *105*, 1459–1470, doi:10.1029/1999JD900933.

Le Treut, H., M. Forichon, O. Boucher, and Z.-X. Li (1998), Sulfate aerosol indirect effect and CO_2 greenhouse forcing: Equilibrium response of the LMD GCM and associated cloud feedbacks, *J. Clim.*, *11*, 1673–1684.

Liou, K.-N. (1986), Influence of cirrus clouds on weather and climate processes: A global perspective, *Mon. Weather Rev.*, *114*, 1167, doi:10.1175/1520-0493(1986)114<1167:IOCCOW>2.0.CO;2.

Liou, K. N. (1992), Radiation and cloud processes in the atmosphere, Oxford Univ. Press, New York, NY. (USA).

Liou, K. N. (2002), *An Introduction to Atmospheric Radiation*, 2 ed., Academic Press, New York, NY. (USA).

Liou, K. N., Y. Takano, P. Yang, and Y. Gu (2002), Radiative transfer in cirrus clouds: Light scattering and spectral information in cirrus, 265–296, Oxfort Univ. Press, New York, NY (USA).

Livesey, N. J., M. D. Fromm, J. W. Waters, G. L. Manney, M. L. Santee, and W. G. Read (2004), Enhancements in lower stratospheric CH_3CN observed by the Upper Atmosphere Research Satellite Microwave Limb Sounder following boreal forest fires, *J. Geophys. Res.*, *109*, D06308, doi:10.1029/2003JD004055.

Llewellyn, E. J., N. D. Lloyd, D. A. Degenstein, R. L. Gattinger, S. V. Petelina, A. E. Bourassa, J. T. Wiensz, E. V. Ivanov, I. C. McDade, B. H. Solheim, J. C. McConnell, C. S. Haley, C. von Savigny, C. E. Sioris, C. A. McLinden, E. Griffioen, J. Kaminski, W. F. Evans, E. Puckrin, K. Strong, V. Wehrle, R. H. Hum, D. J. W. Kendall, J. Matsushita, D. P. Murtagh, S. Brohede, J. Stegman, G. Witt, G. Barnes, W. F. Payne, L. Piché, K. Smith, G. Warshaw, D.-L. Deslauniers, P. Marchand, E. H. Richardson, R. A. King, I. Wevers, W. McCreath, E. Kyrölä, L. Oikarinen, G. W. Leppelmeier, H. Auvinen, G. Mégie, A. Hauchecorne, F. Lefèvre, J. de La Nöe, P. Ricaud, U. Frisk, F. Sjoberg, F. von Schéele, and L. Nordh (2004), The OSIRIS instrument on the Odin spacecraft, *Can. J. Phys.*, *82*, 411–422, doi:10.1139/P04-005.

Ludlam, F. H. (1948), The forms of ice-clouds, *Quart. J. Roy. Meteor. Soc.*, *74*, 39–56, doi: 10.1002/qj.49707431905.

Mace, G. G., M. Deng, B. Soden, and E. Zipser (2006), Association of tropical cirrus in the 10 15-km layer with deep convective sources: An observational study combining millimeter radar data and satellite-derived trajectories, *J. Atmos. Sci.*, *63*, 480–503, doi:10.1175/JAS3627.1.

Manabe, S., and R. F. Strickler (1964), Thermal equilibrium of the atmosphere with a convective adjustment, *J. Atmos. Sci.*, *21*, 361–385, doi:10.1175/1520-0469(1964)021<0361:TEOTAW>2.0.CO;2.

Margitan, J. J. (1984), Mechanism of the atmospheric oxidation of sulfur dioxide: Catalysis by hydroxyl radicals, *J. Phys. Chem.*, *88*, 3314–3318, doi:10.1021/j150659a035.

Mishchenko, M. I., L. D. Travis, and D. W. Mackowski (1996), T-matrix computations of light scattering by nonspherical particles: a review., *J. Quant. Spectrosc. Radiat. Trans.*, *55*, 535–575, doi:10.1016/0022-4073(96)00002-7.

Murtagh, D., U. Frisk, F. Merino, M. Ridal, A. Jonsson, J. Stegman, G. Witt, P. Eriksson, C. Jiménez, G. Megie, J. de La Noë, P. Ricaud, P. Baron, J. R. Pardo, A. Hauchcorne, E. J. Llewellyn, D. A. Degenstein, R. L. Gattinger, N. D. Lloyd, W. F. J. Evans, I. C. McDade, C. S. Haley, C. Sioris, C. von Savigny, B. H. Solheim, J. C. McConnell, K. Strong, E. H. Richardson, G. W. Leppelmeier, E. Kyrölä, H. Auvinen, and L. Oikarinen (2002), Review: An overview of the Odin atmospheric mission, *Can. J. Phys.*, *80*, 309–319, doi:10.1139/P01-157.

Newhall, C. G., and S. Self (1982), The volcanic explosivity index (VEI) - An estimate of explosive magnitude for historical volcanism, *J. Geophys. Res.*, *87*, 1231–1238, doi: 10.1029/JC087iC02p01231.

Ohring, G., and P. Clapp (1980), The effect of changes in cloud amount on the net radiation at the top of the atmosphere, *J. Atmos. Sci.*, *37*, 447–454, doi:10.1175/1520-0469(1980)037<0447:TEOCIC>2.0.CO;2.

Park, M., W. J. Randel, L. K. Emmons, P. F. Bernath, K. A. Walker, and C. D. Boone (2008), Chemical isolation in the Asian monsoon anticyclone observed in Atmospheric Chemistry Experiment (ACE-FTS) data, *Atmos. Chem. Phys.*, *8*, 757–764.

Petty, G. W. (2004), *A First Course in Atmospheric Radiation*, Sundog Publishing, USA.

Pfister, L., H. B. Selkirk, E. J. Jensen, M. R. Schoeberl, O. B. Toon, E. V. Browell, W. B. Grant, B. Gary, M. J. Mahoney, T. V. Bui, and E. Hintsa (2001), Aircraft observations of thin cirrus clouds near the tropical tropopause, *J. Geophys. Res.*, *106*, 9765–9786, doi: 10.1029/2000JD900648.

Pinto, J. P., O. B. Toon, and R. P. Turco (1989), Self-limiting physical and chemical effects in volcanic eruption clouds, *J. Geophys. Res.*, *94*, 11,165–11,174, doi:10.1029/JD094iD08p11165.

Poulida, O., R. R. Dickerson, and A. Heymsfield (1996), Stratosphere-troposphere exchange in a midlatitude mesoscale convective complex 1. Observations, *J. Geophys. Res.*, *101*, 6823–6836, doi:10.1029/95JD03523.

Ramaswamy, V., and V. Ramanathan (1989), Solar absorption by cirrus clouds and the maintenance of the tropical upper troposphere thermal structure, *J. Atmos. Sci.*, *46*, 2293–2310, doi:10.1175/1520-0469(1989)046<2293:SABCCA>2.0.CO;2.

Randel, W. J., and M. Park (2006), Deep convective influence on the Asian summer monsoon anticyclone and associated tracer variability observed with Atmospheric Infrared Sounder (AIRS), *J. Geophys. Res.*, *111*, D12314, doi:10.1029/2005JD006490.

Randel, W. J., M. Park, L. Emmons, D. Kinnison, P. Bernath, K. A. Walker, C. Boone, and H. Pumphrey (2010), Asian monsoon transport of pollution to the stratosphere, *Science*, *328*, 611–, doi:10.1126/science.1182274.

Read, W. G., M. J. Schwartz, A. Lambert, H. Su, N. J. Livesey, W. H. Daffer, and C. D. Boone (2008), The roles of convection, extratropical mixing, and in-situ freeze-drying in the Tropical Tropopause Layer, *Atmos. Chem. Phys.*, *8*, 6051–6067.

Rix, M., P. Valks, Nan Hao, J. Van Geffen, C. Clerbaux, L. Clarisse, P. F. Coheur, R. Loyola, T. Erbertseder, W. Zimmer, and S. Emmadi (2009), Satellite monitoring of volcanic sulfur doixide emissions for early warning of volcanic hazards, *IEEE*, *2*, 196–206, doi:10.1109/JSTARS.2009.2031120.

Roach, W. T. (1967), On the nature of the summit areas of severe storms in Oklahoma, *Quart. J. Roy. Meteor. Soc.*, *93*, 318–336, doi:10.1002/qj.49709339704.

Robock, A. (2000), Volcanic eruptions and climate, *Rev. Geophys.*, *38*, 191–220, doi:10.1029/1998RG000054.

Rossby, C. G. (1940), Planetary flow patterns in the atmosphere, *Quart. J. Roy. Meteor. Soc.*, *66*, 68–87.

Sassen, K., and B. S. Cho (1992), Subvisual-thin cirrus lidar dataset for satellite verification and climatological research, *J. App. Met.*, *31*, 1275–1285, doi:10.1175/1520-0450(1992)031<1275:STCLDF>2.0.CO;2.

Sassen, K., M. K. Griffin, and G. C. Dodd (1989), Optical scattering and microphysical properties of subvisual cirrus clouds, and climatic implications, *J. App. Met.*, *28*, 91–98, doi:10.1175/1520-0450(1989)028<0091:OSAMPO>2.0.CO;2.

Sassen, K., Z. Wang, and D. Liu (2008), Global distribution of cirrus clouds from CloudSat/Cloud-Aerosol Lidar and Infrared Pathfinder Satellite Observations (CALIPSO) measurements, *J. Geophys. Res.*, *113*, D00A12, doi:10.1029/2008JD009972, Copyright 2008 American Geophysical Union.

Sassen, K., Z. Wang, and D. Liu (2009), Cirrus clouds and deep convection in the tropics: Insights from CALIPSO and CloudSat, *J. Geophys. Res.*, *114*, D00H06, doi:10.1029/2009JD011916.

Schneider, T., P. A. O'Gorman, and X. J. Levine (2010), Water vapor and the dynamics of climate changes, *Rev. Geophys.*, *48*, RG3001, doi:10.1029/2009RG000302.

Seinfeld, G. L., and S. N. Pandis (2006), *Atmospheric Chemistry and Physics: From Air Pollution to Climate Change*, John Wiley, Hoboken, NJ. (USA).

Shapiro, M. A. (1980), Turbulent mixing within tropopause folds as a mechanism for the exchange of chemical constituents between the stratosphere and troposphere, *J. Atmos. Sci.*, *37*, 994–1004, doi:10.1175/1520-0469(1980)037<0994:TMWTFA>2.0.CO;2.

Solomon, S., K. H. Rosenlof, R. W. Portmann, J. S. Daniel, S. M. Davis, T. J. Sanford, and G.-K. Plattner (2010), Contributions of stratospheric water vapor to decadal changes in the rate of global warming, *Science*, *327*, 1219–, doi:10.1126/science.1182488.

Solomon, S., J. S. Daniel, R. R. Neely, J.-P. Vernier, E. G. Dutton, and L. W. Thomason (2011), The persistently variable "background" stratospheric aerosol layer and global climate change, *Science*, *333*, 866–, doi:10.1126/science.1206027.

SPARC (2006), Assessment of stratospheric aerosol properties, Rep. 4, World Clim. Res. Programme, Toronto, Ont. Canada.

Stenchikov, G. L., I. Kirchner, A. Robock, H.-F. Graf, J. C. Antuña, R. G. Grainger, A. Lambert, and L. Thomason (1998), Radiative forcing from the 1991 Mount Pinatubo volcanic eruption, *J. Geophys. Res.*, *103*, 13,837–13,858, doi:10.1029/98JD00693.

Stockwell, W. R., and J. G. Calvert (1983), The mechanism of the HO-SO_2 reaction, *Atmos. Env.*, *17*, 2231–2235, doi:10.1016/0004-6981(83)90220-2.

Turco, R. P., P. Hamill, O. B. Toon, R. C. Whitten, and C. S. Kiang (1979), A one-dimensional model describing aerosol formation and evolution in the stratosphere: I. Physical processes and mathematical analogs, *J. Atmos. Sci.*, *36*, 699–717.

Turco, R. P., R. C. Whitten, and O. B. Toon (1982), Stratospheric aerosols: Observation and theory (Paper 2R0109), *Rev. Geophys. Space Phys.*, *20*, 233, doi:10.1029/RG020i002p00233.

Van Geffen, J., M. Van Roozendael, W. Di Nicolantonio, L. Tampellini, P. Valks, T. Erbertseder, and R. Van der A (2007), Monitoring of volcanic activity from satellite as part of GSE PROMOTE, *presented at the ENVISAT Symp.*, ESA, SP-636, Montreux, France.

Vernier, J.-P., L. W. Thomason, and J. Kar (2011), CALIPSO detection of an Asian Tropopause Aerosol Layer, *Geophys. Res. Lett.*, *380*, L07,804, doi:10.1029/2010GL046614, Copyright 2011 American Geophysical Union.

Vernier, J. P., J. P. Pommereau, A. Garnier, J. Pelon, N. Larsen, J. Nielsen, T. Christensen, F. Cairo, L. W. Thomason, T. Leblanc, and I. S. McDermid (2009), Tropical stratospheric aerosol layer from CALIPSO lidar observations, *J. Geophys. Res.*, *114*, D00H10, doi:10.1029/2009JD011946.

Waliser, D. E., and C. Gautier (1993), A satellite-derived climatology of the itcz., *J. Clim.*, *6*, 2162–2174, doi:10.1175/1520-0442(1993)006<2162:ASDCOT>2.0.CO;2.

Wallace, J. M., and P. V. Hobbs (2006), *Atmosphere Science - An Introductory Survey.*, Academic Press, Elsevier, San Diego, Ca. (USA).

Wang, P.-H., P. Minnis, M. P. McCormick, G. S. Kent, and K. M. Skeens (1996), A 6-year climatology of cloud occurrence frequency from Stratospheric Aerosol and Gas Experiment II observations (1985-1990), *J. Geophys. Res.*, *1012*, 29,407–29,430, doi:10.1029/96JD01780, Copyright 1996 American Geophysical Union.

Wang, P. K. (2003), Moisture plumes above thunderstorm anvils and their contributions to cross-tropopause transport of water vapor in midlatitudes, *J. Geophys. Res.*, *108*, 4194, doi: 10.1029/2002JD002581.

Waterman, P. C. (1971), Symmetry, unitarity, and geometry in electromagnetic scattering, *Phys. Rev. D.*, *3*, 825–839, doi:10.1103/PhysRevD.3.825.

Waters, J. W., L. Froidevaux, R. S. Harwood, R. F. Jarnot, H. M. Pickett, W. G. Read, P. H. Siegel, R. E. Cofield, M. J. Filipiak, D. A. Flower, J. R. Holden, G. K. Lau, N. J. Livesey, G. L. Manney, H. C. Pumphrey, M. L. Santee, D. L. Wu, D. T. Cuddy, R. R. Lay, M. S. Loo, V. S. Perun, M. J. Schwartz, P. C. Stek, R. P. Thurstans, M. A. Boyles, K. M. Chandra, M. C. Chavez,

G.-S. Chen, B. V. Chudasama, R. Dodge, R. A. Fuller, M. A. Girard, J. H. Jiang, Y. Jiang, B. W. Knosp, R. C. Labelle, J. C. Lam, A. K. Lee, D. Miller, J. E. Oswald, N. C. Patel, D. M. Pukala, O. Quintero, D. M. Scaff, W. Vansnyder, M. C. Tope, P. A. Wagner, and M. J. Walch (2006), The Earth Observing System Microwave Limb Sounder (EOS MLS) on the Aura satellite, *IEEE Trans. Geosci. Rem. Sens.*, *44*, 1075–1092, doi:10.1109/TGRS.2006.873771.

Winker, D. M., and J. Pelon (2003), The CALIPSO Mission, 1329–1331, IEEE International, geoscience and remote sensing symposium, 2003 IGARSS '03.

Winker, D. M., W. H. Hunt, and C. A. Hostetler (2004), Status and performance of the CALIOP lidar, *Society of Photo-Optical Instrumentation Engineers (SPIE) Conference Series*, vol. 5575, edited by U. N. Singh, 8–15, doi:10.1117/12.571955.

Winker, D. M., W. H. Hunt, and M. J. McGill (2007), Initial performance assessment of CALIOP, *Geophys. Res. Lett.*, *34*, L19803, doi:10.1029/2007GL030135.

World Meteorological Organization (1957), Definition of the tropopause, *World Meteorol. Org. Bull.*, *6*, 136.

Wylie, D., D. L. Jackson, W. P. Menzel, and J. J. Bates (2005), Trends in global cloud cover in two Decades of HIRS observations, *J. Clim.*, *18*, 3021–3031, doi:10.1175/JCLI3461.1.

Yang, Q., Q. Fu, and Y. Hu (2010), Radiative impacts of clouds in the tropical tropopause layer, *J. Geophys. Res.*, *115*, D00H12, doi:10.1029/2009JD012393.

Zhao, J., R. P. Turco, and O. B. Toon (1995), A model simulation of Pinatubo volcanic aerosols in the stratosphere, *J. Geophys. Res.*, *100*, 7315–7328, doi:10.1029/94JD03325.